ON CONTROLLABLE STIFFNESS BIPEDAL WALKING

by Reza Ghorbani

A thesis submitted to the Faculty of Graduate Studies

in partial fulfillment of the requirements for the degree of

Doctor of Philosophy

Department of Mechanical and Manufacturing Engineering

The University of Manitoba

Winnipeg, MB, Canada

Abstract

Impact at each leg transition is one of the main causes of energy dissipation in most of the current bipedal walking robots. Minimizing impact can reduce the energy loss. Instead of controlling the joint angle profiles to reduce the impact which requires significant amount of energy, installing elastic mechanisms on the robots structure is proposed in this research, enabling the robot to reduce the impact, and to store part of the energy in the elastic form which returns the energy to the robot. Practically, this motivates the development of the bipedal walking robots with adjustable stiffness elasticity which itself creates new challenging problems. This thesis addresses some of the challenges through five consecutive stages. Firstly, an adjustable compliant series elastic actuator (named ACSEA in this thesis) is developed. The velocity control mode of the electric motor is used to accurately control the output force of the ACSEA. Secondly, three different conceptual designs of the adjustable stiffness artificial tendons (ASAT) are proposed each of which is added at the ankle joint of a bipedal walking robot model. Simulation results of the collision phase (part of the gait between the heel-strike and the foot-touch-down in bipedal walking) demonstrate significant improvements in the energetics of the bipedal walking robot by proper stiffness adjustment of ASAT. In the third stage, in order to study the effects of ASATs on reducing the energy loss during the stance phase, a simplified model of bipedal walking is introduced consisting of a foot, a leg and an ASAT which is installed parallel to the ankle joint. A linear spring, with adjustable stiffness, is included in the model to simulate

the generated force by the trailing leg during the double support phase. The concept of impulsive constraints is used to establish the mathematical model of impacts in the collision phase which includes the heel-strike and the foot-touch-down. For the fourth stage, an energy-feedback-based controller is designed to automatically adjust the stiffness of the ASAT which reduces the energy loss during the foot-touch-down. In the final stage, a speed tracking (ST) controller is developed to regulate the velocity of the biped at the midstance. The ST controller is an event-based time-independent controller, based on geometric progression with exponential decay in the kinetic energy error, which adjusts the stiffness of the trailing-leg spring to control the injected energy to the biped in tracking a desired speed at the midstance. Another controller is also integrated with the ST controller to tune the stiffness of the ASAT when reduction in the speed is desired. Then, the local stability of the system (biped and the combination of the above three controllers) is analyzed by calculating the eigenvalues of the linear approximation of the return map. Simulation results show that the combination of the three controllers is successful in tracking a desired speed of the bipedal walking even in the presence of the uncertainties in the leg's initial angles.

The outcomes of this research show the significant effects of adjustable stiffness artificial tendons on reducing the energy loss during bipedal walking. It also demonstrates the advantages of adding elastic elements in the bipedal walking model which benefits the efficiency and simplicity in regulating the speed. This research paves the way toward developing the dynamic walking robots with adjustable stiffness ability which minimize the shortcomings of the two major types of bipedal walking robots, i.e., passive dynamic walking robots (which are energy efficient but need extensive parameters tuning for gait stability) and actively controlled walking robots (which are significantly energy inefficient).

Acknowledgments

I would like to thank Professor Christine Wu for her continuous guidance, suggestions, patience, advice, and encouragement that helped me throughout my Ph.D. program. Professor Wu always supported me with her valuable suggestions during our discussions which led me to better understand the basics of my research. I also wish to thank Professor Sepehri for giving me the unique opportunity of working on experimental projects in his laboratory through his robotics course. One of the unique opportunities during my research at the University of Manitoba was working with Professor Eric Bibeau in developing new technologies in sustainable transportation. My Ph.D. program was mostly supported by the University of Manitoba Graduate Fellowship. I greatly appreciate all of the considerations of my advisory committee members during my doctoral work, Professor Annakkage, Professor Balakrishnan, Professor Lehn, and Professor Wang for their careful review, comments, and suggestions. I had the chance to visit some of the advanced robotics laboratories and present my research which was mainly supported by the laboratory directors. I would like to take this opportunity to express my gratitude to Professor Mark Spong in The Center for Autonomous Engineering and Robotics at the University of Illinois at Urbana–Champaign, Professor Chris Atkeson in The Robotics Institute at Cornegie Mellon University, Professor Russ Tedrake in The Robot Locomotion Group at MIT, Professor Hugh Herr in The Biomechatronics Group at the MIT Media Laboratory, Professor Zuomin Dong the Chair of the Department of Mechanical Engineering at the University of Victoria, and Professor Elizabeth

Croft in the Collaborative Advanced Robotics and Intelligent Systems Laboratory at the University of British Columbia. I appreciate all of the considerations of Professor Takanishi and Massimiliano Zecca in the Takanishi Laboratory at Waseda University to support my application for the JSPS postdoctoral fellowship.

I thank my fellow graduate students for valuable discussions and friendly supports at the University of Manitoba. Special appreciation goes to Farshid Najafi, Mark Karpenko, Nima Tehrani, Behraad Bahreyni, Caixia Yang and Xiuping Mu. I learned a lot through my daily technical and somehow philosophical discussions in design of robotic systems with Farshid.

I appreciate all the support and encouragement of my special friends, advisers and colleagues in the Sharif University of Technology during several years of collaborations. Special thanks for Professor Sohrabpour the Chancellor of the Sharif University of Technology for his continuous advice and encouragement, Professor Mansour Jamzad for his six years of full support, Professor Iraj Shadravaan for his kindness and full technical support, Professor Yahya Tabesh, Professor Reza Soltani, Professor Pourtakdoust, Professor Amir Khayyat, Amir Ali Forough Nassirae a wonderful friend and my first teacher in robotics, Hamid Reza Chitsaz, Alireza Haj Khodabakhshi, Moslem Kazemi, Seyyed Bashir Sadjad, Ehsan Chiniforoushan, Farid Mobasser, Seyyed Vahaab Mirrokni and Mohammad Taghi Hajiaghayi. I appreciate the unforgettable kindness and supports of Alireza and Bashir, and also Arthur and Ruth Huebert during my doctoral program.

I thank my family for their constant support and encouragement. My parents have always supported me and have made it possible for me to start this journey. Finally, I give my deepest appreciation and best wishes to my eternal companion Sara. I am thankful for her faith, consistency, gentleness, kindness, love, and her great sense of humor.

Table of Contents

List of Symbols

SEA	Series Elastic Actuator
$AASC$	Automated Adjustable Stiffness Coupling
$ASAT$	Adjustable Stiffness Artificial Tendon
$RASAT$	Rotary Adjustable Stiffness Artificial Tendon
$LASAT$	Linear Adjustable Stiffness Artificial Tendon
$OLASAT$	Offset Location Adjustable Stiffness Artificial Tendon
SMR	Simplified Model of Robot
FTD	Foot-Touch-Down
HS	Heel-Strike
MD	Midstance
EN	End of the walking step
COM	Center of mass of the body
d	Distance between the spring and the center of rotation
θ	Angular displacement of the input and output links
x	The spring deflection in AASC and RASAT
K_{spring}	The stiffness of each spring in AASC
T	Internal torque between the input and output links
K_s	The stiffness of the coupling in AASC
K_i	The electromechanical conversion coefficient
K_{emf}	The back electromotive force constant

T_m	DC motor output torque
R_a	DC motor winding resistance
I	DC motor applied current
ω	DC motor shaft angular velocity
J	The moment of inertia of the rotor of the DC motor
b	The viscous friction in the bearings
E	The input voltage of the DC motor
R_a	DC motor winding resistance
T_{load}	The load's reflected torque on the motor
n_g	Gear ratio
μ_g	Gearbox efficiency
Z_m	Motor impedance
Z_l	Load impedance
K_a	amplifier gain
K_i	DC motor torque constant
ρ_s	Spring stiffness ratio
K_p	Proportional gain
K_I	Integral gain
J_l	Load inertia
J_i	Initial value of load inertia
u_o	Saturation operator output
u_i	Saturation operator input
T_{dmin}	Minimum value of the desired torque
T_{dmax}	Maximum value of the desired torque
I_{max}	Maximum current of the DC motor
K_{sat}	Saturation operator equivalent gain

e_T	Torque error
u_{hint}	Maximum output value of the integral saturation operator
$u_{lmax_{int}}$	Maximum input value of the integral saturation operator
u_{hvel}	Maximum output value of the velocity saturation operator
ω_{max}	Maximum angular velocity of the DC motor
amp_{output}	Amplitude of the output torque signal
amp_{input}	Amplitude of the input torque signal
K_1	Stiffness of low stiffness spring in RASAT
K_2	Stiffness of high stiffness spring in RASAT
l	The offset between the low and high stiffness springs in RASAT
d_{max}	The maximum value of distance d in RASAT
μ	Stiffness ratio of the spring 1 and spring 2 in RASAT
K_{s1}	Stiffness of spring 1 in LASAT
K_{s2}	Stiffness of spring 2 in LASAT
N_s	Maximum number of coils of the springs in LASAT
P_1	Coil's stiffness of the spring 1 in LASAT
P_2	Coil's stiffness of the spring 2 in LASAT
D_i	Mean coil diameter of spring in LASAT
dia_i	Wire diameter of spring in LASAT
G_i	Shear modulus of the material of springs in LASAT
N_1	Number of active coils of spring 1 in LASAT
N_2	Number of active coils of spring 2 in LASAT
ρ	The coil's stiffness ratio of the spring 1 and the spring 2 in LASAT
λ	Number o active coils index in LASAT
K_{a1}	Actual stiffness of spring 1 in LASAT
K_{a2}	Actual stiffness of spring 2 in LASAT

K_{eq}	The equivalent stiffness of the series springs in LASAT
Ls	Shut length of the soft spring in LASAT
a	The offset between two springs in OLASAT
K_{sp1}	Stiffness of spring 1 in OLASAT
K_{sp2}	Stiffness of spring 2 in OLASAT
d_{OLASAT}	Spring's deflection in OLASAT
F_{OLASAT}	The acting force on OLASAT
η	Stiffness ratio of the spring 1 and spring 2 in OLASAT
θ_i	The angle of the link i with respect to the horizontal axis
x_h	The horizontal distance of the heel
y_h	The vertical distance of the heel
D_{ij}	Elements of the inertia matrix
$\hat{\lambda}_k$	Impulsive Lagrangian multiplier
M	Inertia matrix
$H(\theta, \dot{\theta})$	Torque matrix related to centrifugal and coriolis terms
$G(\theta)$	Torque matrix related to gravity of each link
$S(\theta)$	Torque related to the elastic strain
$I(\theta)$	Generalized external torque matrix
T_{ankle}	Torque at ankle joint
K_{knee}	Angular stiffness of the knee joint
$\mathbf{q}$	Generalized coordinate vector
$\hat{Q}_i$	External impulse
$\hat{\lambda}_k$	Impulsive Lagrangian multiplier
${}^{HS}\hat{\lambda}$	Impulsive Lagrangian multiplier at the heel-strike
${}^{FTD}\hat{\lambda}$	Impulsive Lagrangian multiplier at the foot-touch-down
L_0	Relaxed length of the trailing leg spring

L_t	Distance between COM of the body and the toe
l_f	Distance between the toe and the ankle joint
l_{step}	Step length of the biped
d_1	Distance between the center of mass of the foot to the heel
d_2	Distance between the center of mass of the body to the ankle joint
φ_0	Initial angle of the trailing leg
β	Mass ratio which is equal to $\frac{m_1}{m_2}$
ψ	Length ratio which is equal to $\frac{l_1}{l_2}$
ζ	Length ratio which is equal to $\frac{d_1}{l_2}$
υ	Length ratio which is equal to $\frac{l_f}{l_2}$
ς	which is equal to $\frac{K_{sp1}R^2}{m_2 l_2 g}$
η	Stiffness ratio which is equal to $\frac{K_{sp2}}{K_{sp1}}$
K_t	Stiffness and of the trailing leg spring
ν	Trailing leg stiffness ratio which is equal to $\frac{K_t l_2}{m_2 g}$
κ	Dimensionless kinetic energy
τ_{ankle}	Ankle joint torque ratio
${}^{FTD}E^-$	Kinetic energy of the biped before the foot-touch-down
${}^{FTD}E^+$	Kinetic energy of the biped after the foot-touch-down
${}^{MD}E_d$	Desired kinetic energy at midstance
ΔE_r	Required kinetic energy change in each walking step
E^{inj}	Total injected energy in a single walking step
E^{dis}	Total dissipated energy in a single walking step
${}^{FTD}X$	X at the foot-touch-down
${}^{HS}X$	X at the heel-strike
${}^{MD}X$	X at the midstance
X^-	X immediately before event (here impact)

X^+	X immediately after event (here impact)
n	Walking step number
ΔL_{dss}	Initial deformation of the trailing leg spring

List of Figures

List of Tables

Chapter 1

Introduction

The research on the principles of legged locomotion is an interdisciplinary endeavor. Such principles are coming together from research in biomechanics, neuroscience, control theory, mechanical design, and artificial intelligence. Such research can help us to understand human and animal locomotion in implementing useful legged vehicles. There are three main reasons for exploring the legged locomotion. The first reason is to develop vehicles that can move on uneven and rough terrain. Vehicles with wheels can only move on prepared surfaces such as roads and rails; however, most surfaces are not paved. The second reason is to understand human and animal locomotion mechanics. The study of the mechanisms and principles of control found in nature can help us to develop better legged vehicles. The third reason which motivated the study of legged locomotion is the need to build artificial legs for amputees. Although some effective artificial legs have been built to date, more in-depth research is required to fully understand the mechanisms and movements necessary to substitute the actual limbs.

The research in this thesis concerns a group of legged robots known as bipedal walking robots. Research on this subject has a long history; however, it is only in the last two decade that successful experimental prototypes have been developed. The vast

majority of humanoid and bipedal robots control the joint angle profiles to carry out the locomotion. Active walking robots (robots with actuators) can do the above task with reasonable speed and position accuracy at the cost of high control efforts, low efficiencies, and most of the time unnatural gaits. Asimo and WABIAN II, shown in Figure 1.1, are among the most successful bipedal walking humanoid robots. In spite of the extensive research on humanoid robots, the actions of walking, running, jumping and manipulation are still difficult for robots.

Passive-dynamic walking robots have been developed by researchers to mimic human

(a) (b)

Figure 1.1: Example of humanoid bipedal walking robots: (a) WABIAN II: Takanishi Lab, Waseda University (www.takanishi.mech.waseda.ac.jp), (b) Asimo: Honda (http://world.honda.com/ASIMO).

walking. The main goal of building passive-dynamic walking robots is to study the role of natural dynamics in bipedal walking. Passive-dynamic walkers use gravitational energy to walk down a ramp without any actuators. They are energy efficient but have weak stability in the gait. In addition, the major cause of the energy loss in the current passive-dynamic walking robots is the instantaneous change in the velocity of the mass centre during each leg transition. Some examples of passive-dynamic walking robots are shown in Figure 1.2.

Recently, to overcome the limitations and disadvantages of the above walking robots

Figure 1.2: Examples of passive walking robots from other research laboratories. From left to right: 1- Cornell University (http://ruina.tam.cornell.edu/index.html), 2- Museon Walker, Delft Biorobotics Laboratory (mms.tudelft.nl), 3- Cornell University.

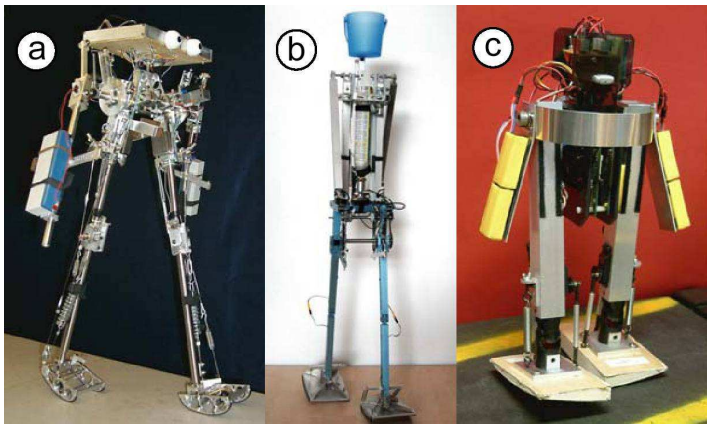

Figure 1.3: Three powered walking robots: (a) The Cornell biped (http://ruina.tam.cornell.edu/index.html), (b) The Delft biped (mms.tudelft.nl), (c) The MIT learning biped (http://groups.csail.mit.edu/locomotion/russt.html).

(active and passive), researchers have proposed energy-efficient walking robots which can be divided in two major research areas. The first research area is the walking robots with actuators which track the optimized joints angle trajectories. The trajectories are determined from an optimization procedure used to minimize an objective function. The second research area is the passive–dynamic robots with direct drive or elastic actuators installed at some of the joints of the biped. Three successful dynamic walking robots are the Cornell Robot (Figure 1.3a), Denise (Figure 1.3b) and Toddler (Figure 1.3c). The main goal of developing the dynamic walking robots is to increase the efficiency of locomotion.

In this thesis, a new research area in energy-efficient walking robots is introduced and developed which deals with adjustable-stiffness dynamic walking. The main characteristics of the adjustable–stiffness dynamic walking robots is that they have adjustable stiffness elastic elements at their joints, which is mainly inspired by the muscle-tendon mechanisms of humans and animals. In the following sections of this chapter, the motivation of the research will be explained and the advantages and limitations of current systems (actuation and walking robots) will be discussed. Then, new methods to improve the current systems will be proposed. The background on the work of other researchers is also given in this chapter. At the end of this chapter, a layout of the thesis will be presented.

1.1 Motivation

The motivations of each part of this research are discussed separately in the following sections.

1.1.1 Actuation systems and force control

Converting some of the energy of a system into mechanical force and motion, is a process of actuation. The device or mechanism that provides this energy conversion is an actuator, e.g., an electromagnetic motor with a gear transmission.

Standard actuation systems in humanoid robots are designed to be as stiff as possible for a given load. This allows the actuator to transmit power with no internal storage of energy. Unfortunately, a stiff transmission in an actuator not only causes a high open-loop gain of the actuator but also increases the impulsive forces. In addition, impulsive forces dissipate the energy of the robot by large plastic impact. Impulsive forces can also cause major damages to the sensors and hardware system installed inside the robots. The high open-loop gain and stiff transmission in the robot's actuators imply that to maintain the stability of the actuator's force controller, control gains must be

kept low. This indicates overall poor closed loop performance without the capability of handling shock loads from the environment.

Bipedal walking robots have direct interactions with unstructured environments, as well with humans. Thus, in bipedal robotic applications, an actuator is more desirable as a force/torque source than as a position/velocity source. Most of the current robotic actuation systems are specially designed for joint position control and are poor at accurately controlling the desired force. A portion of these inaccuracies in actuators are due to the friction, stick-slip, breakaway forces on seals, and backlash in speed reducers. A conventional method to control the force/torque of the electric actuators is to use the current control mode of the electric motor. However for tasks requiring accurate force control with a low desired force amplitude, the force disturbances in the actuators can be problematic in the current control mode.

To overcome the above limitations of current actuation methods for bipedal robots, an adjustable stiffness series elastic actuator is introduced in this work. Two major contributions are made. The first is introducing the conceptual design of an automated adjustable stiffness coupling that is placed between the transmission of the actuator and the load. The mechanical impedance of the coupling can be adjusted over a wide range. The elasticity in the actuator of a bipedal walking robot can reduce the impulsive forces caused by leg collision during walking and can assist in the storage of energy. It is also strongly believed that if the electric motor runs in a velocity control mode instead of current control mode, the overall actuator performance can be improved [1]. The second contribution of this work is the development of a new control method by running the electric motor in the velocity control mode. The inertia of the robot and the actuator filter the force noise while the velocity or position of the actuator is controlled. The process of filtering assists the actuator to operate with better force control performance. Use of velocity control mode was recommended by Williamson [1]. By using this method, the small force sensitivity and the error rejection would

be improved. In this thesis, only the modeling and the control methodology of the actuator are presented. Physical implementation of the actuator remains as follow-up research.

1.1.2 Efficiency in bipedal walking robots

As the principles of physics, motion of an object with a constant speed requires zero energy cost, while the summation of the external forces on the object are orthogonal to the direction of the motion [2]. For instance, frictionless sliding of an object on a level surface, or oscillatory motion of a mass-spring system with no damping require zero energy. By assuming frictionless joints and neglecting air-friction losses, the question is if bipedal walking on a level surface can be similarly energy-cost free.

To answer the question, let us consider a frictionless walking device with rigid links which is subject to gravity and supported by a frictional level surface. The device can include actuators and conservative springs at the hinges (joints). With no frictional sliding, collision in the device is a major source of energy loss that dissipates energy by some combination of mechanisms, i.g., heat at the collision point, dissipation in robot structure, acoustic radiation, etc. [2]. Kinematics of the device before and after collision can determine the energy loss using linear and angular momentum balance, regardless of the mechanism of dissipation [2]. The sudden change in the velocity of the objects before and after collision necessarily causes energy loss. No energy is lost if the new contacts are made in a collision free manner, with zero relative velocity between the approaching objects.

Thus, the search for an efficient bipedal walking with nearly zero-energy-cost is a search for a machine that has motions with low negative actuator work, with no frictional slip at the ground contacts, and with collision free contacts [2]. Because the attention is limited to models with no ground slip and to models with no actuation, the search

becomes limited to finding a collision free walking mechanism. Some possible ways to pursue collision free movement, and thus the ideal zero-energy-cost walking are explained by Gomes and Ruina [2] using kinematic mechanisms and compliant contact. Seyfarth and Geyer have studied the compliant walking model [3–6] and the results of their work strongly support the use of compliancy in bipedal walking robots.

Collision of the leg with the ground is inevitable in the bipedal walking cycle. Collision is also one of the major sources of energy loss. Development of a mechanism or methodology to reduce the energy loss caused by the collision is a challenging problem in bipedal walking robots. This challenge is the major focus of this Ph.D. program research.

1.2 Background and related work

In this section, the background and the previous work related to my research are reviewed.

1.2.1 Adjustable stiffness compliant actuator

Many researchers have studied compliant actuators or the effects of flexible links on robot control [7], [8], [9], [10], [11], [12]. Some research has been done on direct drive actuation [13] to increase the performance of force controllers. Advantages of using compliance, which is a term used for elasticity in this work, for sensing the force on teleoperated systems were studied by Kulishov [14]. The deflection between the actuator output shaft and the motor position was measured to enhance the stability of a force controller [15]. By direct measurement of the spring deflection which is in series with the actuators transmission, Pratt and Williamson [1, 16] introduced the Series Elastic Actuators (SEA) which was further developed by Robinson [17]. The most advanced humanoid robot, Asimo, constructed by Honda Research Laboratories [18, 19] uses harmonic drive motors for actuation and employs visco-elastic materials at the joints for

shock tolerance. Stanford's researchers proposed a new type of compliant actuators by adding an extra small direct drive DC motor at a robot joint parallel to the output shaft of the SEA [20]. Special mechanisms were developed at Carnegie Mellon University to change the compliancy of the actuators for a running gait [21], [22]. Developing a variable stiffness transmission, especially for the actuation of the human-interaction-based robotic systems, was highly recommended by Bicchi [23]. Also, some mechanisms were explained by Mason and Salisbury [24] for articulated hand applications. The following actuation methods were recently developed and proven successful as unique actuation approaches: the joint torque control approach [12], series elastic actuation [17], and Distributed Macro-Mini actuation approach (DM^2) [20]. In the following sections, the above actuation approaches are explained in detail with their advantages and limitations in bipedal walking robots.

Joint torque controlled robots

Joint torque controlled robots consist of high performance actuators and transmissions with integrated torque sensors to achieve the desired performance levels. The bandwidth of the joint actuation is limited and is a result of the nonlinearities and friction inherent in actuator–transmission systems [12], [25]. The implementation of the joint torque control allows for near zero low-frequency impedance, but it is ineffective at higher frequencies. Therefore, the magnitude of impact load, which is determined by the high frequency impedance of the contacting surfaces, is not attenuated, making the actuators difficult to be used in efficient bipedal walking robots. While the joint torque control has been successful in improving the force and impedance control of robotic manipulators, their fundamental open-loop characteristics limit their applications in efficient bipedal walking robots.

Series elastic actuation

Series Elastic Actuators (SEA) [17] have elastic elements intentionally placed in series between the actuator and the load. Deflection of the elastic element is measured to provide an accurate estimate of the force. A linear feedback controller is implemented to regulate the output force by controlling the current of the DC motor, as shown in Figure 1.4. The impedance of the actuator in high frequency is limited by the stiffness of the elastic coupling. The low stiffness value of the series elastic element decreases the open-loop gain which allows the use of a simple and high-gain PD controller. The force control system is stable and possesses low impedance over a wide frequency range, but the open loop characteristic of the SEA causes a physical limitation in the bandwidth of the actuator. The velocity and torque saturation of the DC motor in turn adds to this problem [1, 16, 17].

Low stiffness of the joints is highly valued in bipedal walking robots since it provides nearly passive motion i.e. in the knee joint during the swing phase. By choosing low stiffness elastic elements in series elastic actuators, the impedance of the system remains low with a negative effect of reducing the bandwidth of the system. As a solution, stiffness tuning of the elastic element in SEA (from a low to a high value) can improve the capabilities of the SEA in various tasks in bipedal walking robots. In addition, the Coulomb friction and stiction are dramatically affected by putting elastic elements (with fixed or adjustable stiffness) into the actuator which can not be fully compensated by using the current control of the DC motor [16]. Developing a new control method is also necessary to improve the performance of the series elastic actuators.

Distributed Macro-Mini actuation approach

The Distributed Macro-Mini actuation approach (DM^2) was developed to overcome the safety limitations of joint torque control as well as performance limitations of the

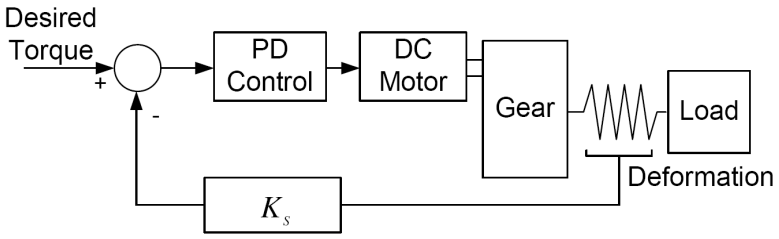

Figure 1.4: Schematic diagram of a series elastic actuator.

SEA [20]. The DM^2 has a pair of parallel actuators installed in different locations on the manipulator. The schematic diagram of DM^2 is shown in Figure 1.5. The SEA is located at the base of the manipulator that significantly reduces the weight and inertia of the manipulator. For the low frequency actuation, low impedance is achieved by using an SEA. For the high frequency actuation, very low impedance is achieved by using a small torque motor with low inertia connected to the manipulator joints through a low friction and low reduction cable transmission. As shown in Figure 1.5, the deformation of the elastic element provides the force/torque feedback. The torque error is compensated through a proportional derivative controller which is then commanded to the base actuator. The torque error is also commanded to the joint actuator (Figure 1.5). This actuation approach has some limitations in applications involving a number of different control modes i.e., free-space motion with contact transitions, in applications requiring a low-impedance torque source, and in applications involving a number of different tasks with a wide range of impedance requirements.

By considering the developmental limitations of each method of compliant actuation for the bipedal walking robots, a new actuation approach is necessary for compensating the limitations of each method. In the thesis a new actuation approach named here as Adjustable Compliant Series Elastic Actuator (ACSEA) is developed. ACSEA includes the electromechanical design to change the stiffness of the elastic element over a wide range. This capability enables the actuator to preform as both a passive element

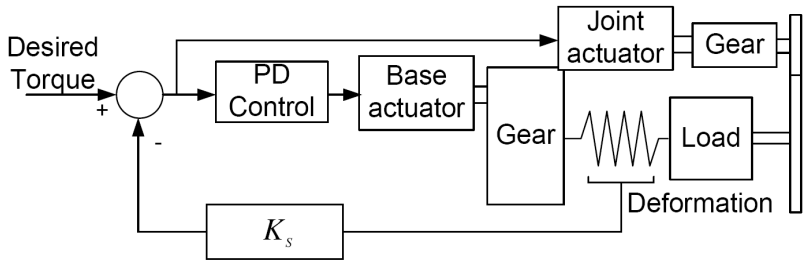

Figure 1.5: Schematic diagram of a distributed macro-mini actuator.

and an active force-control actuator. From the actuator force control point of view, changes in the stiffness of the actuator cause changes in the mechanical gain of the closed loop system. In addition, there are other shortcomings in the system such as stiction and amplifier saturation. To overcome some of these difficulties in controlling the torque (or the force) of the actuator, the velocity control mode of the DC motor is used in this work instead of the common method of controlling the current of the DC motor [16].

1.2.2 Adjustable stiffness artificial tendon

Walking robots based on joint-angle-control paradigm are often energy inefficient. On the other hand, passive-dynamic walkers can provide human-like locomotion and are simple in structure, more efficient in energy consumption, and easier to control than joint-angle-control robots [26]. The modeling, control and analysis of passive-dynamic devices are well documented [27–37] and essentially follow McGeer's work [38]. Although the passive dynamic robots are among the most efficient walking robots, the instantaneous change in the velocity direction of the center of mass of the robot during collision is the most common reason for losing energy. In human gait, the heel pad and the Achilles tendon absorb part of the energy during and after the impact of the collision phase. That energy returns to the leg during the following stance phase [39]. However, for walking robots such energy is dissipated.

The elastic model of a leg [40, 41], i.e. spring-mass, has been well accepted for the dynamics of fast-legged locomotion under gravity [42–44]. It has also been found that the elastic elements at the joints of legs support the self-stabilizing capabilities in running [38,45]. Recently, researchers have demonstrated that the global leg stiffness may come from local elasticity established by appropriate joint torques [42,46]. In addition, they showed that proper adjustment of joint elasticities to the leg geometry and to the initial conditions of ground contact provides internal stability. Experiments and measurments by Ferris et al. [47] show that human runners adjust their leg stiffness to accommodate changes in surface stiffness, allowing them to maintain similar running mechanics on different surfaces. The simplified model of bipedal walking which is often used for studying of energetics is a point mass connected at the top of an inverted pendulum. Seyfarth and Geyer [3–6] have studied the compliant legged locomotion by replacing the conventional model with massless linear spring legs connected to a point mass. Compliant walking model is more similar to the human walking pattern than the conventional model.

The recent research on bipedal walking locomotion by Ruina and Kuo [39], Seyfarth [3], Geyer [4–6] and Wisse [30,31] motivates the development of an adjustable stiffness elastic element for bipedal walking robots. With respect to the above-referenced research and inspired by the functionality of human Achilles tendon, it is believed that the artificial tendon at the ankle of the walking robot can increase the performance of locomotion by providing two distinct purposes: one for energy storage with compliant collision and the other for transmitting the motion into forces for fine and stable manipulation [48]. Adjusting the stiffness of the artificial tendons in the structure of the bipedal walking robots can improve its energy economy.

1.2.3 A note on energy optimality in legged robots

Robots are designed for different applications and their best way of locomotion depends on their tasks. High accelerations and maneuverability may be required to successfully catch an object (e.g., [49]) or to successfully run on uneven trains (e.g., [50]). The same robot may be used at other times to maintain a slow but sufficient speed for long periods of time (endurance) e.g., carrying a load [51]. In all these situations, keeping stability and at the same time economizing the energy consumption is hard to achieve [52], [53].

This thesis is mostly concerned with energy economy of steady bipedal walking. In particular, the structural adaptation is considered by adjusting the stiffness of artificial tendons. For example, mechanically designed artificial tendons in a biped store and return part of the energy of the biped during walking, thus minimizing the work requirements of these gaits.

It is necessary to clearly discuss what is meant by energy optimality in robotics. When a robot is not moving - not actuating - but still processing, it requires power to support the various calculation processes e.g., visual processing, sensing, and decision making. In this process, the power requirement can vary. However, the power consumption can be assumed constant at specific situations or applications. When the robot starts moving, actuators are employed to perform work on the body and exert forces as appropriate. Actuating the links requires energy to generate motion. Further, actuation requires power conversion and more processing. Actuation also increases heat caused by deficiencies in the power amplifier, batteries and transmissions. All these increase entire energy consumption. The increase in power demand due to the use of actuators for movement is the sum total of all such changes in the energy requirements.

What should a robot minimize? It is easiest to discuss this question in the context of steady horizontal locomotion. If the robot needs to travel a given distance, perhaps it

should travel in a manner that minimizes the total battery energy required to travel this distance. Minimization of the total energy cost per unit distance is equivalent to selecting the speed that maximizes the distance traveled on a given energy budget. So an energy-optimal speed can be determined which minimizes the total energy cost per unit distance for walking. In humans, self-selected walking speeds tend to be close to 1.30 ms^{-1} [54, 55].

The walking speed is just one variable among the infinitely many that is required to completely characterize how a robot moves. There is evidence that animals (humans) choose other variables in an energy optimal manner which can be used in robotics. For any given speed, humans select the stride-length [52,56–59] that seems to minimize the metabolic cost. Humans seem to be able to do constrained energy-optimization dynamically, as the situation requires. For instance, the relationship between speed and step length is different for different constraints and the particular relationship seems to be consistent on an average with the optimization of metabolic cost subject to the specific constraints [55]. This suggests that humans (and animals) have evolved an ability to quickly find the optimum energy even in unfamiliar and novel situations, rather than be energy efficient in only the more often used tasks such as steady unconstrained locomotion [52]. However, further experiments are needed to more thoroughly demonstrate the natural constrained optimization capabilities of humans in strange and unfamiliar situations. This subject inspires the development of robots with adjustable structure e.g., artificial tendons with ability to adjust the stiffness.

1.2.4 Energy efficiency in bipedal walking

In this section, more documents are reviewed to support the idea of using adjustable stiffness artificial tendons in the stance leg of the bipedal walking robot to improve the energy economy during locomotion.

Current developments in efficient legged robots are often inspired by ideas from nature.

These ideas influence the configuration, design and sometimes structural properties of the robots. In legged locomotion, collision, i.e. when the leg touches the ground, occurs naturally and frequently. In human walking, part of the kinetic and potential energy from the body during collision is transiently stored as elastic strain energy and later released during the rebound phase by elastic recoil [39]. This phenomenon greatly reduces the work required from the muscles and lowers the metabolic cost of locomotion [60, 61]. The mechanics of elastic recoil were also studied for running and it was found that, the forward kinetic energy of the body's center of mass is in phase with fluctuations in gravitational potential energy [62]. It was also found that, humans and animals most likely store the elastic strain energy in muscles, tendons, ligaments and perhaps even bones, thereby reducing the fluctuations in total mechanical energy [62]. It has been reported that the leg stiffness influences many kinematic variables such as stride frequency and ground contact time [41, 63]. Thus, the stiffness of the leg is a key parameter in determining the dynamics of locomotion [47]. He and Farley [64, 65] suggested that the inherent properties of the musculoskeletal system determine an animal's choice of leg stiffness. Their idea was supported by Roberts et al. [66] who illustrated that the muscles of running turkeys undergo very little change in length during ground contact. Thus, the tendon may contribute most of the compliance of the muscle-tendon unit and greatly influence the leg stiffness [67].

In the context of developing the legged robots, implementation of the adjustable leg stiffness in a running robot has been recommended by researchers to improve the performance on varied terrain [47]. Besides allowing the robot to accommodate different surface conditions, the adjustable leg stiffness would permit a robot to quickly adjust its stride length to avoid obstacles on rocky and uneven surfaces.

Research is also plentiful in the area of series elasticity. Many of the ideas, problems and solutions of series elasticity related to this thesis are initiated and discussed in the publications of the MIT leg lab [1, 15–17]. Beyond the basics, much of the current

research in series elasticity addresses topics such as human centered robotics [20], running robots [21, 22] and moving in rough terrain [68].

Researchers studied the basics of the compliant legged locomotion [3–5]. Jena Walker II [69] was developed at the University of Jena by continuing the research on efficient locomotion using elasticity. However, the stiffness of the elastic elements in Jena Walker II is not adjustable. The electro–mechanical Variable Stiffness Actuation (VSA) motor developed by Bicchi and Tonietti [23] of the University of Pisa is designed for safe and fast physical human/robot interaction in manipulators. The series elastic actuator [16] was developed at the MIT leg lab which is feasible in bipedal walking robots [70]. A series elastic actuation system based on the Bowden–Cable was developed at the University of Twente by Veneman et al [71] for manipulators. The idea of controlling the compliance of a pneumatic artificial muscle to reduce the energy consumption of the robot is demonstrated by Vanderborght et al [72]. Most of the recent research on compliant locomotion is reported by Geyer [6]. Van Der Linde [73] studied the effects of active leg compliance on passive dynamic walking and showed that it can reduce the hip velocity change and as a result reduce the impulsive forces during collision. His studies were performed through computer simulation using a simplified model of a passive walker. Different devices with adjustable stiffness have been made by researchers. The AMASC (Actuator with Mechanically Adjustable Series Compliance) [21] has been developed at Carnegie Mellon University. At the Vrije Universiteit Brussel, the Robotics and Multibody Mechanics research group has developed the PPAM (Pleated Pneumatic Artificial Muscle) [74] which is used in the biped Lucy [75]. At the University of Pisa, Italy, the Variable Stiffness Actuator (VIA) [76] is developed. A biologically inspired joint stiffness control actuator[77] is developed at Georgia Institute of Technology. Sugar and his group in the Department of Mechanical and Aerospace Engineering of the Arizona State University developed the 'Jack Spring' concept [78]. Jack Spring is an adjustable robotic tendon which can be used in gait assisted devices

for artificial legs or prosthetic device. Hugh Herr and his group in Biomechatronics Laboratory at the MIT Media Lab are employing series elasticity in their successful prototypes in human locomotion assistive devices [79–82]. They illustrated that using compliant actuators improves the efficiency of locomotion in lower limb amputees [83–86]. Then there is a large mainstream literature on mechanics of walking and running. A detailed discussion of this literature is beyond the scope of this thesis. A part of this literature attempts to model humans, or parts of humans, in great detail. These models tend to have a large number of degrees of freedom. Body segments are approximated as being rigid. Muscles might have realistic origins and insertions [87], but have simplified Hill-type transient properties [88]. Contact is typically modeled with stiff springs and dashpots. Impressive whole body models have been assembled and various analyses performed. The building of such complex models have been made easier by the development of various software, for example, SIMM [89], that combines musculoskeletal modeling capability with a dynamics package. These models have been made to track human motion capture data [90] using inverse dynamics calculations. Detailed models have also been used in large-scale optimization calculations to predict the dynamics of human motion. Unfortunately, there exists insufficient understanding of the many components that such complex models require, for instance, in vivo muscle behavior is not understood well enough. Further, complex models typically imply high computational cost. Alexander made significant efforts in understanding the energy economy of human and animal locomotion [91–98]. Kuo and his colleagues developed different simple models of bipedal walking and studied the energetics of human locomotion [39, 58, 99–102]. Ruina and his colleagues are studying to understand the mechanics of low cost legged locomotion through the development of a simplified model [59, 103–108]. The mathematical models in this thesis are simple. The hope here is to understand, in detail, the consequences of energetic considerations in the context of these simple models. A vast number of simple models for legged locomotion have

been presented in papers as well as in books by Alexander [91–98]. This thesis draws much from this literature.

Some major issues have been addressed in previous research using simplified model of bipedal walking. However, the idea of adjusting and/or controlling the stiffness of artificial tendons, bringing the mathematical model of the mechanical design concepts into the model of the biped, and regulating the speed of the biped by controlling the elastic energy through the leg's stiffness are the novel issues which will be addressed in this thesis.

1.3 Objective and layout of the thesis

The general objective of this thesis is to study the effects of adjustable stiffness elastic elements on energy economy and control of the bipedal walking robots. The organization of this thesis is as follows:

Chapter 1 gives a brief introduction to the motivation of the thesis. It presents detailed background material and related work covering general ideas of series elastic actuators, adjustable stiffness elastic elements, and efficient bipedal walking methods. It also includes a summary of the objectives and expected contributions.

Chapter 2 describes the design, configuration, and control method of the ACSEA. Conceptual design of an automated adjustable stiffness coupling (AASC) with the capability of adjusting the stiffness in a wide range is introduced. Then, an Adjustable Compliant Series Elastic Actuator (ACSEA) is developed by adding the AASC between an elastic actuator and the load. A novel force control method is developed for ACSEA by using the velocity control mode of the electric motor instead of using the current control mode. The advantages and limitations of the proposed control method are studied using dynamic modeling and simulations.

Chapter 3 introduces conceptual designs of three mechanisms of an adjustable stiff-

ness artificial tendon (ASAT) to evaluate the idea of using adjustable stiffness series elasticity in bipedal walking robots. The effects of adjustable stiffness artificial tendons on the energetics of bipedal walking during the collision phase are studied. A simplified model of bipedal walking is proposed to pursue the study. Then, dynamic modeling of the robot in collision phase is developed. ASAT is considered at the ankle joint of bipedal walking which can store part of the kinetic energy of the biped during continuous motion of the collision phase.

Chapter 4 studies the effects of stiffness adjustment on energy economy of bipedal walking during the stance period and consecutive walking steps. A new simplified model of bipedal walking is also proposed. Then, dynamic modeling of the biped in stance phase is developed. OLASAT, one of the proposed design concepts of ASAT, is defined to be installed at the ankle joint of bipedal walking model which can store part of the kinetic energy of the biped during the collision phase and return that energy during the rebound phase. It consists of computer simulations to demonstrate the influence of properly and poorly adjusting the stiffness of OLASAT during the single support stance phase.

Chapter 5 provides the energy loss calculation during the foot-touch-down using mathematical model of the biped. It proposes a controller to automatically adjust the stiffness of OLASAT. It also shows the normalized formulation of the equations of the motion of the biped. Then, the detailed development of the speed tracking controller is provided followed by an analysis of the local stability of the biped. This chapter consists of computer simulations to demonstrate the performance of the combination of controllers during the stance phase.

Chapter 6 summarizes the conclusions of this research and contains follow-up research ideas.

Chapter 2

Adjustable Compliant Actuator

The actuation system is a crucial element in bipedal walking robots. MIT Leg Lab introduced and developed series elastic actuators [1, 16] for the development of bipedal and humanoid robots. Their major objectives of developing a special actuation system for bipedal walking robots were to increase the efficiency of the robots as well as to create natural looking motion (similar to human walking). However in order to improve the energy economy of a robot, the current actuation methods should be modified, a task that can be extremely challenging.

To address such objectives, several important issues need to be investigated. Most of the current studies have focused on the motion generation and optimal trajectory design for better energy economy and natural looking motion. Mechanical design of the actuator plays an important role in improving bipedal walking performances. A novel actuation system similar to the human muscle includes two major properties, series elasticity and more importantly, adjustable stiffness with series elasticity. Development of an effective force control method for such an actuator is also important.

The objective of this chapter is to propose such an actuation method for bipedal walking robots. The important issues, recommended by Williamson [16], that have not been investigated completely in previous literature are to be considered. In this chapter, a

novel mechanism named Automated Adjustable Stiffness Coupling (AASC) is designed and developed which gives the advantage of adjusting the stiffness of the actuator over a wide range. None of the current actuation systems can provide this capability. Dynamic modeling of the actuator is determined accordingly. The velocity control mode is employed inside the torque control loop to provide an accurate force/torque source. Since the velocity control mode is accurate (using feedback sensors such as tachometers and encoders) and is robust to stiction, the performance of the actuator will be improved consequently. In addition, force control using the velocity control mode operates better under the effects of the amplifier saturation by controlling the desired power of the DC motor. In this work, the physical stiffness of the actuator is not adjusted during the force control. Finally the performance of the actuator is examined by applying some test conditions on the actuator. In this work, the actuation concept is developed and evaluated through simulation, and physical implementation will remain as a follow-up study of this work.

2.1 Adjustable Compliant Actuator Approach

An actuation approach, referred to here as the Adjustable Compliant Series Elastic Actuator (ACSEA), is proposed in this chapter. The ACSEA approach employs several parts including batteries, power amplifier, actuation, transmission, controller, and Automated Adjustable Stiffness Coupling (AASC), this latter being in series with external load as shown in Figure 2.1. The major elements of ACSEA are described in the following sections.

2.1.1 Actuation

Different actuation methods can be employed in bipedal walking robots. Hydraulic actuators have limitations in terms of the required weight for instruments, oil leakage, friction, and stiction, but have the benefits of high power-to-weight ratio and large

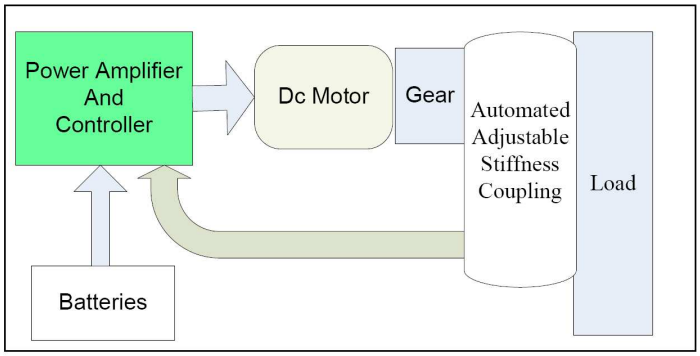

Figure 2.1: Schematic diagram of the compliant actuator.

bandwidth. Pneumatic actuators are inherently springy and compliant but have some difficulties in control and mobile applications and they are energy inefficient. Electrical actuators can be precisely controlled with the additional benefits of safety, high force-to-weight ratio (using high ratio transmission) and mobility. For these reasons, the electrical actuation system has been chosen for study in this thesis.

2.1.2 Speed reducers

Using a high gear ratio transmission, servo motors provide high force-to-weight ratio at the expense of lower efficiency caused by speed reducer deficiencies. Based on the requirements of each application, such as available space and mechanical configuration of the robot, different types of speed reducers can be used. The first choice can be a cable speed reducer that can be built with no backlash, is light-weight, and has low inertia. The second choice is a ball screw speed reducer which provides low friction, high gear ratio, linear motion, and no backlash. The third choice is a spur speed reducer which is inexpensive and has parallel input-output shaft but has backlash with high inertia. The final choice is any combination of the above speed reducers. The ball screw is chosen in this work because of its higher efficiency with no backlash.

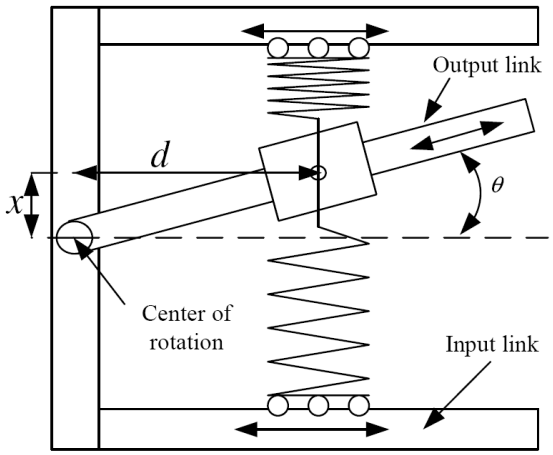

Figure 2.2: Schematic diagram of the AASC. Input and output links are concentric. Springs can be positioned along the input link to adjust the distance d. Springs are pin jointed on a linear bearing which has free sliding motion along the output link.

2.1.3 Automated Adjustable Stiffness Coupling

Perhaps one of the most challenging elements of ACSEA is the Automated Adjustable Stiffness Coupling (AASC). AASC is specially designed in this work to provide a wide range of stiffness. Adjusting the mechanical stiffness obviously increases the efficiency of locomotion in walking machines with benefits of storing and returning energy during contacts in each step. In addition, the links of walking robots can rotate passively with very low stiffness. AASC is installed between the output shaft of the DC motor's gearbox and the load, and hence the effective inertia of the load is isolated from the DC motor by AASC. While the performance of the actuator is maintained by the maximum power and the torque of the DC motor, the overall stiffness of the AASC adds some performance limitations such as creating flexible modes and lowering the bandwidth of the closed loop torque controller.

A schematic diagram of AASC is given in Figure 2.2. In the proposed design, two compression springs are intentionally inserted between the two concentric input and output links. The position of the springs with respect to the center of rotation, d, can

be adjusted automatically using a mechanism that will be explained later. Thus using this mechanism, the internal torque, T, between two concentric links is:

$$T = K_{spring} x d = K_{spring} d^2 \tan\theta \tag{2.1}$$

where θ is the angular displacement between the input and output links, x is the spring deflection and K_{spring} is the stiffness of each spring (compressional springs are used in each side of the output link). The stiffness of the coupling, K_s can be determined from:

$$K_s = \frac{T}{\theta} = K_{spring} d^2 \frac{\tan\theta}{\theta} \tag{2.2}$$

By adjusting the displacement of the springs to the center of rotation from $d = d_1$ to $d = d_2$, the ratio of the stiffness of the coupling is as follows:

$$\frac{K_{s1}}{K_{s2}} = \frac{K_{spring} d_1^2 \frac{\tan\theta}{\theta}}{K_{spring} d_2^2 \frac{\tan\theta}{\theta}} = \frac{d_1^2}{d_2^2} \tag{2.3}$$

For example, if d with an initial value of $d_1 = 20mm$ changes to the final value of $d_2 = 1mm$, the stiffness of the coupling decreases by 400 times that shows the capability of adjusting the stiffness in a wide range with a moderate change in d. From the mechanical design point of view, as shown in Figure 2.3a, AASC consists of an input link (Figure 2.3d), an output link (Figure 2.3c), two compression springs, and a spring positioning mechanism (including a ball screw, a nut, and a guiding shaft) that is installed at output link of AASC. The input and output links are concentric and a potentiometer measures θ. Two helical compression springs are located inside the spring housing as shown in Figure 2.3c. The spring housing is linearly positioned by a non-back drivable ball screw and nut, which in turn, is connected to the input link as shown in Figure 2.3d. By changing the position of the spring housing, the distance d (shown in Figure 2.2) can be adjusted. The ball screw which is attached to the input

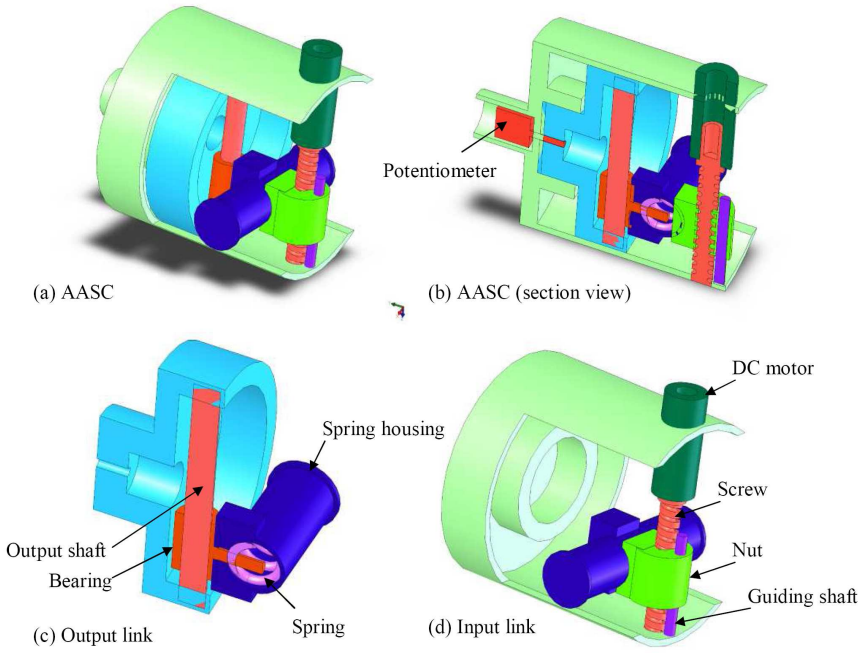

Figure 2.3: 3D model of the automatic adjustable stiffness coupling.

link (shown in Figure 2.3d) is driven by a DC motor. The angular motion of the DC motor is converted to a linear motion by a ball screw, a nut, and a guiding shaft that is installed at input link parallel to the ball screw.

As shown in Figure 2.3c, the bearing can slide at output shaft which in turn is attached to the output link. The Bearing is also hinged to the spring housing. It also has sliding motion inside the slot deployed in the spring housing. Consequently, with a relative torque on the links, the bearing slides inside the spring housing and converts the angular motion between the links to the linear motion of the springs. The force produced as a result of the deflection of the compression spring creates the torque through the output shaft via bearing, Figure 2.3c.

In summary, the unique design of AASC provides a wide range of stiffness with moderate change of d. This capability can potentially increase the performance of robotic systems in which require a quick change in stiffness.

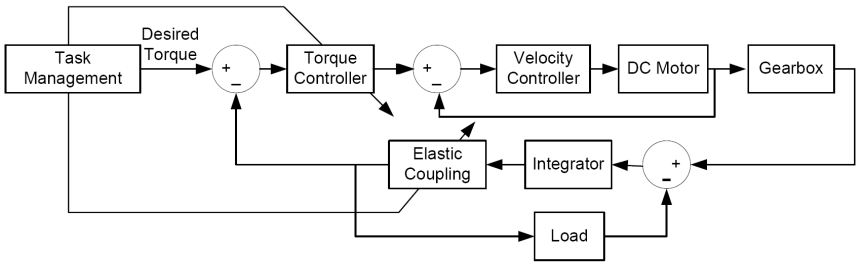

Figure 2.4: Schematic diagram of the actuator and controllers in a robotic system.

2.2 Control approach

Dynamics and control of the actuator are important issues that are explained in detail in this section. Figure 2.4 containes the schematic diagram of the control structure of the actuator in a robotic system. For given motion specifications, the task management block, shown in Figure 2.4, computes the desired torque of the actuator as well as the desired stiffness of the coupling.

In conventional torque controllers, the torque error commands the current of the DC motor through an amplifier. However in this work, based on the desired torque and the torque error, the torque controller block commands the desired velocity of the DC motor (shown in Figure 2.4). Since the velocity control mode is accurate (using feedback sensors such as tachometers and encoders) and is robust to stiction, the performance of the actuator will be improved consequently. The velocity controller block would close the fast inner loop to ensure that the actuator follows a desired velocity value. In the next section, more details about the implementation of the control method are described.

2.3 Actuator as a torque source

Using special mechanical characteristics of ACSEA, the control approach seeks to exploit actuation's unique characteristics to construct a near perfect torque source. The

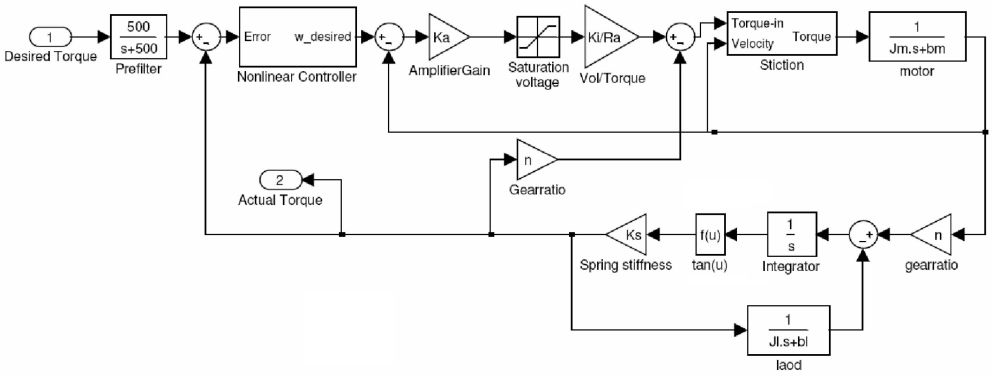

Figure 2.5: Control block diagram of the actuator in Simulink.

characteristics of a perfect torque source, consisting of zero output impedance and infinite control bandwidth, would enable an actuator to possess the characteristics necessary for the bipedal walking robots. While a perfect torque source is impossible to achieve, a nearly perfect torque source that can offer some of the advantages of the perfect torque source is described here.

The block diagram of the actuator model in Simulink is shown in Figure 2.5. A prefilter block is located after the desired torque signal to smooth the input signal. Based on the desired torque (after prefilter block), torque error (as shown in Figure 2.5) is commanded to a torque controller block that is usually a nonlinear controller. Afterward, the torque controller block commands a desired velocity (w_desired) to the DC motor. In the velocity controller loop, the difference of the desired velocity signal (commanded from the torque controller block) and the actual velocity of the DC motor is amplified and is followed by a saturation operator. Then, the saturated voltage signal is converted to the torque of the DC motor as shown in Figure 2.5. The difference of the produced torque of the DC motor and the torque of the actuator at transmission is then applied to the stiction block and finally to the motor impedance that gives the actual velocity of the DC motor. The output velocity of the DC motor after transmission is subtracted from the load's velocity. Deflection of AASC is multiplied by its

stiffness which gives the actual torque of the actuator. The velocity control mode and its performance specifications are detailed in the next section.

2.3.1 Velocity control mode: implementation and limitations

Nowadays, velocity control of the DC motors is a conventional routine in robotics and automation industry by using amplifiers and velocity feedback sensors (such as encoders and tachometers). The effects of coupling-load interaction dynamics in the velocity control mode are investigated here as one of the major concerns of ACSEA. Since an electrical DC motor is chosen as a power source in the actuator, the dynamic model of a DC motor is given below.

The electrical DC motor is an electromechanical transducer with the following relations.

$$E = R_a I + K_{emf}\omega \tag{2.4}$$

$$T_m = T_{load} + (J_m S + b_{vis})\omega \tag{2.5}$$

$$T_m = K_i I \tag{2.6}$$

The parameters T_m, R_a, I, E, and ω are DC motor output torque, winding resistance, applied current, voltage, and motor shaft angular velocity, respectively. K_i is the electromechanical conversion coefficient which equals the ratio of the DC motor's torque to current. The parameter K_{emf} is the back electromotive force constant. In practice, the moment of inertia of the rotor, J_m, and the viscous damping ratio, b_{vis}, are measured while the electrical winding is open. T_{load} is the external torque over the output shaft of the DC motor and its value depends on the transmission type. For back drivable transmissions: $T_{load} = \frac{n_g T_l}{\mu_g}$, where T_l is the actual torque of the actuator. n_g and μ_g are the gear ratio and the transmission efficiency, respectively.

Using the above relations, the transfer function of the DC motor is:

$$\omega = \frac{\frac{K_i}{R_a}E - T_{load}}{J_m S + b_{vis} + \frac{K_i K_{emf}}{R_a}} \tag{2.7}$$

The closed loop transfer function of the velocity control loop is:

$$\frac{\omega}{\omega_d} = \frac{K}{Z_m + \frac{n_g^2}{\frac{S}{K_s}+\frac{1}{Z_l}} + K} \tag{2.8}$$

where K_s is the coupling stiffness. Parameters Z_m and Z_l are the motor and load impedances, respectively. The values of Z_m, Z_l and K are given below:

$$Z_m = J_m S + b_m \tag{2.9}$$

$$Z_l = J_l S + b_l \tag{2.10}$$

$$K = \frac{K_a K_i}{R_a} \tag{2.11}$$

where K_a is the amplifier gain. The damping ratio of the DC motor, b_m, which includes viscous, b_{vis}, and, back electromotive force damping is given below:

$$b_m = b_{vis} + \frac{K_i K_{emf}}{R_a} \tag{2.12}$$

By replacing the above parameters in Eqn.(2.8), the closed loop transfer function of the velocity control loop is given below:

$$\begin{aligned} \frac{\omega}{\omega_d} \quad = \quad & \frac{K(J_l S^2 + b_l S + K_s)}{J_l J_m S^3 + (J_m b_l + J_l b_m + J_l K)S^2 + (J_m K_s + b_m b_l + n^2 K_2 J_l + K b_l)S + } \\ & \overline{+ b_m K_s + n_g^2 b_l K_s + K K_s} \end{aligned} \tag{2.13}$$

The linear transfer function in Eqn.(2.13) is valid for a small θ. Coulomb friction and stiction are dramatically affected by introducing the AASC. Stiction is considered

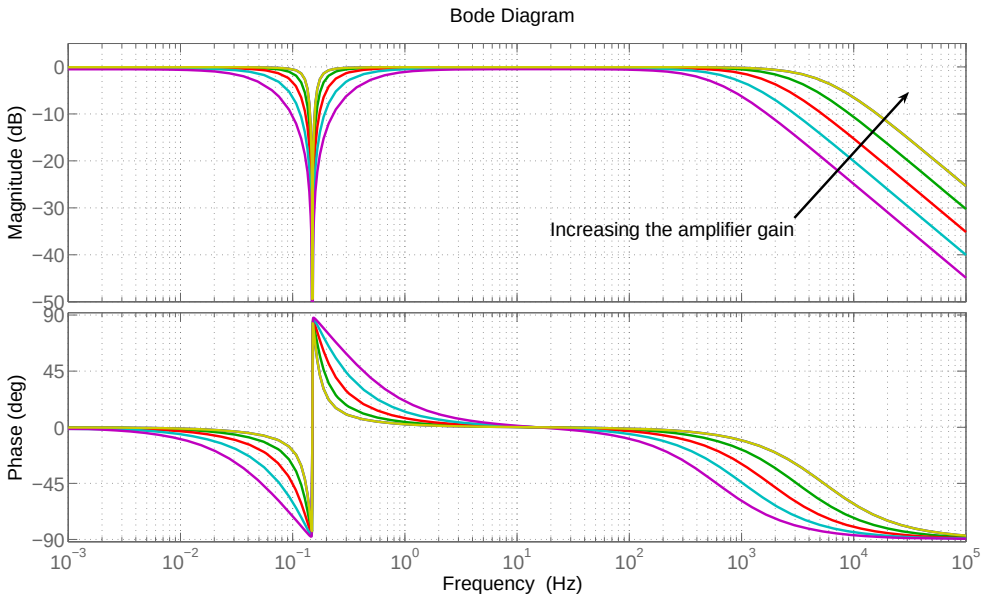

Figure 2.6: Bode plot of velocity control loop.

in simulations of the actuator model as shown in Figure 2.5. The parameters of the permanent magnet DC motor and the controller that are used in the simulations are listed in Table 2.1.

Due to the effects of the flexible modes, the transfer function, Eqn.(2.13), has two complex zeros and two complex poles. Also the transfer function has one real pole caused by the DC motor's inertia and damping. Since flexible modes of the load are lightly damped, frequency responses of the system in Bode plot exhibit a sharp peak and a notch on the phase response plot and exibit a sharp notch on the magnitude plot as illustrated in Figure 2.6. To reduce the peak and notch shown in Figure 2.6, it is found that increasing the amplifier gain increases the damping ratio of the system and also decreases the effects of flexible modes. Moreover, the steady state error of the system and the sensitivity of the system to the load dynamics are lowered as can be seen in the low frequency response of the system in Figure 2.6. On the other hand, increasing the saturation of the amplifier (increasing the difference between the actual and the saturated signal) is equivalent to decreasing the amplifier gain whenever the amplifier is

Parameter	Definition	Values
K_i	Torque constant	7.88 mNM/A
J_m	Motor moment of inertia	11.3 gcm^2
b_m	Motor viscous damping	0.011 $\frac{mNMsec}{rad}$
R_a	Motor winding resistance	0.309Ω
J_l	Load moment of Inertia	113 Kgm^2
b_l	Load viscous damping	0.1 NM/sec
n_g	Gear ratio	0.01
$\frac{K_s}{tan\theta}$	Coupling stiffness	100 NM/rad
x	Spring deflection	0 to 10 mm
d	displacement	0 to 40 mm
ρ_s	Spring stiffness ratio	$\frac{d_1^2}{d_2^2}$
K_p	Proportional gain	5
K_I	Integral gain	1
K_a	Amplifier gain	1.5
k	Torque controller gain	100

Table 2.1: Parameters of the actuator employed in simulations.

saturated. Thus to keep the performance of the system, saturation has to be prevented. Preventing saturation is possible by setting limitations for the commanded velocity signal which is directly related to the gains of the torque controller. In addition, the task manager block, shown in Figure 2.4, should be reasonably designed by dictating desired torque values with respect to the actuator's limitations. For example by increasing the frequency of a desired torque signal, magnitude of a signal must be decreased. The next section explains the torque controller.

2.3.2 Torque controller

The task manager block sets the commanded torque of the actuator. Then, the prefilter reduces the sudden changes of the commanded torque. The output torque of the actuator is measured from the coupling's angular deformation θ. By subtracting the desired torque from the actual torque of the actuator, the torque error is commanded to the torque controller unit as shown in Figure 2.5. The torque controller unit is designed by considering the following facts: 1- The maximum angular velocity of the DC motor

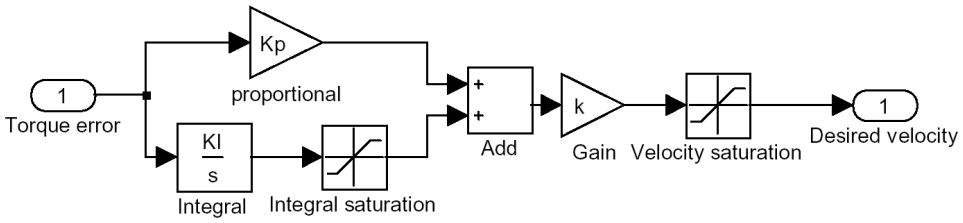

Figure 2.7: Schematic diagram of the nonlinear torque controller.

is limited as a result of amplifier saturation. 2- The power of the DC motor is limited. 3- The stiffness of AASC can be adjusted by employing the following equation.

$$K_s = \rho_s K_{spring} \quad \rho_{min} < \rho_s < \rho_{max} \tag{2.14}$$

Parameter ρ_s is determined from the distance between the spring position and the center of rotation as mentioned in Eqn.(2.2). Proportional-Integral controller is used to compensate the torque error. Figure 2.7 illustrates the schematic diagram of the torque controller unit. As shown in Figure 2.7, there are two different saturation operators in the torque controller unit. The first saturation operator limits the output of the integrator that is called integral saturation operator in this thesis. The second saturation operator limits the output magnitude of the controller that saturates the desired velocity signal and is named velocity saturation operator in this thesis. The velocity saturation operator limits the commanded desired velocity below the maximum angular velocity of the DC motor. Here, the gain $k = 100$ is assumed to be constant. Proportional and integral gains of the controller, K_p and K_I, are determined by trial and error to improve the response of the actuator to a step torque input, and are listed in Table 2.1. The next section explains the effects of the saturation operators on the performance of the system.

2.4 Saturation effects on performance

One significant deviation from the ideal model occurs when the actuator saturates. Saturation of ACSEA represents the threshold above which the DC motor can no longer compensate for the phase and the magnitude errors of the actuator since the amplifier could not produce enough current to compensate the velocity error.

As mentioned before, reducing the amplifier and controller gains can significantly reduce the performance of the torque controller. In addition, each saturation operator can be replaced by an equivalent gain in linear analysis which is described in section 2.4.1. Thus to evaluate the performance of the system, sensitivity of the actuator as a torque source to the saturation operators should be studied. The range of changing the equivalent gains can be determined as an index to show the sensitivity of the actuator to each saturation operator. Thus in the next section, the range of change of the equivalent gain of each saturation operator is calculated.

2.4.1 Substituting the saturation with an equivalent gain

The saturation operators in the torque control unit and in the DC motor amplifier have the same form of nonlinearity, which is time-invariant and single valued, and lies in a sector $[a; b]$ as shown in Figure 2.8. The general configuration of a saturation operator is shown in Figure 2.8. The saturation operator output, u_o, is limited to the following range $u_l < u_o < u_h$. Also the input of the saturation operator, u_i, is limited as follows: $u_{lmin} < u_i < u_{lmax}$ where the parameters of u_{lmin}, u_{lmax}, u_l and u_h are constant values. Each saturation operator is considered to be an equivalent gain in the linearized form of the system. For small inputs the saturation operator is inactive, and the equivalent gain of the saturation operator equals b (as shown in Figure 2.8). While the saturation operator is active, the equivalent gain K_{sat} is bounded between $0 \leq \frac{u_h}{u_{lmax}} < K_{sat} < b$. For simplicity of analysis, in this thesis the gain b has the value of 1. The closed loop

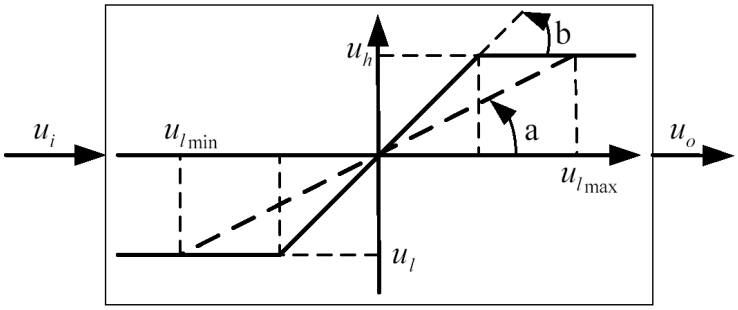

Figure 2.8: Schematic diagram of a saturation operator.

gain of the actuator depends on the equivalent gains of the saturation operators. Thus, the range of the equivalent gain of each saturation operator is defined in this section. The maximum and minimum values of the desired torque, T_{dmax} and T_{dmin}, are limited to the maximum possible torque, $K_i I_{max} n$, provided by the DC motor. I_{max} is the maximum current of the DC motor and is determined by the amplifier saturation. The torque error in the system, e_T, is limited by $|e_T| \leq (T_{dmax} - T_{dmin})$. With the above considerations for each saturation operator, the range of equivalent gains are defined as follows:

1- Equivalent gain of the integral saturation operator is limited by:

$$0 \leq \frac{u_{hint}}{u_{lmaxint}} \leq K_{satint} < b \tag{2.15}$$

where u_{hint} and $u_{lmaxint}$ are the maximum output and input values of the integral saturation operator respectively. The maximum input signal of the integral saturation operator, $u_{lmaxint}$, can be very large. Thus by increasing the input signal, the integral saturation operator decreases the effects of the integrator on the controller by reducing the equivalent gain of the integrator. On the other hand, the integral saturation operator limits the maximum output value of the integral controller. This is important to

Parameter	**Values**
u_{hint}	5
u_{lint}	-5
u_{hvel}	1025 rad/sec
u_{lvel}	-1025 rad/sec
u_{hvol}	12 V
u_{lvol}	-12 V
T_{dmax}	30 NM
T_{dmin}	-30 NM

Table 2.2: Parameters of the saturation operators employed in simulations.

keep the stability of the system with respect to the integral–windup.

2- The equivalent gain of the velocity saturation operator is limited by:

$$0 \leq \frac{u_{hvel}}{k(K_p(T_{dmax} - T_{dmin}) + u_{hint})} \leq K_{satvel} < b \tag{2.16}$$

where u_{hint} and u_{hvel} are the maximum output values of the integrator and of the velocity saturation operator respectively. The integral saturation operator limits the output of the integral controller and thus decreases the effects of integral–windup on the velocity saturation operator.

3- The equivalent gain of the voltage saturation operator is limited by:

$$0 \leq \frac{u_{hvol}}{K_a(u_{hvel} + \omega_{max})} \leq K_{satvol} < b \tag{2.17}$$

where ω_{max} is the maximum angular velocity of the DC motor, 1025 rad/sec, and $(u_{hvel} + \omega_{max})$ is the maximum possible error in the velocity control loop.

2.4.2 Effects of saturation on the performance of the actuator

In this section, the range of the equivalent gain of each saturation operator will be determined first. The parameters of the actuator and the saturation operators are shown in Tables and 2.1 and 2.2 respectively. The range of saturation for the voltage

saturation operator is:

$$0.0034 \leq K_{satvol} < 1 \tag{2.18}$$

The equivalent gain for velocity saturation operator is:

$$0.066 \leq K_{satvel} < 1 \tag{2.19}$$

The above ranges show that the equivalent gains can be changed over a wide range. In addition, by reducing the equivalent gain of each saturation operator, the performance of the actuator can be significantly reduced. Thus, the effects of saturation on the performance of the torque controller should be studied properly.

The Bode plot of the actuator is shown in Figure 2.9 in which none of the saturation operators are active. Thus, the equivalent gain of all saturation operators equals one. Figure 2.9 shows that the actuator can properly respond to the desired torque frequencies less than 70 hertz. Saturation is a function of the amplitude of the input signal that is not considered in the linear response of the actuator in Figure 2.9. Thus to evaluate the actuator in the presence of saturation, the frequency response of the actuator is determined using simulation. A series of sinusoidal torque signals as the input to the actuator are comanded which have constant amplitudes. Here, 50 different frequencies from 0.01 Hz to 100 Hz are commanded. Then the steady state output torque of the actuator are measured. The magnitude response of the Bode plot is calculated based on the following relation.

$$Magnitude[dB] = 20log_{10}(\frac{amp_{output}}{amp_{input}}) \tag{2.20}$$

where amp_{output} and amp_{input} are the amplitudes of the output and input torque signals respectively. Figure 2.10 shows the frequency response of the actuator for different desired torque amplitudes from 1 [NM] to 30 [NM]. As shown in Figure 2.10, even for

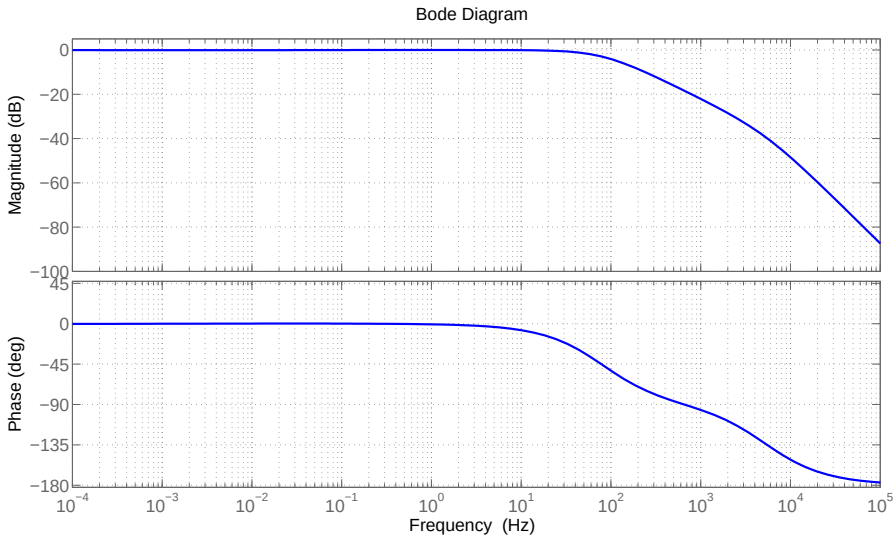

Figure 2.9: Bode plot of the force control loop of ACSEA.

the maximum desired torque, $T_{des} = 30[NM]$, the actuator can successfully follow the desired torque in low frequencies (less that 10 hertz). As shown in Figure 2.10 at high frequencies (more than 10 Hz), increasing the amplitude of the desired torque reduces the performance of the actuator as a torque controller.

2.5 Simulation examples

In this section, the overall response of the actuator to several desired torque signals is presented. Simulations are performed in SIMULINK. The parameters of the actuator and the controller used in simulations are listed in Tables 2.1 and 2.2. Figure 2.11 shows the response of the actuator to a desired torque signal in a period of 10 seconds. The desired torque signal consists of ramp, step, and continuous forms. Torque controller block of the actuator commands a desired velocity signal to the DC motor which is also shown in Figure 2.11. As shown in this figure, the actuator can successfully follow the desired torque signal. Amplifier saturation can be seen in Figures 2.11a and 2.11b in the time period of 4-5 seconds.

To better illustrate the response of the actuator, Figure 2.12 shows the response of

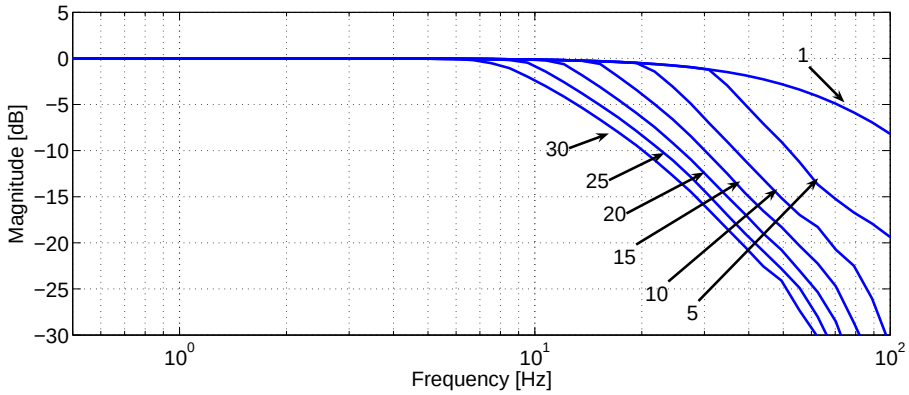

Figure 2.10: Magnitude plot of the nonlinear model of ACSEA for different desired torque amplitudes of 1, 5, 10, 15, 20, 25 and 30 NM.

the actuator to a desired torque signal in a period of 1 second. Sudden changes in the desired torque signal are assumed at time values of 0.12 sec, 0.38 sec, 0.6 sec, 0.82 sec and 0.94 sec. As shown in Figure 2.12a, overshoot and oscillations of the torque response are very low and the actuator can successfully track the desired torque signal. As shown in Figure 2.12a and 2.12b, after sudden changes in the desired torque signal, there are errors in tracking the desired torque. It is shown that the commanded velocity from the torque controller is the maximum available velocity of the DC motor, 1025 rad/sec, but the velocity response of the DC motor is not fast due to the amplifier saturation. Thus, the lag or the error in response of the actuator is caused by actuator power limitations and the proposed controller method is successful to command the proper desired velocity signal.

The above results illustrate that the actuator can successfully respond to the commanded torque signal. The results also demonstrate that the desired torque signal should be selected considering the actuator's inherent limitations.

2.6 Summary

An actuator approach for bipedal walking robots was developed in this section. The actuator was referred to here as Adjustable Compliant Series Elastic Actuator (AC-

SEA). The conceptual design of the actuator was presented in this chapter. ACSEA gives the capability of changing the stiffness of the actuator in a wide range. A new force control method was proposed for ACSEA by using velocity control mode of the DC motor instead of using the current control mode. The proposed control method is simple and accurate. By designing a nonlinear torque controller, an almost pure torque source is provided which can be used in wide range of applications. The performance of the actuator for different desired tasks was tested through simulations. The simulation results show reasonable response and provide a strong argument for the concept of this actuation system for bipedal walking robots.

In this chapter, the performance analyses of the actuator are performed for specific electrical motor and couplings parameters. Development of a model of the actuator using dimensionless parameters is recommended as follow-up of this research. Development of a prototype of the actuator is also recommended as future work to verify the control method. Simultaneous torque control of the actuator with adjustment of the stiffness of the coupling as a multi-input multi-output control problem can also be studied in future research.

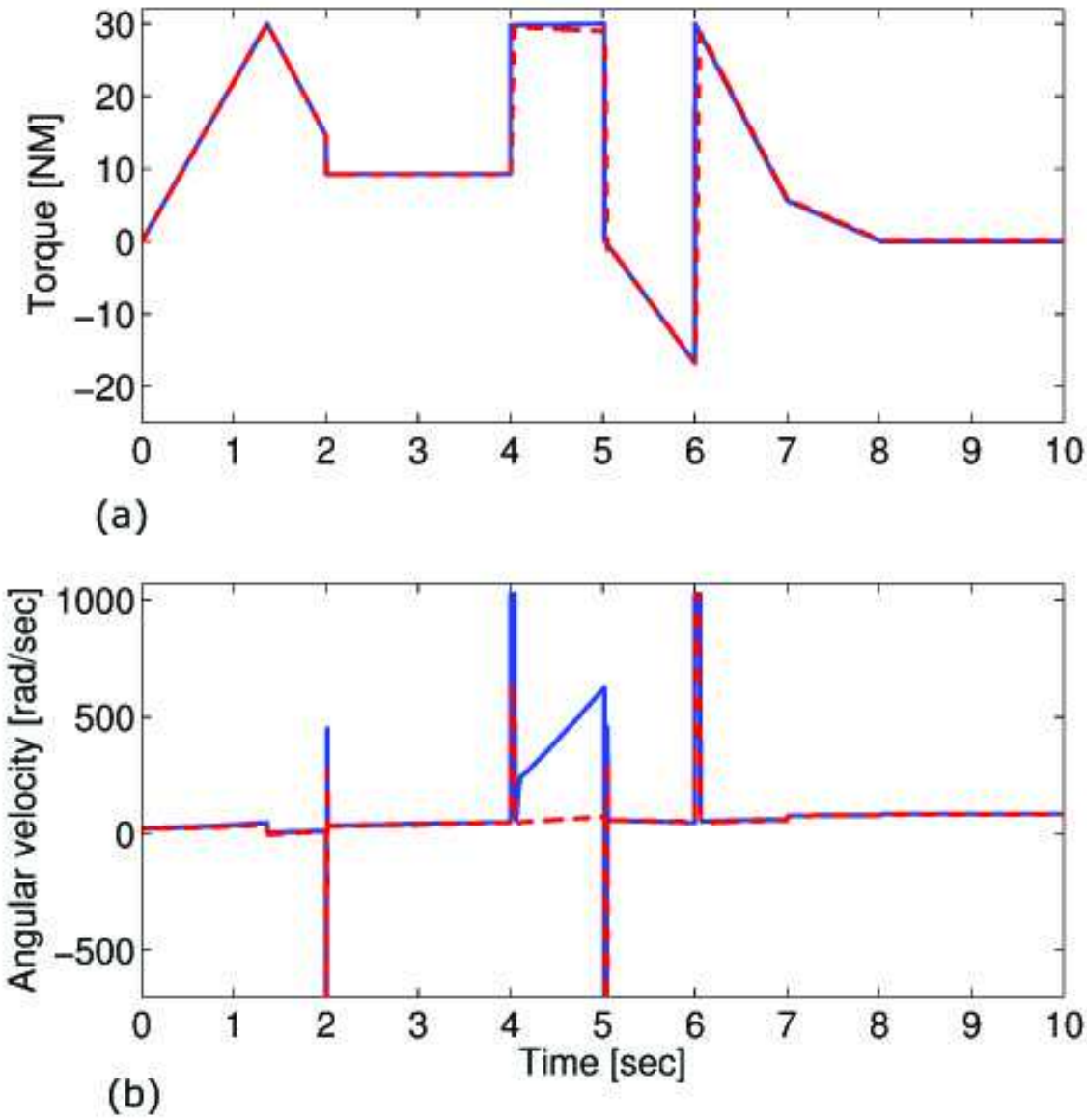

Figure 2.11: Response of the actuator in case 1. Commanded and actual torque signals are shown by solid line and dashed line respectively.

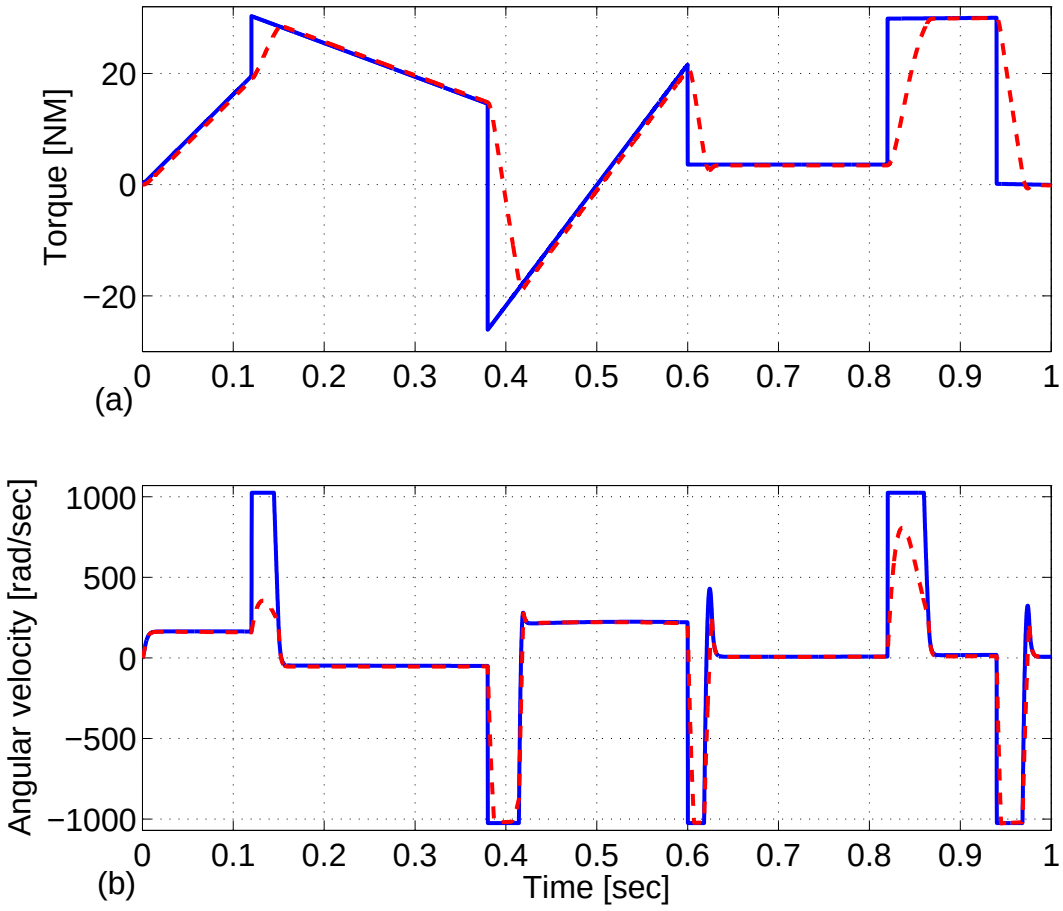

Figure 2.12: Response of the actuator in case 2. Commanded and actual torque signals are shown by solid line and dashed line respectively.

Chapter 3

Adjustable Stiffness Artificial Tendons

Researchers have developed passive dynamic walking robots in which the joints of the robot, are completely passive [26–28, 30, 31, 38]. Passive dynamic walking machines provide human-like locomotion in bipedal walking robots that is more efficient than the joint-angle-controlled robots (with active actuators at the joints). On the other hand, tuning the parameters of the passive dynamic walking robots is tricky, and time consuming, and requires much experimentation. In addition, passive dynamic walking robots still have considerable energy loss through rapid changes in the velocity direction of the center of mass of the robot during collision of the foot with the ground. Joint-angle-controlled bipedal walking robots also undergo significant energy loss caused by the rigid collision of the foot with the ground in addition to their common energy dissipation in the robot's power systems.

Collision of the foot with the ground during bipedal walking is inevitable, which is one of the major causes of the energy loss. Establishing a new technique to reduce this energy loss is a challenging problem which is addressed in this chapter by developing the idea of using the adjustable stiffness series elastic elements in the robot's structure.

This chapter constructively demonstrates the idea through two main efforts. The first effort is to develop the conceptual designs of the adjustable stiffness artificial tendons (ASAT) to show that the idea can be implemented in practice. The second effort is to study the effects of adjustable stiffness series elasticity on reducing the energy loss by adding the model of each ASAT into the robot dynamics.

The organization of this chapter is as follows. Section 3.1 describes three different conceptual designs of ASAT. In Section 3.2, advantages and limitations of each concept are explained. In Section 3.3, in order to capture the behavior of ASAT on energetics, the dynamic model of a bipedal walking robot is developed which includs a foot, a thigh, a shank, and ASAT installed parallel to the ankle joint. Then, computer simulations are carried out to demonstrate the effectiveness of each ASAT design on reducing the energy loss during the collision phase. Finally the research is summarized in Section 3.4.

3.1 Conceptual designs

In this section, three different conceptual designs of ASAT are developed. The physical prototypes of the conceptual designs have not been made in this project. The first design (Section 3.1.1) is a rotary adjustable stiffness artificial tendon that is a bi-directional tendon able to apply a torque clockwise as well as counter clockwise. The second design (Section 3.1.2) is a uni-directional linear adjustable stiffness artificial tendon that uses the concept of changing the number of active coils of two series springs. Finally, the third design (Section 3.1.3) is a combination of two offset parallel springs that is also a uni-directional tendon. The mathematical model of each tendon is also developed in this section. In Section 3.2, the advantages and limitations of each concept are discussed.

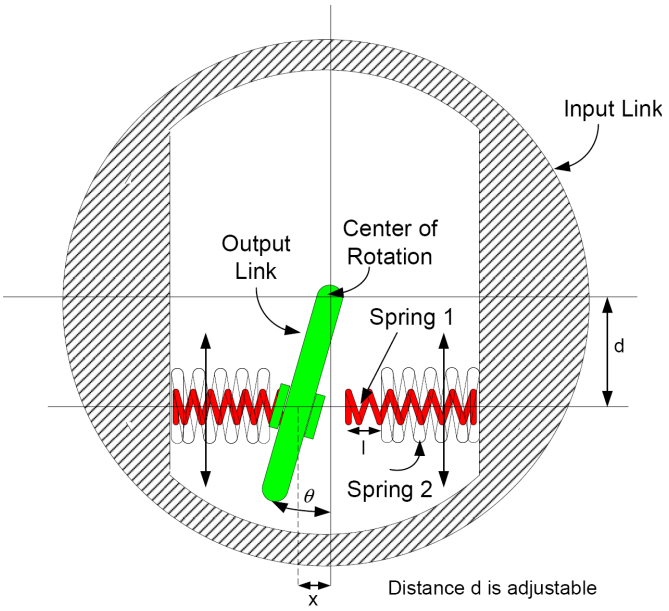

Figure 3.1: Schematic diagram of the RASAT. A pair of two compression springs (spring 1 and spring 2) with a constant offset, l, are located in each side of the output link. Input and output links are concentric, and d, the distance of the springs to the center of rotation, is adjustable.

3.1.1 Rotary Adjustable Stiffness Artificial Tendon

The Rotary Adjustable Stiffness Artificial Tendon (RASAT) is specially designed to provide a wide range of angular stiffness. The schematic of RASAT is illustrated in Figure 3.1. As shown in Figure 3.1, a pair of two parallel helical compression springs (spring 1 with low stiffness and spring 2 with high stiffness) are configured in an offset, l, and are located on each side of the output link. In RASAT, each pair of compression springs is intentionally inserted between the two concentric input and output links. Each spring pair consists of a low stiffness spring with a stiffness of K_1 and a high stiffness spring with a stiffness of K_2. The offset between the low and high stiffness springs has a constant value of l. d, the distance between the spring pairs and the center of rotation of the links, is adjustable. In this case, the internal torque T, between the

concentric input and output links is calculated from:

$$T = \begin{cases} K_1 dx = K_1 d^2 \tan\theta & \frac{l}{d} > \tan\theta \\ \\ K_1 dl + d(K_1 + K_2)(d\tan\theta - l) & \frac{l}{d} < \tan\theta \end{cases} \tag{3.1}$$

where θ is the angular displacement between the input and output links and x is the spring deflection. In Eqn.(3.1), $\frac{l}{d} > \tan\theta$ represents the situation where only spring 1 is engaged and $\frac{l}{d} < \tan\theta$ is when both springs are engaged. The stiffness of spring 2 is μ times higher than the stiffness of spring 1. Thus:

$$K_2 = \mu K_1 \tag{3.2}$$

After substituting Eqn.(3.2) into Eqn.(3.1) and dividing the resulting equation by $K_1 d_{max}^2$, the following non-dimensional form is arrived at:

$$\frac{T}{K_1 d_{max}^2} = \begin{cases} tan\theta(\frac{d}{d_{max}})^2 & \frac{l}{d} > \tan\theta \\ \\ (\mu+1)\tan\theta(\frac{d}{d_{max}})^2 - \mu\frac{l}{d_{max}}(\frac{d}{d_{max}}) & \frac{l}{d} < \tan\theta \end{cases} \tag{3.3}$$

where d_{max} is the maximum value of distance d. The effects of the distance ratio, $\frac{d}{d_{max}}$, on the output torque index, $\frac{T}{K_1 d_{max}}$, in RASAT are graphically illustrated in Figures 3.2 and 3.3 where $\mu = 5$ and $\frac{l}{d_{max}} = 0.1$. As shown in Figure 3.2, by increasing the distance, d, from zero to d_{max}, for a given θ, the torque index, $\frac{T}{K_1 d_{max}}$, increased. This relationship is shown for different amounts of θ from $\theta = 5^o$ to $\theta = 15^o$ increasing in steps of 1^o. The torque–angular deflection relation in RASAT is graphically illustrated in Figure 3.3 for different values of distance indexes $\frac{d}{d_{max}}$. The slope of each curve in Figure 3.3 is equivalent to the stiffness of the tendon. As shown in Figure 3.3, by decreasing the ratio $\frac{d}{d_{max}}$, from 1 to 0.1 with steps of 0.1, the slopes of curves are

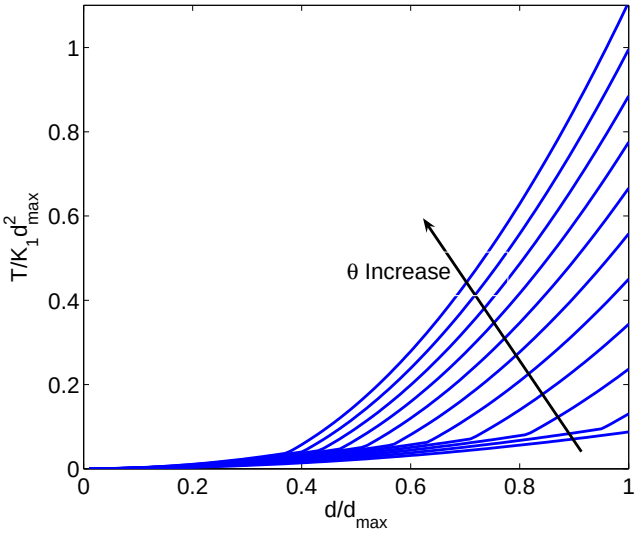

Figure 3.2: Effects of decreasing $\frac{d}{d_{max}}$ in dimensionless force–deformation in RASAT for a constant θ. θ increases in equal steps of 1^o from 5^o to 15^o.

reduced significantly. It has been shown in Figure 3.3 that the slope of the curves can be adjusted in a wide range which illustrates the capability of RASAT in wide range of the stiffness. Sudden changes in the slope of the curves in Figure 3.3 are caused by engaging the high stiffness spring. Also, the higher the ratio $\frac{d}{d_{max}}$, the sooner the sudden change occurs. The effect of the stiffness ratio of the springs, μ, on the stiffness of RASAT is illustrated in Figure 3.4 by assuming $\frac{d}{d_{max}} = 0.8$ and $\frac{l}{d_{max}} = 0.1$. Increasing the μ represents the increase of the stiffness ratio of spring 2 to spring 1. In Figure 3.4, the slope of the curves increases at the turning point, which is caused by engaging spring 2 while μ increases from zero to 5 with equal increments of 1.

From the mechanical design point of view, RASAT (Figures 3.5a & 3.5b) is comprised of an input link (Figure 3.5d), an output link (Figure 3.5c), four springs (not shown in figure 3.5 but shown in Figure 3.1), and the spring positioning mechanism that is installed on the input link as shown in Figure 3.5d. Input and output links are concentric and a relative angular deflection between the input and output links, θ, can be measured using an angular displacement sensor, i.e. a potentiometer with a

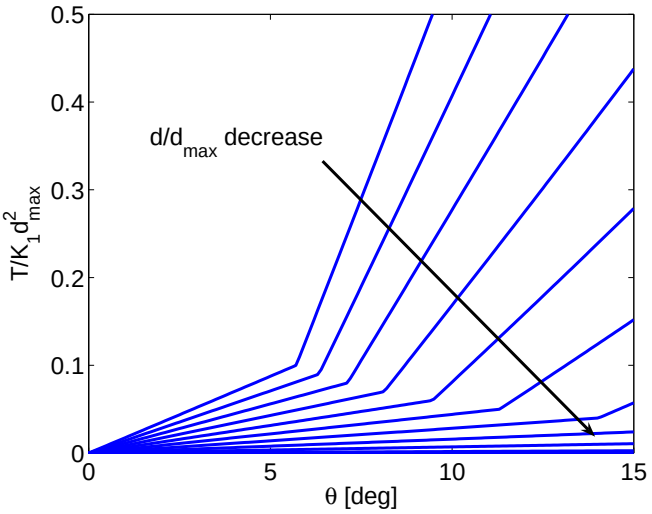

Figure 3.3: Each curve shows non–dimensional force–θ in RASAT for a constant d. $\frac{d}{d_{max}}$ decreases from 1 to 0.1 in equal steps.

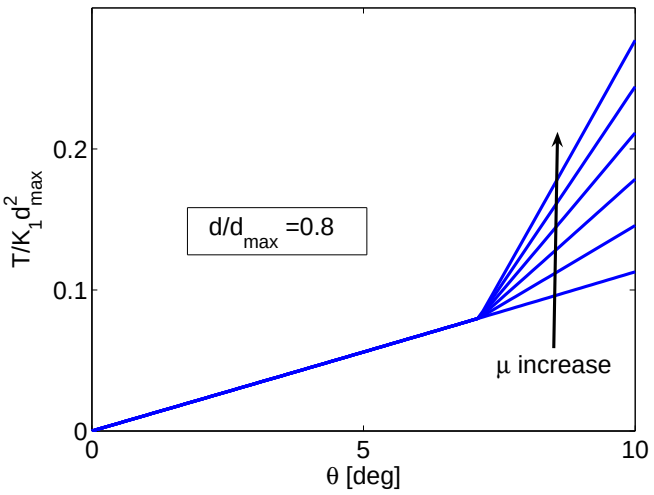

Figure 3.4: Effects of increasing μ in dimensionless force–θ in RASAT.

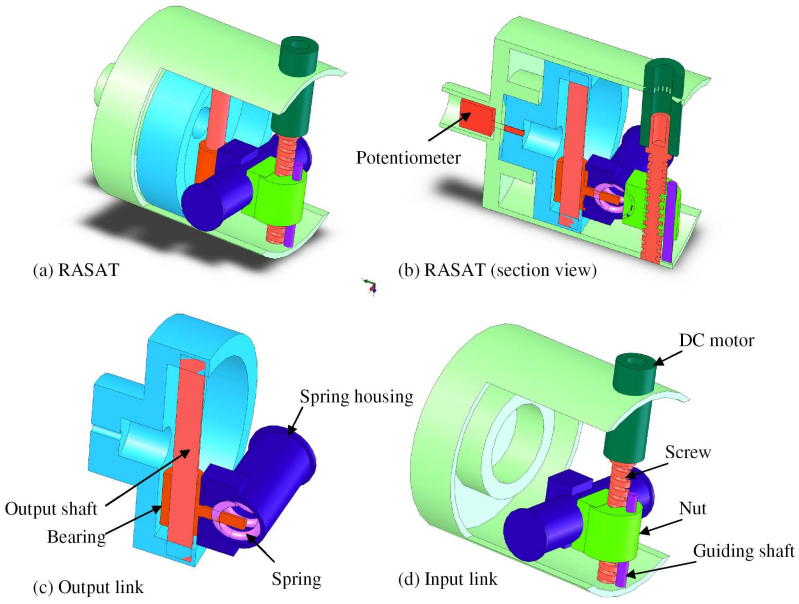

Figure 3.5: 3D model of RASAT.

low pass filter. Two pairs of parallel helical compression springs with constant offset are located inside the spring housing. The spring housing is linearly positioned by a non-back drivable ball screw and nut, which in turn, is connected to the input link. The ball screw, attached to the input link (Figure 3.5d), rotates using a brushless DC motor. Angular motion of the DC motor is converted to linear motion using a guiding shaft installed at the input link parallel to the ball screw. The distance d (Figure 3.1) between the spring housing and the center of rotation can be adjusted using the angular displacement feedback signal from an output shaft of the DC motor. A bearing (Figure 3.5c) sliding on the output shaft, which is attached to the output link, is pin jointed at the spring housing and has a sliding motion inside the slot deployed on spring housing. Consequently, with a torque on the links, the bearing slides inside the spring housing and converts the angular motion between the links to the linear motion of the springs. The resultant force caused by the deflection of the springs creates torque through the output shaft via the bearing (Figure 3.5c).

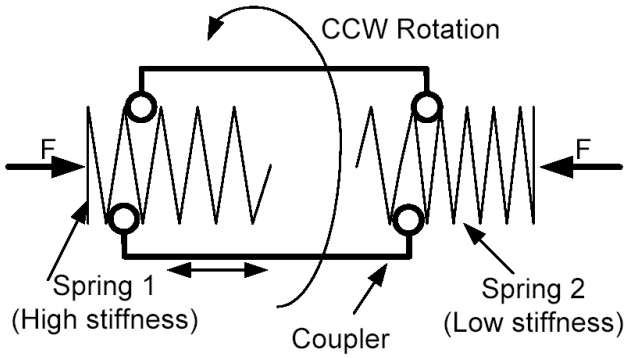

Figure 3.6: Schematic diagram of LASAT.

3.1.2 Linear Adjustable Stiffness Artificial Tendon

Linear Adjustable Stiffness Artificial Tendon (LASAT) is a uni-directional compression tendon. LASAT is a series combination of two helical compression springs. A rigid coupler that connects two series springs together is illustrated in Figure 3.6. Counter-clockwise rotation of the coupler, increases the number of active coils in spring 2 with a low stiffness and decreases the number of active coils in the spring 1 with a high stiffness; and vice versa for clockwise rotation. Springs 1 and 2 have the stiffnesses of K_{s1} and K_{s2} respectively, that are defined by:

$$K_{si} = \frac{P_i}{N_s} \qquad i = 1, 2 \tag{3.4}$$

where parameter i represents the i^{th} spring and number of spring coils, N_s, is assumed to be equal for both springs. P_1 and P_2 are the coil's stiffness of spring 1 and 2 respectively [109]:

$$P_i = \frac{dia_i^4 G_i}{8 D_i^3} \qquad i = 1, 2 \tag{3.5}$$

where D_i, dia_i, and G_i are the mean coil diameters, wire diameters and the shear modulus of the springs. By changing the position of the coupler, the number of the

active coils of spring 1 and spring 2 will be defined by $N_1 = (1-\lambda)N_s$ and $N_2 = \lambda N_s$ respectively, where $0 < \lambda < 1$. The coil's stiffness of spring 1 is assumed to be ρ times higher than spring 2, thus $P_1 = \rho P_2$.

By the above considerations, the effective stiffness of spring 1, K_{a1}, and that of spring 2, K_{a2}, are given by the following equations:

$$K_{a1} = \frac{K_{s1}}{1-\lambda} \tag{3.6}$$

$$K_{a2} = \frac{K_{s2}}{\lambda} \tag{3.7}$$

The stiffness of the springs in series, K_{eq} given in Eqn.(3.8), represents the LASAT stiffness as long as the compression of the softer spring is lower than its shut length, Ls, (where the coils are in contact):

$$K_{eq} = \frac{K_{a1}K_{a2}}{K_{a1}+K_{a2}} = \frac{\frac{P_1}{(1-\lambda)N_s}\frac{P_2}{\lambda N_s}}{\frac{P_1}{(1-\lambda)N_s}+\frac{P_2}{\lambda N_s}} = \frac{\rho K_{s2}}{1+(\rho-1)\lambda} \tag{3.8}$$

Thus, the force of the tendon is calculated by the following equations:

$$F_{LASAT} = \begin{cases} K_{eq}d_{LASAT} & d_{LASAT} \le Ls\frac{1+(\rho-1)\lambda}{\rho} \\ \\ K_{s2}Ls + K_{a1}(d_{LASAT} - Ls\frac{1+(\rho-1)\lambda}{\rho}) & d_{LASAT} > Ls\frac{1+(\rho-1)\lambda}{\rho} \end{cases} \tag{3.9}$$

and respectively in dimensionless form:

$$\frac{F_{LASAT}}{K_{s2}Ls} = \begin{cases} \frac{d_{LASAT}\rho}{Ls(1+(\rho-1)\lambda)} & \frac{d_{LASAT}}{Ls} \le \frac{1+(\rho-1)\lambda}{\rho} \\ \\ 1+\frac{\rho}{1-\lambda}(\frac{d_{LASAT}}{Ls} - \frac{1+(\rho-1)\lambda}{\rho}) & \frac{d_{LASAT}}{Ls} > \frac{1+(\rho-1)\lambda}{\rho} \end{cases} \tag{3.10}$$

where d_{LASAT} is the deflection of the LASAT and the length $Ls\frac{1+(\rho-1)\lambda}{\rho}$ is the total deflection of the tendon at the instance that spring 2 reaches the shut length. Figure

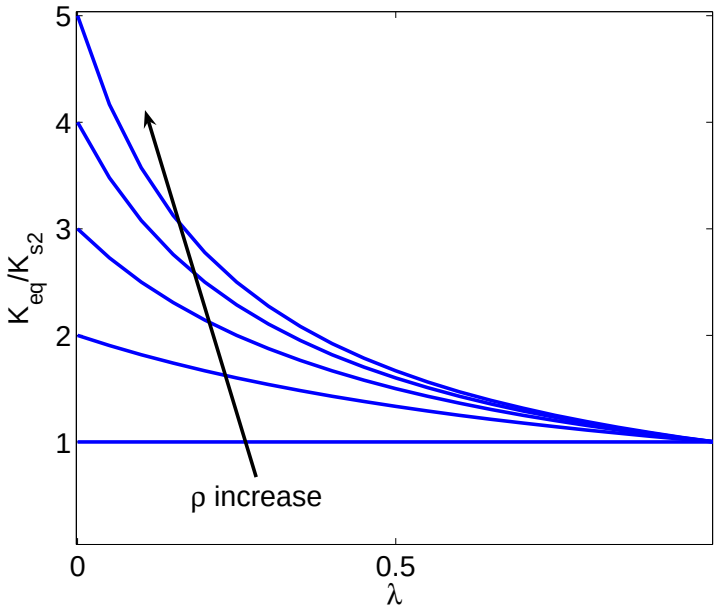

Figure 3.7: Dimensionless relation of stiffness–λ in LASAT before shut length. Each curve corresponds to a constant ρ and ρ increases from 1 to 5 with steps of 1.

3.7 illustrates the relationship of the dimensionless resultant stiffness of the LASAT, $\frac{K_{eq}}{K_{s2}}$, to λ (the ratio of the number of active coils of spring 2 to N_s) for different values of ρ (the ratio of the coil stiffness of spring 1 to spring 2). In Figure 3.7, each curve corresponds to a constant ρ and the value of ρ increases from 1 to 5 with increments of one. As shown, by increasing the λ from zero to one for a constant ρ, the stiffness of LASAT, K_{eq}, decreases.

Figure 3.8 shows the relation of dimensionless force index $\frac{F_{LASAT}}{K_{s2}Ls}$, to the dimensionless deflection index $\frac{d_{LASAT}}{Ls}$, when $\rho = 5$ for λ varying from 0.1 to 0.9 with equal steps of 0.1. As shown in Figure 3.8, there is a discontinuity in the slope of each curve as $\frac{F_{LASAT}}{K_{s2}Ls} = 1$ that is caused by the shut length of spring 2. The slope of the curves before the shut length shown in Eqn.(3.8) equals $\frac{\rho}{1+(\rho-1)\lambda}$. The slope after shut length equals $\frac{\rho}{1-\lambda}$. By increasing λ, the slope of each curve decreases before the shut length, which results in the softer equivalent spring, and increases after the shut length, which results in stiffer equivalent spring. In general, helical springs do not act linearly close

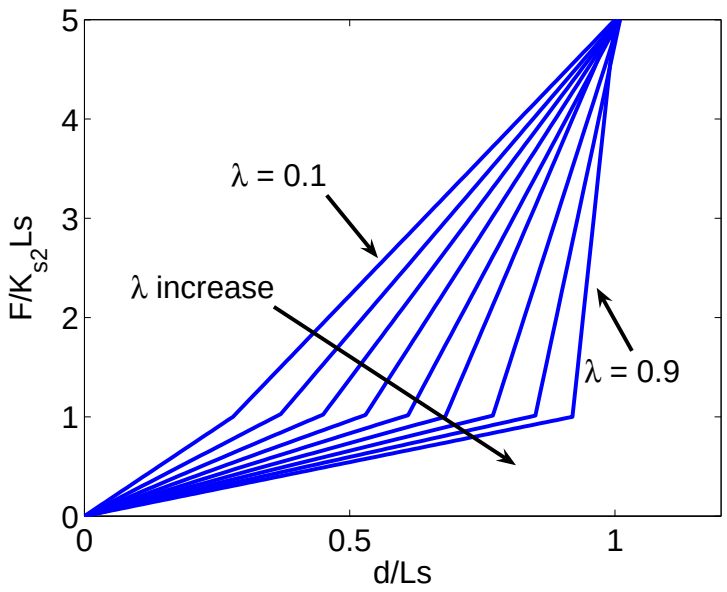

Figure 3.8: Dimensionless graph of force–deformation in LASAT. Sudden changes in slopes of the curves are caused by spring 2 reaching the shut length.

to their shut lengths. LASAT is designed in such a way as to prevent the shut length which in turn removes the nonlinear effects on the tendon caused by coil contact and friction.

From the mechanical design point of view, LASAT is comprised of an input rod, an output rod, two springs and a spring positioning mechanism as shown in Figure 3.9. The springs can slide inside the output rod and have the same coil pitch and the mean diameter, but have different wire diameters. The inner diameter of the output rod is assumed to be lower in the area contacting the softer spring than in the area contacting the stiffer spring. The output force is directly applied to the low stiffness spring and a notch inside the output rod makes a stopper that prevents the softer spring from reaching the shut length. The positioning mechanism of the coupler consists of a brushless DC motor, a spline shaft, and a coupling element. The outer surface of the coupler is threaded and the lead of each thread equals the spring's coil pitch. The inner surface of the coupler can freely slide over the sliding shaft. The coupling element can be rotated by the sliding shaft which is connected to the brush-less DC

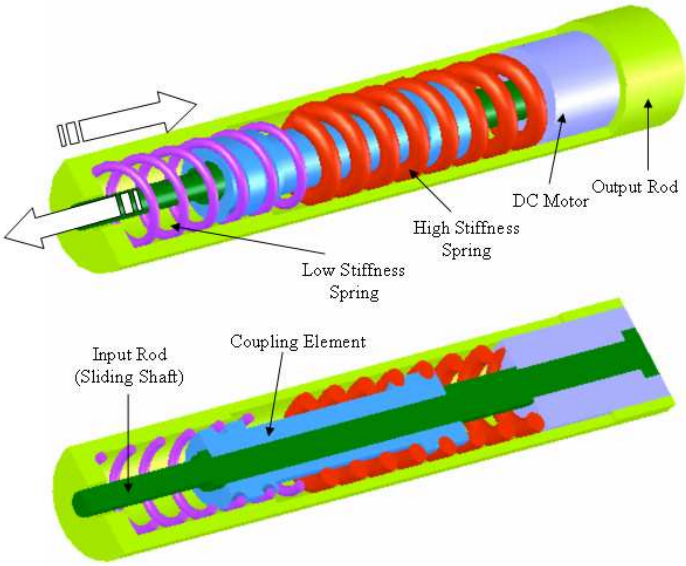

Figure 3.9: 3D model of LASAT.

motor. Then, the angular motion of the coupling element is converted to linear motion and simultaneously changes the number of acting coils in each spring. Also, an angular displacement sensor is installed on the brush-less DC motor to measure the location of the coupling element.

3.1.3 Offset Location Adjustable Stiffness Artificial Tendon

The Offset Location Adjustable Stiffness Artificial Tendon (OLASAT) is specially designed to adjust its stiffness mechanically. It switches the stiffness between two specific values. Here, the artificial tendon is a combination of two parallel springs with an offset as shown in Figure 3.10. The offset, a, between the two springs can be adjusted. The applied force, F_{OLASAT}, is a function of the stiffness of spring 1 with a low stiffness (K_{sp1}), spring 2 with a high stiffness (K_{sp2}), the offset (a), and the spring's deflection

at the end point (d_{OLASAT}) as follows:

$$F_{OLASAT} = \begin{cases} K_{sp1} d_{OLASAT} & d_{OLASAT} < a \\ \\ K_{sp1} a + (K_{sp1} + K_{sp2})(d_{OLASAT} - a) & d_{OLASAT} \geq a \end{cases} \tag{3.11}$$

The above equation in the dimensionless form appears in Eqn.(3.12) where K_{sp2} is replaced by ηK_{sp1}.

$$\frac{F_{OLASAT}}{K_{sp1} a} = \begin{cases} \frac{d_{OLASAT}}{a} & \frac{d_{OLASAT}}{a} < 1 \\ \\ 1 + (1 + \eta)(\frac{d_{OLASAT}}{a} - 1) & \frac{d_{OLASAT}}{a} \geq 1 \end{cases} \tag{3.12}$$

The force-deflection graph of the OLASAT is illustrated in Figure 3.11. η is the ratio of the stiffness of spring 2 to that of spring 1 ($\eta = 5$ in Figure 3.11). The slopes of the straight lines in Figure 3.11 represent the stiffness of OLASAT. The stiffness is suddenly switched from the stiffness of spring 1, K_{sp1}, to the stiffness of two parallel springs, $(\eta + 1)K_{sp1}$, at point $d_{OLASAT} = a$.

From the mechanical design point of view, OLASAT is a uni-directional tendon and consists of an input rod, an output rod, a low stiffness spring and a high stiffness spring, with a positioning mechanism using a ball screw and a nut (as shown in Figure 3.12). The low stiffness spring is coupled between the input and the output rod. The high stiffness spring is connected to the input rod on one side and is free on the other side. A miniature brushless DC motor connected to the ball screw provides the sliding motion of the high stiffness spring over the slot deployed on the input rod, which can adjust the offset between the two springs.

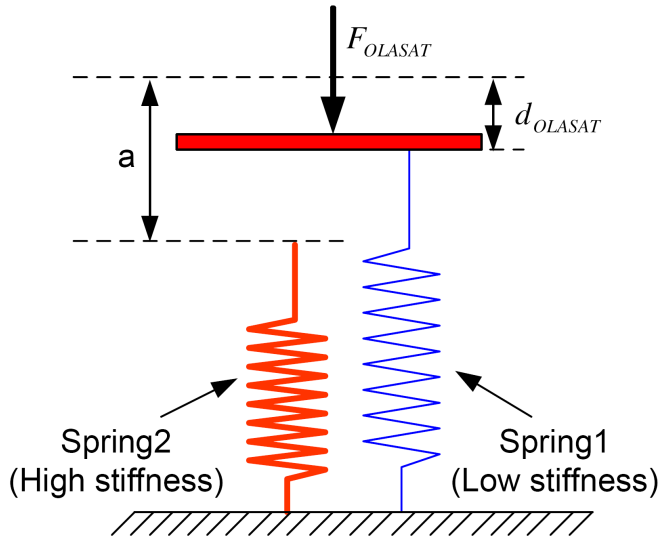

Figure 3.10: Schematic diagram of OLASAT.

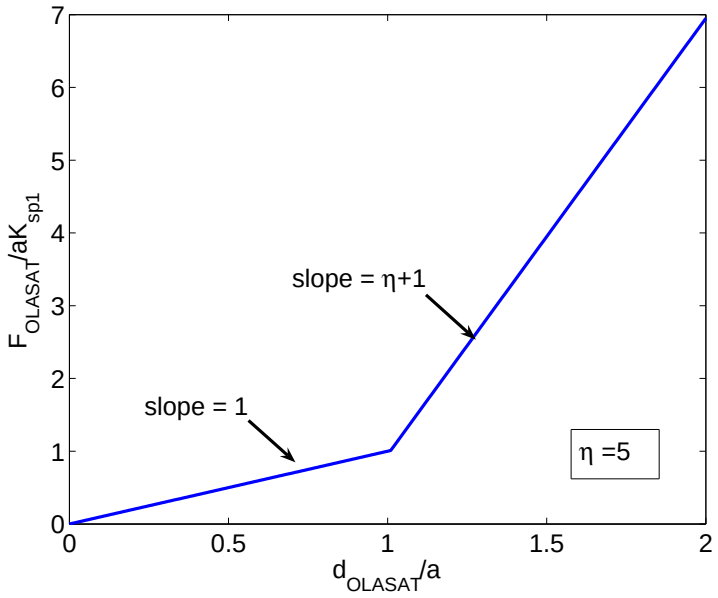

Figure 3.11: Dimensionless force–deformation graph of OLASAT.

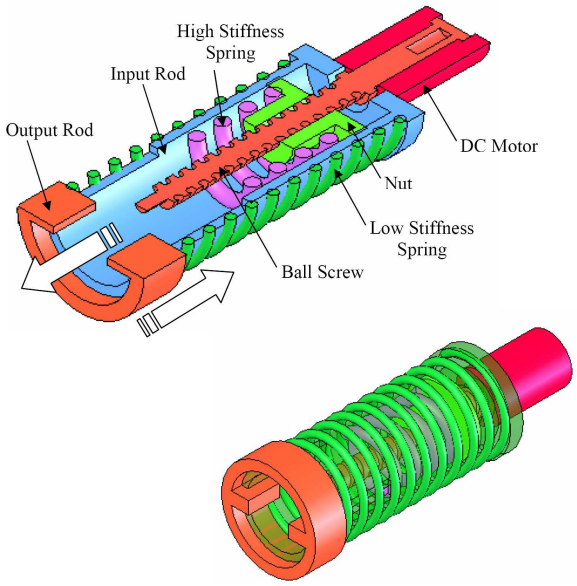

Figure 3.12: 3D model of OLASAT.

3.2 Advantages and limitations

In this section, the advantages and limitations of each conceptual design based on simulations are discussed. The main advantage of RASAT is the adjustment of the stiffness over a wide range, by means of a moderate change in the distance of the springs to the center of rotation. As shown in Figure 3.3, by adjusting $\frac{d}{d_{max}}$ from a low value, 0.1, to a high value, 1, slopes of the curves and consequently, the stiffness of RASAT increase in a wide range of numbers. For example, by considering the $d_{max} = 50mm$ and changing d from $d = 5mm$ to $d = 50mm$, the stiffness increases 100 times. This capability can significantly improve the performance of bipedal walking. For example, RASAT can be used at the knee joint of the bipedal walking robot when a low stiffness (during the passive motion of the swing phase) and a high stiffness (during the stance phase) are required. Friction of the joints and the high number of moving elements are among RASAT's disadvantages.

LASAT can be built lighter and more compact than RASAT. In addition to this ad-

vantage, the stiffness of the equivalent spring in LASAT is linear. The friction between the coupler and the springs during the adjustment of the number of active coils may cause difficulties as the stiffness changes. Stiffness of LASAT after the shut length changes a lot for high values of λ (the ratio of the number of active coils of spring 2 to N_s). This counts as the major disadvantage of LASAT.

The design of OLASAT is simple and can be built more easily than the other mechanisms. In addition, the friction is lower between the moving parts with respect to RASAT and LASAT. In OLASAT, the positioning mechanism (including DC motor and ball screw as shown in Figure 3.12) adjusts the location of spring 2 and controls the output force of the DC motor to the load. These advantages can potentially increase the performance of the robots and are very important in the development of efficient bipedal walking robots. OLASAT can only have two stiffness values. In bipedal walking, the stiffness of ASATs can be adjusted during the swing phase while the end effector is not in contact with the environment. This allows a small required force to adjust the stiffness which leads to the smaller size of ASATs and lower energy consumption for stiffness adjustment.

3.3 Case study

In this section, the effects of each conceptual design of the ASAT on the energy economy of bipedal walking during the collision phase are studied. This study can answer the question of applicability of the idea in bipedal walking robots. To reach this objective and to reduce the complexity of the analysis, a simplified model of a bipedal walking robot is introduced which consists of the dynamic model of each design of ASAT at the ankle joint. In general, the stance period of the walking cycle is demarcated into four phases which are explained by Kuo et al [39]. Collision of the foot with the ground is the major reason of energy loss during passive bipedal walking. Thus, the dynamic model of the bipedal walking robot during collision is detailed in this section. The

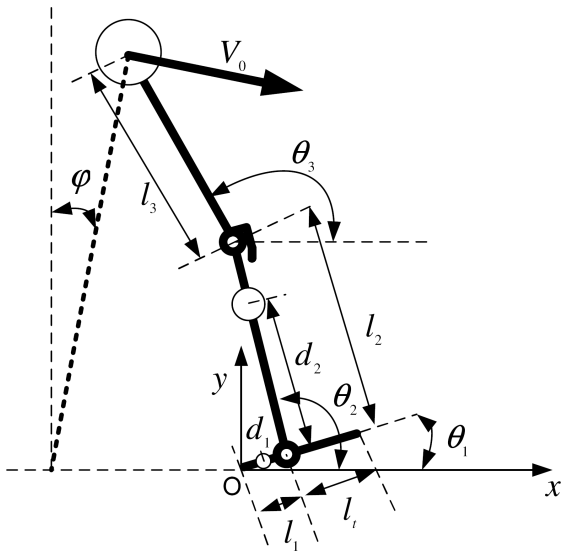

Figure 3.13: Diagram of the robot.

simulation results of the bipedal walking model in the collision phase are explained. The model of the designed ASAT (RASAT, LASAT, OLASAT) in two cases of poorly-adjusted and well-adjusted stiffness, which are explained in detail in the next section, is included in the simulation results to compare the energy economy of the biped in two extreme cases.

3.3.1 Dynamic modeling of the collision phase

In this section, the focus is on dynamic modeling of the bipedal walking robot during the collision phase. Here, a simplified model of a walking robot is introduced, which is able to test the effectiveness of ASAT in reducing energy loss. The robot includes, as shown in Figure 3.13, a foot (link 1), a shank (link 2), and a thigh (link 3). To simplify the analysis, the bipedal walking model is in sagittal plane with friction free joints. In addition, a point mass at center of gravity of each link has been assumed. The mass of the upper body and trailing leg is also assumed to be at the upright end of the thigh. In Fig 3.13, the value of d_i represents the location of the center of mass of link i, which is measured as a distance between the mass center of link i and joint i. Joints

i ($i = 1, 2, 3$) are the heel, the ankle, and the knee, respectively. θ_i is also denoted as the angle of the link i with respect to the horizontal axis. x_h and y_h represent the horizontal and vertical distance between the heel and a reference point O on the ground. Dynamic modeling of the bipedal walking in the collision phase is presented here using the Lagrangian approach. The collision phase starts with an impact of heel-strike followed by a continuous motion. At the end of the collision phase, a second impact of the foot-touch-down occurs. Both impacts are assumed to be rigid to rigid, instantaneous, and perfectly plastic, which dissipates part of the energy of the robot. Generalized coordinates of the robot include the horizontal and vertical positions of the heel as well as the foot, shank and thigh angles with respect to the horizontal line that correspond to x_h, y_h, θ_1, θ_2, and θ_3, respectively.

Dynamic modeling of the heel-strike

At the beginning of the stance phase, the heel contacts the ground with impact. The impact is assumed as an impulsive constraint of a sudden change in the velocity of the heel to zero. The joints (the heel, the ankle, and the knee) angular velocities are also subjected to a sudden change resulting from this impact event. At the heel-strike, there is an impulsive force between the heel and the ground. The external moment at each joint is taken to be negligible during impact. For purpose of simplicity, impulsive constraint relations [110] are employed in this work to provide the angular velocities of the foot, the shank and the thigh after the heel-strike. Since no detailed information is available from the literature, the derivations and complete forms of the constrained impulsive motion equations are presented here.

By applying the impulsive constraint relations [110], the Lagrange multiplier form of the constrained impulsive motion equation at the heel-strike is shown below.

$$\sum_{j=1}^{5} D_{ij}(\dot{q}_j^+ - \dot{q}_j^-) = \hat{Q}_i + \sum_{k=1}^{n} \hat{\lambda}_k a_{ki} \qquad (i = 1, 2, ..., 5) \tag{3.13}$$

where

$$\dot{\mathbf{q}} = (\dot{x}_h, \dot{y}_h, \dot{\theta}_1, \dot{\theta}_2, \dot{\theta}_3) \tag{3.14}$$

$$D_{ij} = \frac{\partial^2 K}{\partial \dot{q}_i \partial \dot{q}_j} \qquad (i, j = 1, 2, ..., 5) \tag{3.15}$$

$\mathbf{q}$ is a 5×1 generalized coordinate vector and K is the kinetic energy of the biped (shown in Section 3.3.1). $\dot{x}_h$ and $\dot{y}_h$ are the horizontal and vertical velocities of the heel. $\dot{\theta}_1$ and $\dot{\theta}_2$ and $\dot{\theta}_3$ are the angular velocities of the foot, the shank, and the thigh. The superscripts $'+'$ and $'-'$ represent the time immediately after and before the impact. n is the maximum number of impulsive constraints which equals 2. D_{ij} are elements of a 5×5 inertia matrix which are calculated from the kinetic energy of the biped.
In this thesis, it is also assumed that the heel-strike is not accompanied by an external impulse, $\hat{Q}_i$. Thus

$$\hat{Q}_i = 0 \qquad (i = 1, 2, ..., 5) \tag{3.16}$$

The term $\sum_{k=1}^{n} \hat{\lambda}_k a_{ki}$ in Eqn.(3.13) corresponds to constraint impulse and $\hat{\lambda}_k$ is an impulsive Lagrangian multiplier.
The heel-strike consists of the constraints $\Delta\dot{x}_h = {}^{HS}\dot{x}_h^+ - {}^{HS}\dot{x}_h^- = -{}^{HS}\dot{x}_h^-$ and $\Delta\dot{y}_h = {}^{HS}\dot{y}_h^+ - {}^{HS}\dot{y}_h^- = -{}^{HS}\dot{y}_h^-$ that correspond to the zero velocity of the heel immediately after the heel-strike. The superscript HS corresponds to the instant of the heel-strike. The generalized coordinate vector $\mathbf{q}$ is divided into two vectors of $\mathbf{q}_1 = (x_h, y_h)$ and $\mathbf{q}_2 = (\theta_1, \theta_2, \theta_3)$. In addition, it is assumed that the initial conditions of the robot before the heel-strike ($\dot{\mathbf{q}}_1^-$ and $\dot{\mathbf{q}}_2^-$) are given. Thus, to solve the angular

velocity of each joint, Eqn.(3.13) is shown in the following matrix format:

$$\begin{bmatrix} D1 & D2 \\ D3 & D4 \end{bmatrix} \begin{bmatrix} \Delta\dot{\mathbf{q}}_1 \\ \Delta\dot{\mathbf{q}}_2 \end{bmatrix} = \begin{bmatrix} {}^{HS}\hat{\lambda} \\ 0 \end{bmatrix} \tag{3.17}$$

where sub-matrices of the inertia are divided into $D1$, $D2$, $D3$ and $D4$, which are 2×2, 2×3, 3×2 and 3×3 matrices. The impulsive Lagrangian multiplier, ${}^{HS}\hat{\lambda}$, at the heel-strike is a 2×1 vector. Therefore, by solving Eqn.(3.17), the angular velocities of the links after the heel-strike are obtained:

$$\dot{\mathbf{q}}_2^+ = \dot{\mathbf{q}}_2^- - D4^{-1}D3(\Delta\dot{\mathbf{q}}_1) \tag{3.18}$$

The impulse caused by the impact event at the heel-strike can also be calculated:

$${}^{HS}\hat{\lambda} = D1(\Delta\dot{\mathbf{q}}_1) + D2(\Delta\dot{\mathbf{q}}_2) \tag{3.19}$$

After the heel-strike, the number of the degrees of freedom of the biped is reduced. The generalized coordinates vector of the robot reduces to $\mathbf{q} = (\theta_1, \theta_2, \theta_3)$ and also the inertia is reduced to a 3×3 matrix. The equations of continuous motion of the robot are given in the next section.

Dynamic modeling of the continuous motion

According to Figure 3.13, the coordinates of the mass center of link i are:

$$x_{ci} = x_h + d_i\cos(\theta_i) + \textstyle\sum_{j=1}^{i-1} l_j\cos(\theta_j) \tag{3.20}$$

$$y_{ci} = y_h + d_i\sin(\theta_i) + \textstyle\sum_{j=1}^{i-1} l_j\sin(\theta_j) \tag{3.21}$$

The potential energy (assume $P = 0$ at the ground level) of the two-link biped is:

$$P = \sum_{i=1}^{3} m_i g y_{ci} \tag{3.22}$$

The elastic torque of the artificial tendons is considered as a force vector in dynamic equations and is not included in potential energy. The kinetic energy is

$$K = \sum_{i=1}^{3} \frac{1}{2} m_i (\dot{x}_{ci}^2 + \dot{y}_{ci}^2) \tag{3.23}$$

By applying the potential and kinetic energy of equations (3.22) and (3.23) to the Lagrangian equations, the dynamic equation of the robot during continuous motion is given below:

$$M(\theta)\ddot{\theta} + H(\theta, \dot{\theta})\dot{\theta} + G(\theta) + S(\theta) = I(\theta) \tag{3.24}$$

where $M(\theta)$ is a 3×3 positive definite and symmetric inertia matrix. $H(\theta, \dot{\theta})$ is a 3×3 matrix related to centrifugal and coriolis terms. $G(\theta)$ is a 3×1 matrix of torque related to the gravity of each link. $S(\theta)$ is a 3×1 matrix related to the elastic torques of the artificial tendon at the ankle joint and the linear spring at the knee joint. θ, $\dot{\theta}$, $\ddot{\theta}$, and $I(\theta)$ are the generalized coordinates, velocities, accelerations, and the external torque vector respectively [111, 112]. The detailed forms of M, H, G and S in Eqn.(3.24) are presented as:

$$M_{ij} = U_{ij} \cos(\theta_i - \theta_j) \tag{3.25}$$

$$H_{ij} = U_{ij} \sin(\theta_j - \theta_i)\dot{\theta}_j \tag{3.26}$$

$$G_i = +g_i \cos(\theta_i) \tag{3.27}$$

U_{ij} and g_i are inertial and gravitational terms defined as:

$$U_{ij} = \begin{cases} m_i d_i^2 + (\sum_{j=i+1}^{3} m_j) l_i^2 & \text{j} = i \\ m_j d_j l_i + (\sum_{k=j+1}^{3} m_k) l_i l_j & \text{j} > i \\ U_{ji} & \text{j} < i \end{cases} \tag{3.28}$$

$$g_i = m_i d_i g + (\sum_{j=i+1}^{3} m_j) l_i g \tag{3.29}$$

$$S = \begin{bmatrix} T_{ankle} \\ -T_{ankle} + K_{knee}(\theta_3 - \theta_2 - \varphi_3) \\ -K_{knee}(\theta_3 - \theta_2 - \varphi_3) \end{bmatrix} \tag{3.30}$$

where one end of ASAT at joint i is connected to the link $i-1$ with an initial angle of φ_i. The elastic torque at the ankle joint, T_{ankle}, is dependent on the type of ASAT attached to the ankle joint as well as to the initial angle of ASAT. $T_{ankle} = T$ for RASAT, and T is calculated from Eqn.(3.1). Linear motions of LASAT and OLASAT are converted to the angular motion at the ankle joint using an angular pulley with a radius of R. Thus, $T_{ankle} = RF_{LASAT}$ for LASAT where F_{LASAT} is calculated from Eqn.(3.9). $T_{ankle} = RF_{OLASAT}$ for OLASAT where F_{OLASAT} is calculated from Eqn.(3.11).

Dynamic modeling of the foot-touch-down

The foot-touch-down (FTD) is the ending instant of the collision phase which is accompanied by a sudden change in the angular velocity of the foot to zero caused by impact. It also causes a sudden change in angular velocity of the shank and the thigh which

are calculated in this section. In this work, the foot-touch-down impact is modeled by the constraint equation shown below.

$$\begin{aligned} \Delta^{FTD}\dot{\theta}_1 &= {}^{FTD}\dot{\theta}_1^+ - {}^{FTD}\dot{\theta}_1^- \\ &= -{}^{FTD}\dot{\theta}_1^- \end{aligned} \tag{3.31}$$

${}^{FTD}\dot{\theta}_1^-$ and ${}^{FTD}\dot{\theta}_1^+$ are the angular velocity of the foot immediately before and after the foot-touch-down. The above equation shows that the angular velocity of the foot suddenly changes to zero. Jumps in the angular velocity of the shank and the thigh are provided by a reduced form of Eqn. (3.17) where $\mathbf{q} = (\theta_1, \theta_2, \theta_3)$. The matrix D4 in Eqn. (3.17) is divided into four sub-matrices of inertia of D_1, D_2, D_3, and D_4 which are 1×1, 1×1, 2×1 and 2×2 matrices respectively. Here, the generalized coordinates vector of the foot-touch-down, $\mathbf{q}$, is divided into $\mathbf{q}_1 = (\theta_1)$ and $\mathbf{q}_2 = (\theta_2, \theta_3)$. Therefore, the angular velocity of the links after the foot-touch-down is defined:

$$\dot{\mathbf{q}}_2^+ = \dot{\mathbf{q}}_2^- - D_4^{-1} D_3 (\Delta\dot{\mathbf{q}}_1) \tag{3.32}$$

The impulse caused by the impact event at the foot-touch-down can also be calculated:

$${}^{FTD}\hat{\lambda} = D_1(\Delta\dot{\mathbf{q}}_1) + D_2(\Delta\dot{\mathbf{q}}_2) \tag{3.33}$$

The foot is assumed to be stationary on the ground after the foot-touch-down, thus the degrees of freedom of the system will be reduced and the generalized coordinate vector of the robot will be changed to $\mathbf{q} = (\theta_2, \theta_3)$.

3.3.2 Simulations and results

In this section, the effects of each conceptual design of ASAT on reducing the energy loss of bipedal walking during the collision phase are studied through computer sim-

Table 3.1: Physical parameters of the robot.

Link no.	$m_i[kg]$	$l_i[m]$	$d_i[m]$
1	1	0.05	0.03
2	4.5	0.431	0.247
3	61.1	0.68	0.68

ulations. Reducing the energy loss in the collision phase can significantly affect the energy performance of the bipedal walking robots. Thus, the simulations are performed in the collision phase for 6 case studies using RASAT, LASAT, and OLASAT at the ankle joint, with both poorly and well-adjusted stiffnesses. Poorly-adjusted stiffnesses represent the lowest value of the stiffness of each ASATs. Well-adjusted stiffnesses are defined using a trial and error procedure which minimizes the energy loss during the collision phase. Adjusting the stiffness of ASAT requires energy and causes a change in the position of the center of mass of the biped. However those parameters are not assumed in this study because of their negligible effects. The parameters of the robot representing a simplified model of a human sized bipedal robot, as explained in Tzafestas et. al [113], are listed in Table 3.1.

The generalized coordinates and parameters of the robot are visually illustrated in Figure 3.13. The initial states immediately before the heel-strike are specified: $\theta_1 = 15^o$, $\theta_2 = 105^o$, $\theta_3 = 105^o$, $x_h = y_h = 0$, and $\dot{\theta}_1 = \dot{\theta}_2 = \dot{\theta}_3 = 0$. These initial conditions simulate the perpendicular foot to the thigh, while the leg is assumed to be straight with an initial angle of 105^o with respect to the horizontal line, and with zero angular velocity before the heel-strike. The same initial translational velocity is assumed for the robot immediately before the heel-strike. $\dot{x}_{ci} = V_0 sin\varphi$ and $\dot{y}_{ci} = V_0 cos\varphi$. In this analysis, $V_0 = 1.5m/s$ and $\varphi = 15^o$ which is within the walking speed range of the biped. The same initial conditions are chosen for all case studies, and the focus of the simulations is on demonstrating the effects of adjusting the artificial tendons on the energetics of the robot during the collision phase.

The stiffness of the knee joint, $K_{knee} = 1000[\frac{Nm}{rad}]$, is assumed constant. By inserting different ASATs at the ankle joint of the robot, the dynamics of the robot are studied in six different cases. Each tendon involves two cases of poorly-adjusted and well-adjusted stiffness. Cases 1–2 consist of RASAT at the ankle joint while: $K_1 d_{max}^2 = 500, \frac{l}{d_{max}} = 0.1$, and $\mu = 5$. The value of $\frac{d}{d_{max}}$ equals 0.1 and 1 for case 1 and 2, which represent poorly and well-adjusted stiffness respectively. Cases 3–4 consist of LASAT at the ankle joint while: $R^2 K_{s2} = 300[\frac{Nm}{rad}], \frac{Ls}{R} = 0.2618[rad]$ and $\rho = 3$. λ equals to 1 and 0.1 for Cases 3 and 4, which represent poorly and well-adjusted stiffness, respectively. Cases 5 and 6 consist of OLASAT at the ankle joint while $R^2 K_{sp2} = 300\ [\frac{Nm}{rad}]$, and $\eta = 4$. The offset $\frac{a}{R}$ equals to 0.2618 $[rad]$ and 0.0349 $[rad]$ for Cases 5 and 6, which represent poorly and well-adjusted stiffness respectively.

Since the focus of this study is on the effects of ASATs on energy economy of the biped during the collision phase, the initial states of the simulation immediately before the heel-strike are the same for all the cases. Here the results of the simulations after the heel-strike are presented in Figures 3.14-3.19. Joint angles are shown in Figures 3.14-3.19a where θ_1, θ_2, and θ_3 are the angle of the foot, ankle, and knee with respect to the ground. The absolute value of velocity of the center of mass (COM) of the body in the robot is illustrated in Figures 3.14-3.19b. The discontinuity in velocity caused by the foot-touch-down (FTD), is indicated by an ellipse in Figures 3.14-3.19b. The trajectory and velocity vector of the COM of the body during the collision phase are demonstrated in Figures 3.14-3.19c. In addition, the kinetic energy of the robot in the same time period as the simulations is depicted in Figures 3.14-3.19d, including the discontinuity that is illustrated with an ellipse. Finally, the stick diagram of the robot during the collision period is shown in Figures 3.14-3.19(e), with the time step of 0.005 sec after the heel-strike. The results of the simulations for each conceptual designs of ASATs are separately discussed below.

Figures 3.14a and 3.15a indicate that the collision phase takes 0.017 sec and 0.036 sec

for cases 1 and 2 respectively. It shows that the collision period is increased while RASAT is well-adjusted, which in turn causes to reduce the impulsive force applied on the robot by decreasing the angular velocity of the foot. Significant reduction in the kinetic energy of the robot caused by the FTD is shown by ellipses in Figures 3.14d and 3.15d. By increasing the ratio $\frac{d}{d_{max}}$ from 0.1 in the first case to 1 in the second case, the discontinuities in the velocity and the kinetic energy of the robot during the FTD are significantly reduced, as shown in Figures 3.15b and 3.15d, compared to those shown in Figures 3.14b and 3.14d. Figure 3.15c shows that the vertical component of the velocity of the COM of the body is gradually decreased during the collision phase. In cases 3 and 4, adjusting λ from 1 to 0.1 (Figure 3.16 and 3.17) increases the stiffness of LASAT at the ankle joint. Figures 3.16a and 3.17a indicate that the collision phase period takes 0.019 sec and 0.025 sec for cases 3 and 4 respectively. Figure 3.17c shows that the vertical component of the velocity of the COM of the body is gradually decreased during the collision phase, which is desirable in decreasing the impact at the FTD. Adjusting the stiffness using LASAT decreases discontinuities in velocity and kinetic energy (compare the results shown in Figures 3.16b and 3.16d with the results shown in Figures 3.17b and 3.17d). The results show that the kinetic energy loss in each step of walking can be significantly reduced through proper adjustment of the LASAT.

In cases 5 and 6, the effectiveness of adjusting the offset in OLASAT from $\frac{a}{R} = 0.2618\ [rad]$ to $\frac{a}{R} = 0.0349\ [rad]$ are shown in Figures 3.18 and 3.19. Figures 3.18a and 3.19a indicate that the collision phase period takes 0.019 sec and 0.041 sec for cases 5 and 6 respectively. Figure 3.19c shows that the vertical component of the velocity of the COM of the body is gradually decreased during the collision phase, which is also very useful in decreasing the impact on FTD. Adjusting the stiffness using OLASAT can decrease discontinuities in the velocity and the kinetic energy (compare the results shown in Figures 3.18b and 3.18d with Figures 3.19b and 3.19d). The results show

that the kinetic energy loss in each walking step can be significantly reduced through proper adjustment of the LASAT.

In all of the above cases, the period of the collision phase (starting from the heel-strike and ending at the FTD) has been increased by properly adjusting the stiffness of the tendons. This result is based on a comparison of the foot trajectory from an initial value of 15^o to 0^o in each case study at part a of Figures 3.14-3.19. Through proper adjustment of the stiffness, the vertical velocity of COM of the body during collision is gradually decreased to zero. This effect can potentially increase the efficiency of locomotion by decreasing the energy loss at the FTD as well as by storing and returning the energy at the ankle joint during the stance phase. In addition, for the physical parameters of the robot listed in Table 3.1, $R = 50mm$ and $d_{max} = 65mm$ can be chosen. Using Eqn.(3.5), for a cold-drawn spring wire with coil diameter of $dia = 2.5mm$ including 6 coils, the output diameters of the low and high stiffness springs are below $25mm$ for all design concepts. These illustrate the compatibility of the size of ASATs to the size of the biped.

The kinetic energy loss of case 1 is 20% of the total kinetic energy of the robot before the FTD and it is reduced to 5% in case 2 by propper stiffness adjustment of the RASAT. Comparing case 3 with a 19% kinetic energy loss and case 4 with a 3.5% kinetic energy loss also demonstrates the significant effects of the LASAT in reducing the energy loss. The simulation results of case 5 with a 20% kinetic energy loss and case 6 with a 1% kinetic energy loss also illustrate the significant improvement in the energetics of the bipedal walking robots by proper stiffness adjustment of OLASAT.

3.4 Summary

Adjusting the leg stiffness is highly desired in legged robotic applications. As a result, three different conceptual designs of the adjustable stiffness artificial tendon (ASAT) were developed in this chapter. The mathematical model and the 3D detailed design

of each conceptual design of ASAT were illustrated. A simplified model of bipedal walking robot including a foot, a shank, and a thigh was introduced in this chapter incorporating the dynamics model of the ASATs at the ankle joint. The dynamic modeling of the bipedal walking robot was studied during the collision phase. The collision phase includes two discontinuities in motion, the heel-strike and the foot-touch-down, which were modeled using impulsive constraints. The results of the simulations of the biped motion illustrate the significant effects of the adjustment of the stiffness of the ASATs in improving the energy economy of the bipedal walking by reducing the energy loss. The simulation results illustrate the significant improvement in the energy economy of the bipedal walking robot by proper stiffness adjustment. The roles of stiffness adjustment in improving the energy economy of the bipedal walking during the stance phase and the consecutive walking steps are explained in the next chapter using OLASAT and a new simplified model of bipedal walking.

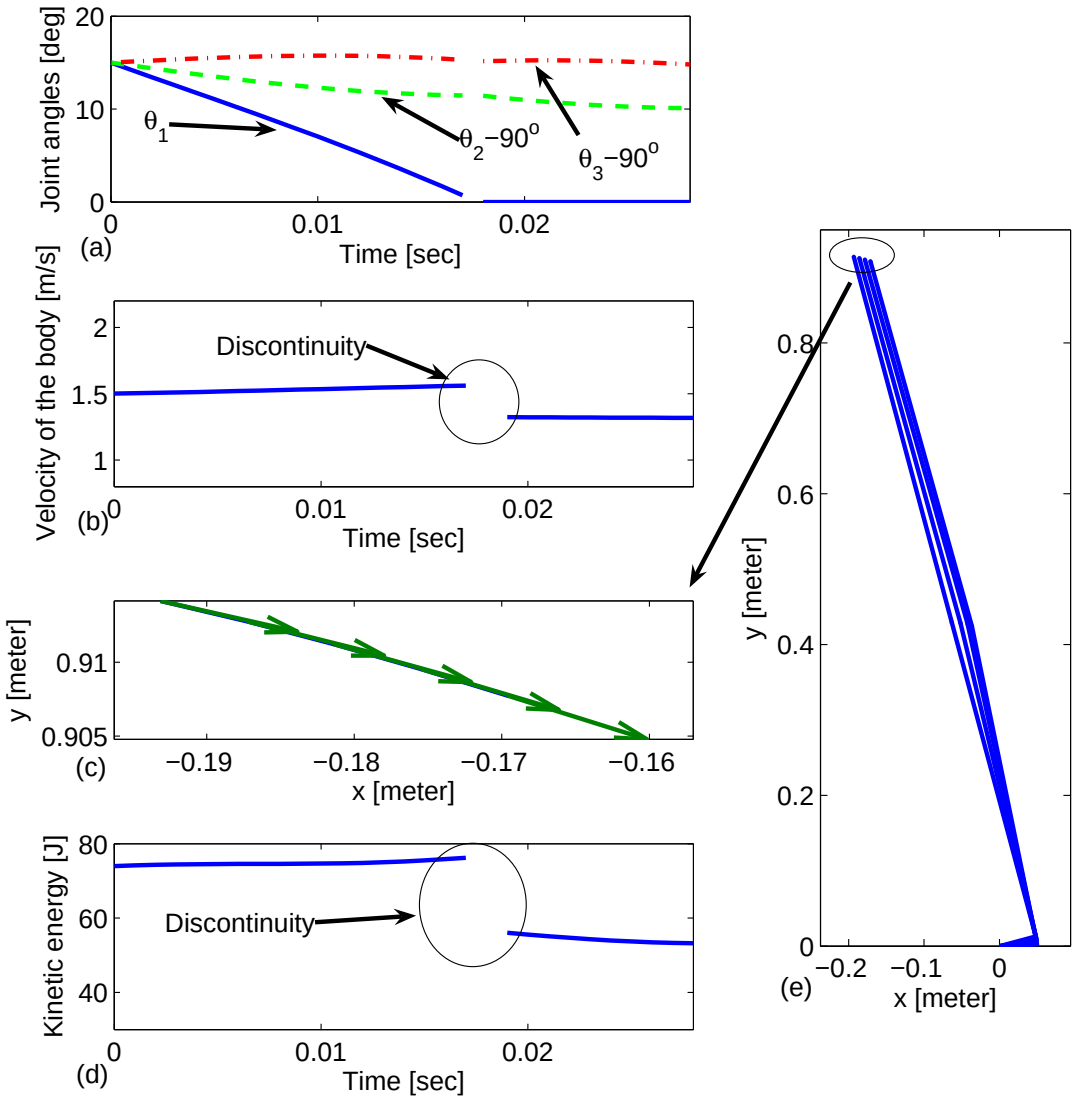

Figure 3.14: Results of the collision phase in Case 1. RASAT deployed on ankle joint. $K_{knee} = 1000Nm/rad$, $K_1 = \frac{500}{d_{max}^2}$ $[N/m]$, $\frac{l}{d_{max}} = 0.1$, $\mu = 5$ *and* $\frac{d}{d_{max}} = 0.1$

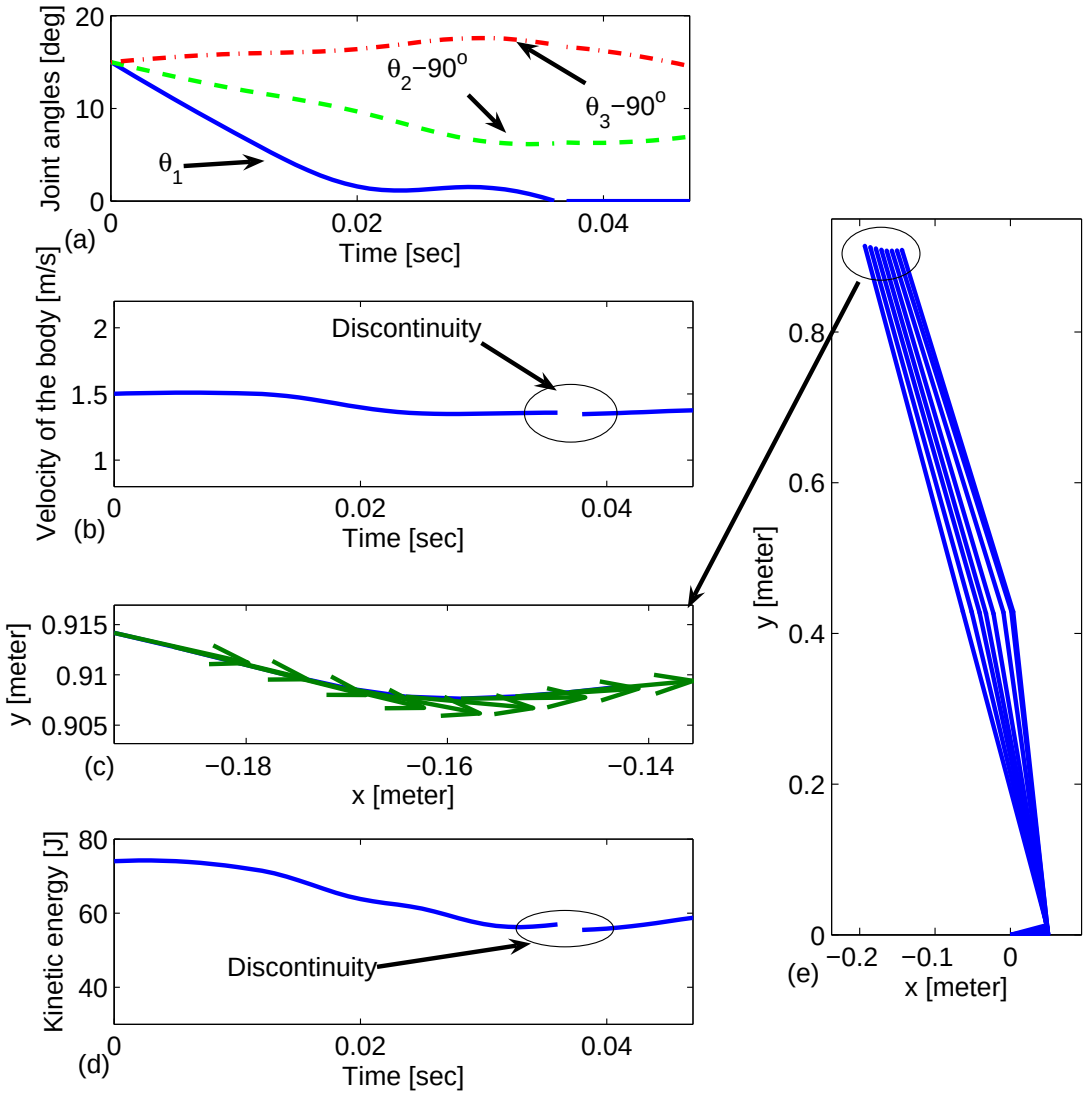

Figure 3.15: Results of the collision phase in Case 2. RASAT deployed on ankle joint. $K_{knee} = 1000Nm/rad$, $K_1 = \frac{500}{d_{max}^2}$ $[N/m]$, $\frac{l}{d_{max}} = 0.1$, $\mu = 5$ *and* $\frac{d}{d_{max}} = 1$

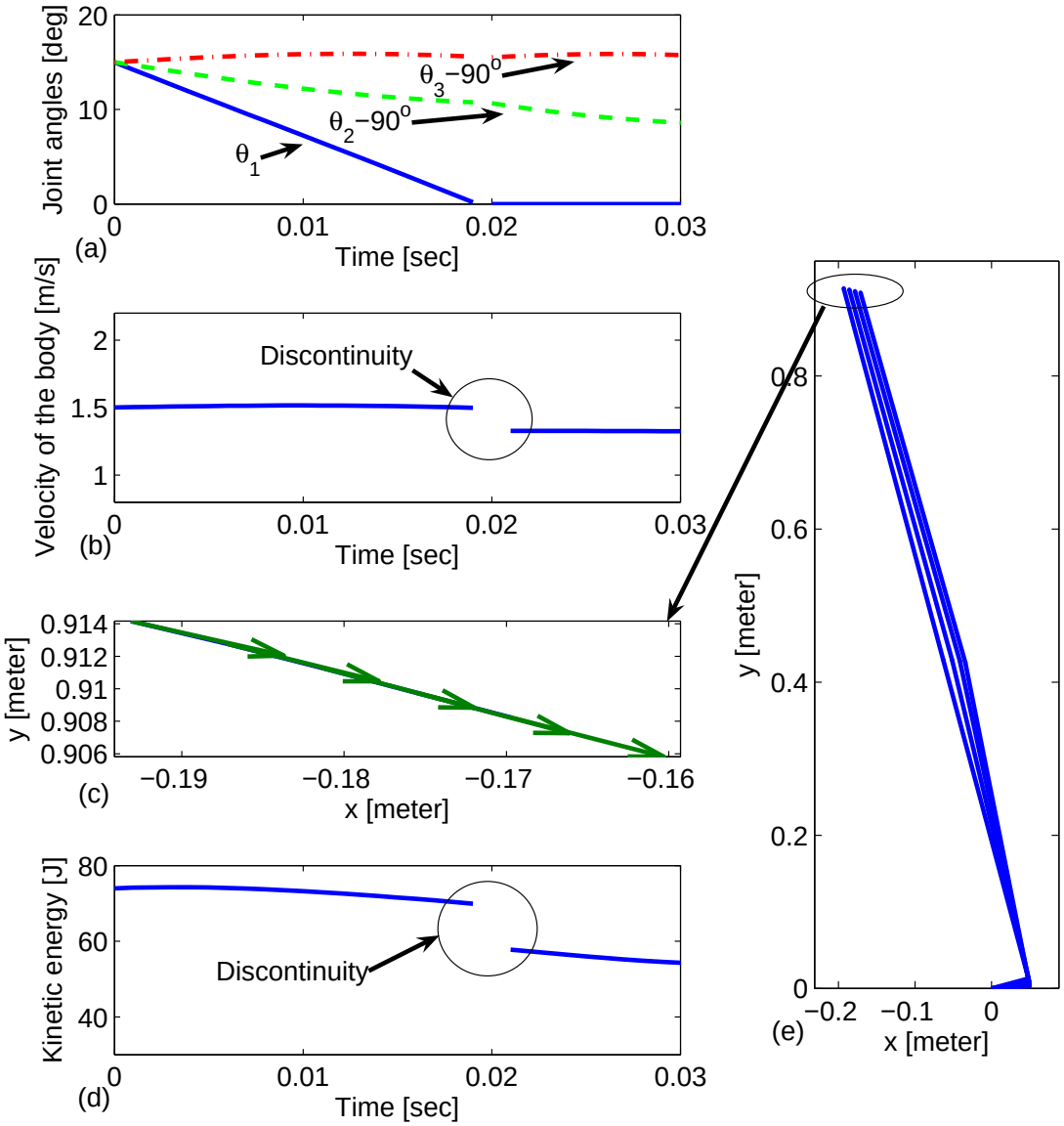

Figure 3.16: Results of the collision phase in Case 3. LASAT on ankle joint while: $K_{s2} = \frac{300}{R^2}\ [\frac{N}{m}]$, $Ls = \frac{0.2618}{R}$, $\rho = 3$ *and* $\lambda = 1$.

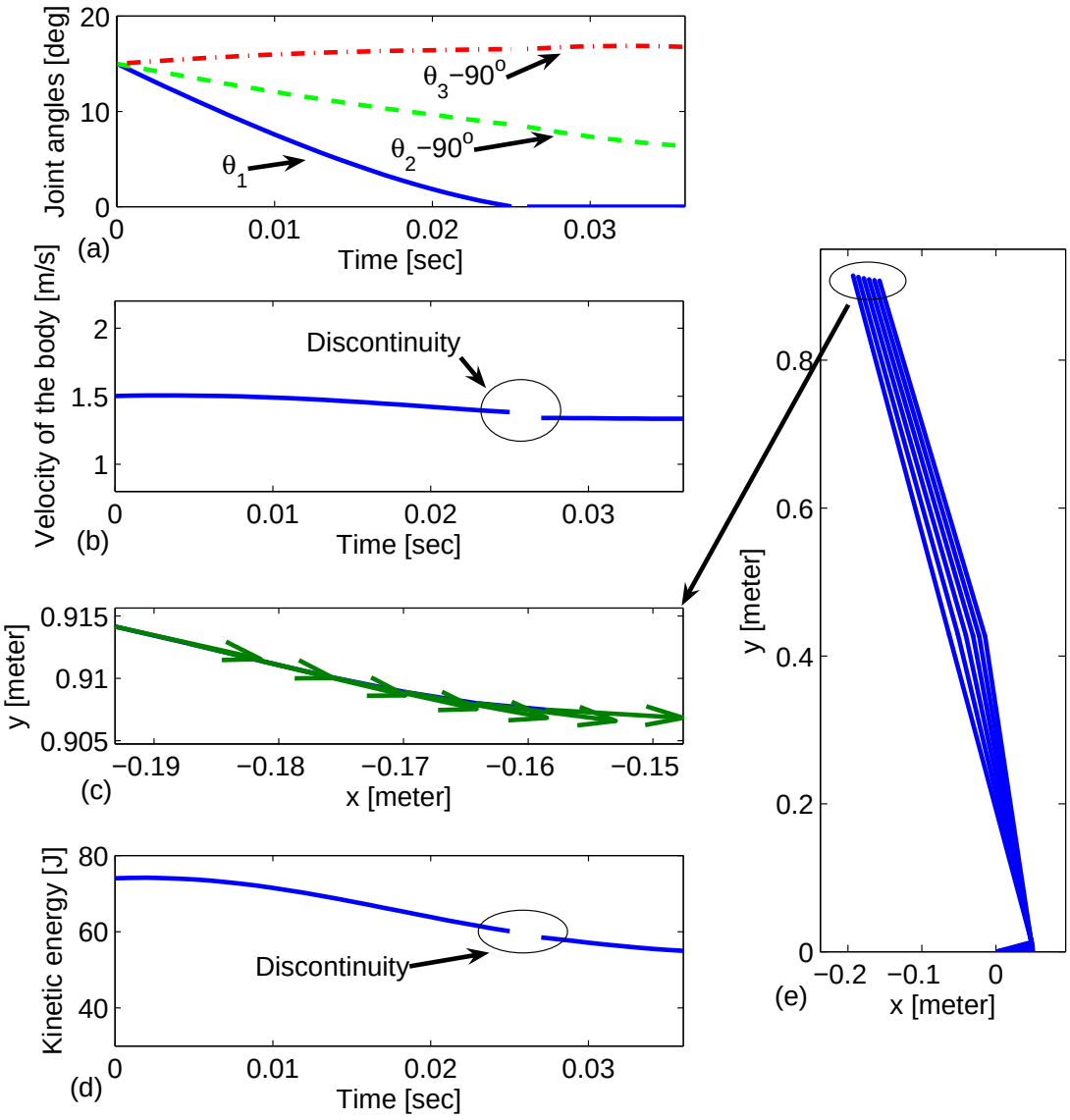

Figure 3.17: Results of the collision phase in Case 4. LASAT on ankle joint while: $K_{s2} = \frac{300}{R^2}\ [\frac{N}{m}]$,$Ls = \frac{0.2618}{R}$, $\rho = 3$ *and* $\lambda = 0.1$.

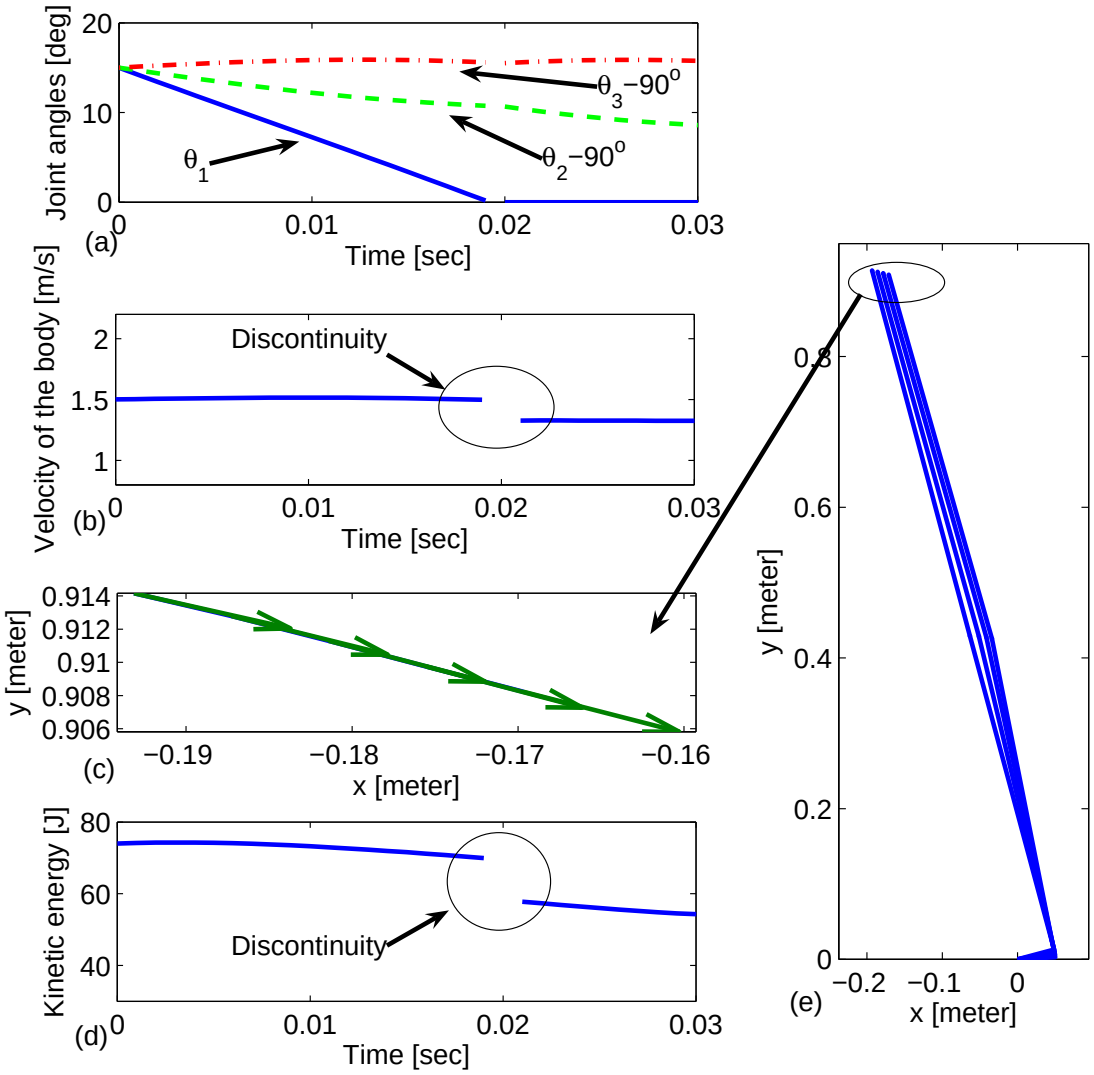

Figure 3.18: Results of the collision phase in Case 5. OLASAT on ankle joint while: $K_{sp2} = \frac{300}{R^2}\ [\frac{N}{m}]$, $\eta = 4$ *and the offset* $a = \frac{0.2618}{R}$.

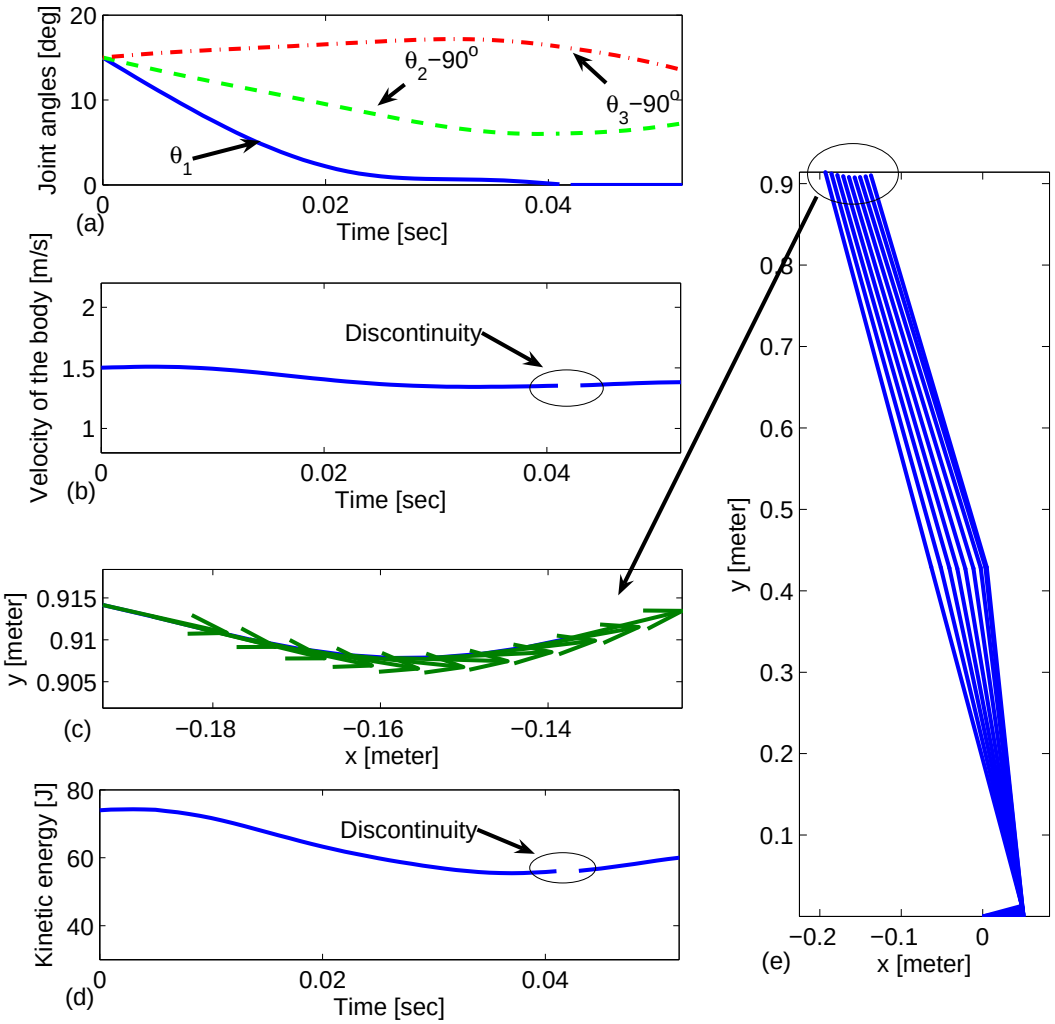

Figure 3.19: Results of the collision phase in Case 6. OLASAT on ankle joint while: $K_{sp2} = \frac{300}{R^2}\ [\frac{N}{m}]$, $\eta = 4$ *and the offset* $a = \frac{0.0349}{R}$.

Chapter 4

Adjustable Stiffness Bipedal Walking Model

Previous research illustrated that the collision of the foot with the ground in both passive dynamic and joint-angle-controlled bipedal walking approaches is inevitable and occurs frequently causing major loss of energy. Establishing a new technique to reduce this energy loss is a challenging problem which was addressed in the previous chapter. Each conceptual design of the adjustable stiffness artificial tendons (ASAT) can significantly reduce the energy loss during the collision phase. In this chapter, a new simplified model of bipedal walking is developed which includes ASAT. The conceptual design and the dynamic model of the offset location adjustable stiffness artificial tendon (OLASAT), explained in Section 3.1.3, is used which is capable of adjusting the stiffness mechanically as well as of storing and releasing the elastic energy. OLASAT is also effective in reducing the energy loss and has a simple configuration. To verify the effects of OLASAT on reducing the energy loss, a simplified model of the stance phase of the bipedal walking robot is introduced which consists of a foot, a leg, and OLASAT parallel to the ankle joint. Dynamic modeling of the biped during the double support time period is considered while the trailing leg is modeled by a pre-

deformed linear compression spring. In fact, the major injected energy to the biped is provided by the spring model during the double support period. The concept of impulsive constraints is used to establish the mathematical model of the impact events during the collision phase which consists of the heel-strike and the foot-touch-down. The organization of this chapter is as follows. The simple 2 degrees of freedom (DOF) model of the walking robot is illustrated in Section 4.1. The mathematical model of the bipedal walking is developed in Section 4.2. Section 4.3 illustrates the normalized formulation of the equations of motion of the biped. Then in Section 4.4, computer simulations are carried out to demonstrate the performance of the adjustment of the stiffness during the stance phase and during the consecutive walking steps.

4.1 Bipedal walking gait in the simplified model

A simplified model and the gait cycle of a bipedal walking robot are introduced here. The model offers different advantages. It is simple, and hence decreases the complexity of analysis in energy economy. In addition, it considers the effects of OLASAT and the foot. It also includes the double support phase and has the ability to inject energy to the biped. The dynamics of the swing leg is not considered in the model to avoid complexity of the analysis.

In the model, as shown in Figure 4.1, a rigid foot with a point mass is pivoted at the ankle joint to a rigid stance leg with a lumped mass at the hip (upper tip of the stance leg). One end of OLASAT is attached to the stance leg and the other end is attached to the foot. A cable and pulley mechanism converts the angular movement of the ankle joint to the linear deformation of the springs in OLASAT. The model also includes a massless linear spring to simulate the force of the trailing leg during the double support stance phase. The linear spring injects the energy to the biped. The input energy through the spring of the trailing leg can be adjusted by either controlling the initial deformation of the spring or adjusting its stiffness. To simplify the analysis,

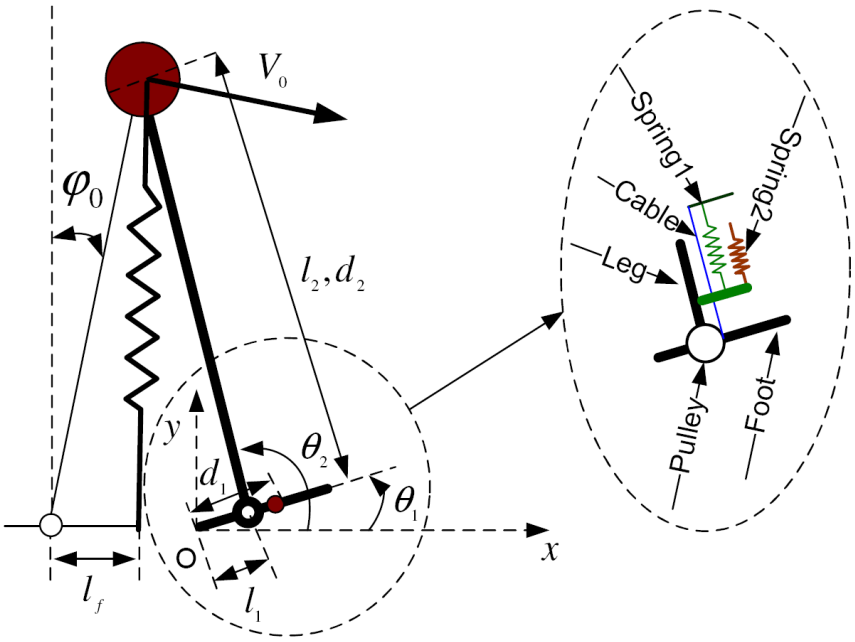

Figure 4.1: Bipedal walking model schematic diagram.

planar motion and friction-free joints are assumed in the bipedal walking model.

In general, as shown in Figure 4.2, the stance phase includes (in both single and double support periods) the collision, the rebound, and the preload phases. The collision phase starts with the impact of the heel-strike followed by continuous motion. At the end of the collision, a second impact of the foot-touch-down occurs. Both impacts are assumed to be rigid to rigid, instantaneous, and perfectly plastic, which dissipates part of the energy of the biped. In this model, the offset between the two springs of OLASAT, as shown in Figure 3.10, can be adjusted to store part of the energy of the biped during the continuous motion of the collision phase and to reduce the impact at the foot-touch-down. The offset is adjusted only once during the swing phase while there is no external load on the foot. Then it remains constant for the following supporting period. The second phase, rebound, is a continuous motion while the foot is assumed stationary on the ground. The stored energy in OLASAT during

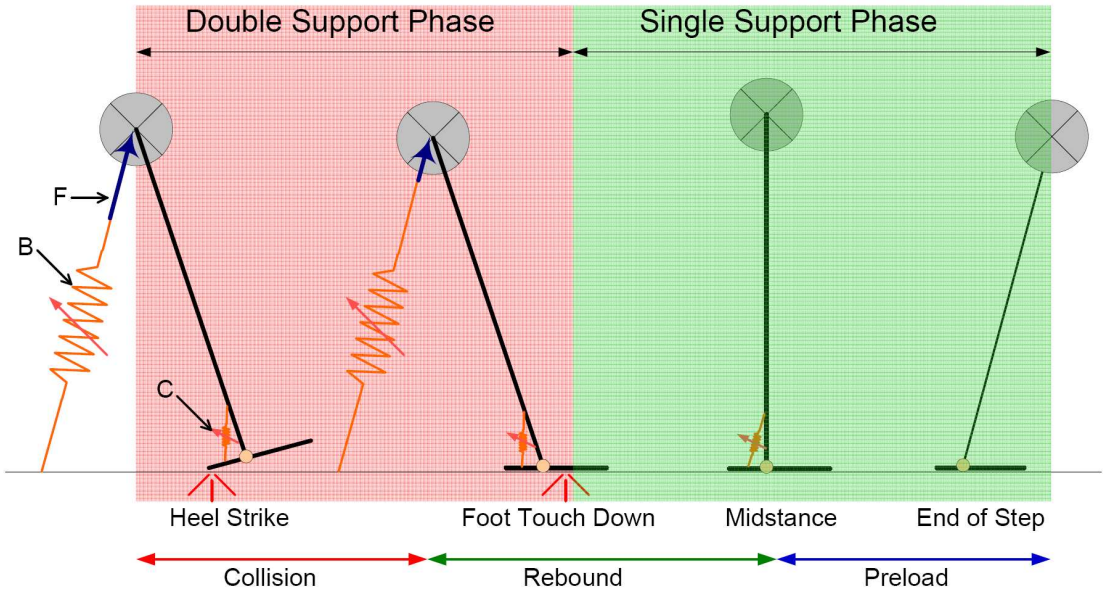

Figure 4.2: General Schematic of the bipedal gate.

the collision phase returns to the biped during the rebound phase. The rebound phase ends at midstance (biped upright position). OLASAT is passively loaded during the collision phase and is passively unloaded during the rebound phase. The motion of the biped after midstance is named the preload phase [39] which continues until the heel-strike of the following walking step. The kinematics of the heel-strike of the following walking step is specified by step length and the geometry of the robot.

The bipedal walking model in this work consists of a pre-deformed compression linear spring to simulate the force of the trailing leg. The linear spring of the trailing leg is massless with one end connected to the toe of the foot on the ground and the other to the upper tip of the stance leg as shown in Figure 4.1. It is also shown in Figure 4.2 by B. The force vector from the compliant trailing leg (F in Figure 4.2) is applied on the upper tip of the stance leg until the spring reaches its relaxed length (determining the end of the double support phase). By assuming the trailing leg as an elastic element, the model provides several advantages. The simplicity of dynamic modeling and analysis during impact events and the capability of injecting the external energy are two major

advantages. The next section describes the details of the dynamic modeling of the proposed bipedal walking model.

4.2 Dynamic modeling of the bipedal walking

In this section, the focus is on the dynamic modeling of the stance phase of the bipedal walking on level ground, which includes the collision, the rebound, and the preload phases.

In Figure 4.1, links 1 and 2 are the foot and the stance leg. d_1 is the distance between the center of mass of the foot and the heel, and d_2 is that of the body and the ankle joint. l_1 is the distance between the heel and the ankle joint. l_2 is the distance between the ankle joint and the center of mass of the body which is at the upper end of the stance leg. Thus in the model, $l_2 = d_2$. θ_1 and θ_2 are denoted as the angles of the foot and the stance leg with respect to the horizontal axis as illustrated in Figure 4.1. x_h and y_h represent the horizontal and vertical distance between the heel and a reference point O on the ground. In this work, the origin O is defined at the heel of the stance leg.

Generalized coordinates of the biped are the horizontal and vertical positions of the heel as well as foot and stance leg angles with respect to the horizontal line which correspond to x_h, y_h, θ_1, and θ_2 respectively. The perpendicular position of the foot to the stance leg is assumed as a neutral position (no force) of OLASAT in this work. The heel is assumed to be pivoted to the ground during the collision phase by assuming enough friction force between the foot and the ground. Dynamic modeling of the bipedal walking, which is detailed in the following subsections, includes the heel-strike, the continuous motion during the collision phase, and the rebound and the preload phases.

4.2.1 The heel-strike

At the beginning of the stance phase, the heel contacts the ground with impact. The impact is assumed as an impulsive constraint of a sudden change in the velocity of the heel to zero. The foot and the leg angular velocities are also subjected to a sudden change resulting from this impact event. At the heel-strike, there is an impulsive force between the heel and the ground. The external moment at each joint is taken to be negligible during impact. For the sake of of simplicity, impulsive constraints relations [110] are employed in this work to provide the angular velocities of the foot and the leg after the heel-strike. Since no detailed information is available from the literature, the derivations and complete forms of the constrained impulsive motion equations are presented here.

By applying the impulsive constraint relations [110], the Lagrange multiplier form of the constrained impulsive motion equation at the heel-strike is shown below.

$$\sum_{j=1}^{4} D_{ij}(\dot{q}_j^+ - \dot{q}_j^-) = \hat{Q}_i + \sum_{k=1}^{n} \hat{\lambda}_k a_{ki} \qquad (i = 1, 2, ..., 4) \tag{4.1}$$

where

$$\dot{\mathbf{q}} = (\dot{x}_h, \dot{y}_h, \dot{\theta}_1, \dot{\theta}_2) \tag{4.2}$$

$$D_{ij} = \frac{\partial^2 K}{\partial \dot{q}_i \partial \dot{q}_j} \qquad (i, j = 1, 2, ..., 4) \tag{4.3}$$

$\mathbf{q}$ is a 4×1 generalized coordinate vector and K is the kinetic energy of the biped (shown in Section 4.2.2). $\dot{x}_h$ and $\dot{y}_h$ are the horizontal and vertical velocities of the heel. $\dot{\theta}_1$ and $\dot{\theta}_2$ are the angular velocities of the foot and the leg. The superscripts $'+'$ and $'-'$ represent the time immediately after and before the impact. n is the maximum

number of impulsive constraints which equals 2. D_{ij} are elements of a 4×4 inertia matrix which are calculated from the kinetic energy of the biped.

In this paper, it is also assumed that the heel-strike is not accompanied by an external impulse, $\hat{Q}_i$. Thus

$$\hat{Q}_i = 0 \qquad (i = 1, 2, ..., 4) \tag{4.4}$$

The term $\sum_{k=1}^{n} \hat{\lambda}_k a_{ki}$ in Eqn.(4.1) corresponds to constraint impulse and $\hat{\lambda}_k$ is an impulsive Lagrangian multiplier.

The heel-strike consists of the constraints $\Delta\dot{x}_h = {}^{HS}\dot{x}_h^+ - {}^{HS}\dot{x}_h^- = - {}^{HS}\dot{x}_h^-$ and $\Delta\dot{y}_h = {}^{HS}\dot{y}_h^+ - {}^{HS}\dot{y}_h^- = - {}^{HS}\dot{y}_h^-$ that correspond to the zero velocity of the heel immediately after the heel-strike. The superscript HS corresponds to the instant of the heel-strike. The generalized coordinate vector $\mathbf{q}$ is divided into two 1×2 vectors of $\mathbf{q}_1 = (x_h, y_h)$ and $\mathbf{q}_2 = (\theta_1, \theta_2)$. In addition, it is assumed that the initial conditions of the robot before the heel-strike ($\dot{\mathbf{q}}_1^-$ and $\dot{\mathbf{q}}_2^-$) are given. Thus, to solve the angular velocities of the biped, Eqn.(4.1) is shown in the following matrix format:

$$\begin{bmatrix} D1 & D2 \\ D3 & D4 \end{bmatrix} \begin{bmatrix} \Delta\dot{\mathbf{q}}_1 \\ \Delta\dot{\mathbf{q}}_2 \end{bmatrix} = \begin{bmatrix} {}^{HS}\hat{\lambda} \\ 0 \end{bmatrix} \tag{4.5}$$

where $D1$ and $D2$ are 2×2 matrices:

$$D1 = \begin{bmatrix} m_1 + m_2 & 0 \\ 0 & m_1 + m_2 \end{bmatrix} \tag{4.6}$$

$$D2 = \begin{bmatrix} m_1 d_1 + m_2 l_1 sin(\theta_1) & m_2 d_2 \\ m_1 d_1 + m_2 l_1 cos(\theta_1) & m_2 d_2 \end{bmatrix} \tag{4.7}$$

m_1 and m_2 are the foot and the body mass. D3 is the transpose matrix of D2.

$$D3 = D2^T \tag{4.8}$$

and D4 is a 2×2 matrix:

$$D4 = \begin{bmatrix} m_1 d_1^2 + m_2 l_1^2 & m_2 d_2 l_1 \cos(\theta_1 - \theta_2) \\ m_2 d_2 l_1 \cos(\theta_2 - \theta_1) & m_2 d_2^2 \end{bmatrix} \tag{4.9}$$

The impulsive Lagrangian multiplier, ${}^{HS}\hat{\lambda}$, at the heel-strike is a 2×1 vector. Therefore, by solving Eqn.(4.1), the angular velocities of the links after the heel-strike are defined:

$$\dot{\mathbf{q}}_2^+ = \dot{\mathbf{q}}_2^- - D4^{-1} D3(\Delta \dot{\mathbf{q}}_1) \tag{4.10}$$

The impulse caused by the impact event at the heel-strike can also be calculated:

$${}^{HS}\hat{\lambda} = D1(\Delta \dot{\mathbf{q}}_1) + D2(\Delta \dot{\mathbf{q}}_2) \tag{4.11}$$

After the heel-strike, the degrees of freedom of the biped are reduced. Respectively, the generalized coordinates vector of the robot reduces to $\mathbf{q} = (\theta_1, \theta_2)$ and also the inertia is reduced to a 2×2 matrix. The equations of the continuous motion of the robot are given in the next section.

4.2.2 The continuous motion of the collision phase

According to Figure 4.1, the coordinates of the mass center of link i are:

$$x_{ci} = x_h + d_i \cos(\theta_i) + \sum_{j=1}^{i-1} l_j \cos(\theta_j) \tag{4.12}$$

$$y_{ci} = y_h + d_i \sin(\theta_i) + \sum_{j=1}^{i-1} l_j \sin(\theta_j) \tag{4.13}$$

The potential energy (assume $P = 0$ at the ground level) of the two-link biped is:

$$P = \sum_{i=1}^{2} m_i g y_{ci} \tag{4.14}$$

The elastic torque of OLASAT is included as a force vector in dynamic equations and is not considered in the Lagrangian function. The kinetic energy is:

$$K = \sum_{i=1}^{2} \frac{1}{2} m_i (\dot{x}_{ci}^2 + \dot{y}_{ci}^2) \tag{4.15}$$

By applying Eqn.(4.14) and Eqn.(4.15) to the Lagrangian equations, the dynamic equation of the biped during the continuous motion of the collision phase is given below:

$$M(\theta)\ddot{\theta} + H(\theta, \dot{\theta})\dot{\theta} + G(\theta) + S(\theta) = I(\theta) \tag{4.16}$$

θ, $\dot{\theta}$, $\ddot{\theta}$, and $I(\theta)$ are the 3×1 vectors of generalized coordinates, velocities, accelerations and external torques respectively ([111, 112]). $M(\theta)$ is a 2×2 positive definite and symmetric inertia matrix which is shown below:

$$M = \begin{bmatrix} m_1 d_1^2 + m_2 l_1^2 & m_2 d_2 l_1 \cos(\theta_1 - \theta_2) \\ m_2 d_2 l_1 \cos(\theta_2 - \theta_1) & m_2 d_2^2 \end{bmatrix} \tag{4.17}$$

$H(\theta, \dot{\theta})$ is a 2×2 matrix related to centrifugal and coriolis terms:

$$H = \begin{bmatrix} 0 & m_2 d_2 l_1 \sin(\theta_2 - \theta_1)\dot{\theta}_2 \\ m_2 d_2 l_1 \sin(\theta_1 - \theta_2)\dot{\theta}_1 & 0 \end{bmatrix} \tag{4.18}$$

$G(\theta)$ is a 2×1 vector of the gravitational torque as follows:

$$G = \begin{bmatrix} (m_1 d_1 + m_2 l_1) g \cos(\theta_1) \\ m_2 d_2 g \cos(\theta_2) \end{bmatrix} \tag{4.19}$$

The torque related to OLASAT is shown in a 2×1 vector defined by $S(\theta)$.

$$S = \begin{bmatrix} -R^2 K_{sp1}(\Delta\theta - \frac{\pi}{2}) - \gamma R^2 K_{sp2}(\Delta\theta - \frac{\pi}{2} - a/R) \\ R^2 K_{sp1}(\Delta\theta - \frac{\pi}{2}) + \gamma R^2 K_{sp2}(\Delta\theta - \frac{\pi}{2} - a/R) \end{bmatrix} \tag{4.20}$$

$\Delta\theta = \theta_2 - \theta_1$ and R is the radius of the pulley at the ankle joint. K_{sp1} and K_{sp2} are the stiffnesses of the springs 1 and 2 in OLASAT at the ankle joint. a is the offset of the OLASAT. As mentioned in the last section, OLASAT is in neutral position while the foot is perpendicular to the stance leg. Also:

$$\gamma = \begin{cases} 0 & (\Delta\theta - \frac{\pi}{2}) \ < a/R \\ \\ 1 & (\Delta\theta - \frac{\pi}{2}) \ \geq a/R \end{cases} \tag{4.21}$$

$\gamma = 0$ denotes that only spring 1 is engaged and $\gamma = 1$ means that both springs in OLASAT are engaged. The force vector representing the trailing leg during the double support period is converted to the joint torques using the Jacobian matrix, the deformation of the trailing leg, and its stiffness (K_t). $I(\theta)$ is a 2×1 dimension vector, each element of which consists of the exerted torque from the trailing leg at the heel and at the ankle joint during the double support phase. $I(\theta)$ is given below:

$$I = \begin{bmatrix} -Fl_1 \sin(\theta_1)\cos(\delta) + Fl_1 \cos(\theta_1)\sin(\delta) \\ -Fl_2 \sin(\theta_2)\cos(\delta) + Fl_2 \cos(\theta_2)\sin(\delta) \end{bmatrix} \tag{4.22}$$

where δ is the angle of the spring model of the trailing leg with respect to the horizontal line. $F = \iota K_t(L_0 - L_t)$ is the force generated by the trailing leg during the double support period. L_0 is the relaxed length of the trailing leg spring and L_t is the distance between the COM of the body and the toe of the trailing leg. L_t is calculated by the equation below.

$$L_t = \sqrt{(l_{step} - l_1 - l_f + l_1\cos(\theta_1) + l_2\cos(\theta_2))^2 + (l_1\sin(\theta_1) + l_2\sin(\theta_2))^2} \quad (4.23)$$

l_f is the distance between the toe and the ankle joint. l_{step} is the step length of the biped:

$$l_{step} = l_1 + l_2\sin(\varphi_0) + l_1\cos({}^{HS}\theta_1^-) + l_2\cos({}^{HS}\theta_2^-) \quad (4.24)$$

where ${}^{HS}\theta_1^-$ and ${}^{HS}\theta_2^-$ are the initial angles of the foot and the leg immediately before the heel-strike. φ_0 is the final angle of the stance leg in the previous walking step with respect to the vertical line, shown in Figure 4.1. The parameter ι models the compressional spring behavior of the trailing leg spring, where

$$\iota = \begin{cases} 1 & L_t \leq L_0 \\ 0 & L_t > L_0 \end{cases} \quad (4.25)$$

Here, the initial force through the trailing leg during the double support phase depends on the step length, leg geometry, the relaxed length of the spring, and the stiffness of the compressional spring. This force can be generated by actuating system on the trailing leg of the robot which is not covered in the thesis.

4.2.3 The foot-touch-down

The foot-touch-down (FTD) is the instant the collision phase ends which is accompanied by a sudden change in the angular velocity of the foot to zero caused by impact. It also causes a sudden change in the angular velocity of the stance leg which is calculated in this section. In this work, the foot-touch-down impact is modeled by the constraint equation shown below.

$$\begin{aligned} \Delta^{FTD}\dot{\theta}_1 &= {}^{FTD}\dot{\theta}_1^+ - {}^{FTD}\dot{\theta}_1^- \\ &= -{}^{FTD}\dot{\theta}_1^- \end{aligned} \tag{4.26}$$

${}^{FTD}\dot{\theta}_1^-$ and ${}^{FTD}\dot{\theta}_1^+$ are the angular velocities of the foot immediately before and after the foot-touch-down. The above equation shows that the angular velocity of the foot suddenly changes to zero. The angular velocity of the leg immediately after the foot-touch-down, ${}^{FTD}\dot{\theta}_2^+$, is calculated in Eqn.(4.28) using the constraint Eqn.(4.27).

$$\begin{bmatrix} m_1 d_1^2 + m_2 l_1^2 & m_2 d_2 l_1 \cos(\theta_1 - \theta_2) \\ m_2 d_2 l_1 \cos(\theta_2 - \theta_1) & m_2 d_2^2 \end{bmatrix} \begin{bmatrix} {}^{FTD}(\dot{\theta}_1^+ - \dot{\theta}_1^-) \\ {}^{FTD}(\dot{\theta}_2^+ - \dot{\theta}_2^-) \end{bmatrix} = \begin{bmatrix} {}^{FTD}\hat{\lambda}_{FTD} \\ 0 \end{bmatrix} \tag{4.27}$$

$${}^{FTD}\dot{\theta}_2^+ = {}^{FTD}\dot{\theta}_2^- + \frac{l_1 \cos(\theta_2 - \theta_1)\ {}^{FTD}\dot{\theta}_1^-}{d_2} \tag{4.28}$$

The impulsive Lagrangian multiplier at the foot-touch-down, ${}^{FTD}\hat{\lambda}$, is:

$${}^{FTD}\hat{\lambda} = -(m_1 d_1^2 + m_2 l_1^2)^{FTD}\dot{\theta}_1^- + m_2 l_1^2 \cos^2(\theta_1 - \theta_2)^{FTD}\dot{\theta}_1^- \tag{4.29}$$

After the foot-touch-down, the generalized coordinate vector of the biped is changed to $\mathbf{q} = \theta_2$. The next section describes the equations of motion in the rebound and the

preload phases.

4.2.4 The rebound and the preload phases

The rebound phase is a continuous motion starting immediately after the FTD whereby the foot is assumed to be stationary on the ground in which $\theta_1 = 0$. The equation of motion during the rebound phase is described below.

$$m_2 d_2^2 \ddot{\theta}_2 + m_2 d_2 g \cos(\theta_2) + R^2 K_{sp1}(\theta_2 - \frac{\pi}{2}) + \gamma R^2 K_{sp2}(\theta_2 - \frac{\pi}{2} - \frac{a}{R}) = \\ = -F l_2 \sin(\theta_2)\cos(\delta) + F l_2 \cos(\theta_2)\sin(\delta) \tag{4.30}$$

The preload phase is a continuous motion of the leg as an inverted pendulum and it starts after midstance. However, assuming a second OLASAT during the preload phase may improve the energetics of the biped by reducing the angular velocity of the stance leg before the following heel-strike which is left for future research. In this work the biped is only under gravitational forces due to the uni-directional property of OLASAT. The equation of motion during the preload phase is given below.

$$\ddot{\theta}_2 + \frac{g}{d_2}\cos(\theta_2) = 0 \tag{4.31}$$

The equations of motion in the normalized form with dimensionless parameters can help one to study more efficiently the bipedal walking motion in generalized form. It also assists in the parametric follow-up study. The next section presents the normalized form of the equations of motion covered in the above sections.

4.3 Equations of motion in normalized form

The dimensionless parameters of the model are specified and listed in Table 4.1. The equations of motion are normalized by $m_2 l_2^2$, the inertia of the stance leg about the ankle joint. Finally, by replacing the dimensionless parameters into the normalized

Table 4.1: Dimensionless Parameters.

Parameters	β	ψ	ζ	υ	ς	η	ν
Equivalence	$\frac{m_1}{m_2}$	$\frac{l_1}{l_2}$	$\frac{d_1}{l_2}$	$\frac{l_f}{l_2}$	$\frac{K_{sp1}R^2}{m_2 l_2 g}$	$\frac{K_{sp2}}{K_{sp1}}$	$\frac{K_t l_2}{m_2 g}$

form of the equations of motion, the normalized form of the equations of motion are arrived at. The normalized form of the dynamics equation at the heel-strike appears below.

$$\begin{bmatrix} \frac{\beta+1}{l_2^2} & 0 & \frac{\beta\zeta+\psi\sin(\theta_1)}{l_2} & \frac{1}{l_2} \\ 0 & \frac{\beta+1}{l_2^2} & \frac{\beta\zeta+\psi\cos(\theta_1)}{l_2} & \frac{1}{l_2} \\ \frac{\beta\zeta+\psi\sin(\theta_1)}{l_2} & \frac{\beta\zeta+\psi\cos(\theta_1)}{l_2} & \beta\zeta^2+\psi^2 & \psi\cos(\Delta\theta) \\ \frac{1}{l_2} & \frac{1}{l_2} & \psi\cos(\Delta\theta) & 1 \end{bmatrix} \begin{bmatrix} -{}^{HS}\dot{x}^- \\ -{}^{HS}\dot{y}^- \\ {}^{HS}(\dot{\theta}_1^+ - \dot{\theta}_1^-) \\ {}^{HS}(\dot{\theta}_2^+ - \dot{\theta}_2^-) \end{bmatrix} = \begin{bmatrix} \frac{{}^{HS}\hat{\lambda}_1}{m_2 d_2^2} \\ \frac{{}^{HS}\hat{\lambda}_2}{m_2 d_2^2} \\ 0 \\ 0 \end{bmatrix} \tag{4.32}$$

where $\Delta\theta = \theta_1 - \theta_2$. The normalized form of the equations of motion at the foot-touchdown is

$$\begin{bmatrix} \beta\zeta^2+\psi^2 & \psi\cos(\Delta\theta) \\ \psi\cos(\Delta\theta) & 1 \end{bmatrix} \begin{bmatrix} -{}^{FTD}\dot{\theta}_1^- \\ {}^{FTD}(\dot{\theta}_2^+ - \dot{\theta}_2^-) \end{bmatrix} = \begin{bmatrix} \frac{{}^{FTD}\hat{\lambda}}{m_2 d_2^2} \\ 0 \end{bmatrix} \tag{4.33}$$

Eqn.(4.34) is the normalized counterpart of Eqn.(4.16).

$$\hat{M}(\theta)\ddot{\theta} + \hat{H}(\theta,\dot{\theta})\dot{\theta} + \hat{G}(\theta) + \hat{S}(\theta) = \hat{I}(\theta) \tag{4.34}$$

where

$$\hat{M} = \begin{bmatrix} \beta\zeta^2+\psi^2 & \psi\cos(\Delta\theta) \\ \psi\cos(\Delta\theta) & 1 \end{bmatrix} \tag{4.35}$$

$$\hat{H} = \begin{bmatrix} 0 & \psi \sin(\theta_2 - \theta_1)\dot{\theta}_2 \\ \psi \sin(\theta_2 - \theta_1)\dot{\theta}_1 & 0 \end{bmatrix} \tag{4.36}$$

$$\hat{G} = \begin{bmatrix} \frac{\beta\zeta+\psi}{l_2} g \cos(\theta_1) \\ \frac{g}{l_2} \cos(\theta_2) \end{bmatrix} \tag{4.37}$$

$$\hat{S} = \frac{\varsigma}{l_2} \begin{bmatrix} -g(\Delta\theta - \frac{\pi}{2}) - \gamma\eta g(\Delta\theta - \frac{\pi}{2} - a/R) \\ g(\Delta\theta - \frac{\pi}{2}) + \gamma\eta g(\Delta\theta - \frac{\pi}{2} - a/R) \end{bmatrix} \tag{4.38}$$

$$\hat{I} = \begin{bmatrix} -\frac{\iota\nu g(L_0 - L_t)\beta}{l_2^2} \sin(\theta_1)\cos(\delta) + \frac{\iota\nu g(L_0 - L_t)\beta}{l_2^2} \cos(\theta_1)\sin(\delta) \\ -\frac{\iota\nu g(L_0 - L_t)\beta}{l_2^2} \sin(\theta_2)\cos(\delta) + \frac{\iota\nu g(L_0 - L_t)\beta}{l_2^2} \cos(\theta_2)\sin(\delta) \end{bmatrix} \tag{4.39}$$

The equations of motion during rebound is

$$\begin{aligned} &\ddot{\theta}_2 + \frac{g}{l_2}\cos(\theta_2) + \varsigma\frac{g}{l_2}(\theta_2 - \frac{\pi}{2}) + \gamma\eta\varsigma\frac{g}{l_2}(\theta_2 - \frac{\pi}{2} - \frac{a}{R}) \\ &= -\frac{\iota\nu g(L_0 - L_t)\beta}{l_2^2}\sin(\theta_2)\cos(\delta) + \frac{\iota\nu g(L_0 - L_t)\beta}{l_2^2}\cos(\theta_2)\sin(\delta) \end{aligned} \tag{4.40}$$

The next section shows the simulation results related to the energy economy of the bipedal walking when OLASAT is incorporated.

4.4 The study of energy economy using simulations

The effects of the adjustable stiffness artificial tendon on the energetics of bipedal walking is studied in this section through computer simulations. In Section 4.4.1, the simulation results of bipedal walking are illustrated during the single support phase for

Table 4.2: Parameters used in the simulations.

Parameters	β	ψ	ζ	υ	ς	η
Value	0.02	0.05	0.07	0.1	0.3	4

a single walking step. The same initial conditions are chosen in Section 4.4.1 for two different stiffness values of OLASAT. The simulation results illustrate significant improvement in reducing the energy loss by proper adjustment of the stiffness of OLASAT. Then, the simulation results of the robot during single support phase are presented for 5 consecutive walking steps which compare the two cases of the poorly-adjusted and the well-adjusted stiffness of OLASAT.

4.4.1 Stance phase of bipedal walking during a single walking step

In this section, a realization of the single support phase of bipedal walking is demonstrated for two different stiffness values of OLASAT during a single walking step. In order to study the effects of stiffness adjustment on the energy economy of the biped, simulations are performed for the same initial conditions. The offset values are set to two extreme cases representing a poorly-adjusted stiffness and a well-adjusted stiffness. The parameters of the biped in computer simulations are listed in Table 4.2 in addition to $m_2 = 1kg$ and $l_2 = 1.0m$. The initial conditions of the biped immediately before the heel-strike in the simulation are specified as follows: ${}^{HS}\theta_1^- = 15^o$, ${}^{HS}\theta_2^- = 105^o$, $x_h = y_h = 0$, ${}^{HS}\dot{\theta}_1^- = {}^{HS}\dot{\theta}_2^- = 0$ and $\varphi_0 = 11.7^o$. The initial translational velocity V_0 of the biped before the heel-strike has the magnitude of $1.5m/s$ with the horizontal angle of $-\varphi_0$.

Using those initial conditions, the total kinetic energy of the biped before the heel-strike is equal to 1.125 [J]. The stiffness of the trailing leg spring is assumed zero in this section, ($\nu = 0$), to simulate the biped's motion with no external elastic energy

input. Note that the dynamics of the swing leg is not assumed in the model.

Figures 4.3 and 4.4 show the simulation results of the biped in case 1 (poorly-adjusted stiffness) and case 2 (well-adjusted stiffness). OLASAT's offset values for case 1 and 2 give $\frac{a}{R} = 15^o$ and $\frac{a}{R} = 3.5^o$ respectively. In case 1, only spring 1 is involved in OLASAT which is the minimum stiffness of OLASAT. In case 2 the offset is well-adjusted using a trial and error procedure which reduces the angular velocity of the foot before the foot-touch-down to decrease the energy loss. Figures 4.3a and 4.4a show the joint angles of the biped θ_1, θ_2 which indicate that the motion of the biped is sustained in both cases as also shown in the stick diagram of the biped in Figures 4.3e and 4.4e. Figures 4.3b and 4.4b show the magnitude of the velocity vector of the COM of the body. As shown in Figures 4.3b and 4.4b, the velocity jump of the COM of the body during the FTD in case 2, which equals 0.01 $\frac{m}{sec}$, is significantly lower than case 1, which equals 0.2 $\frac{m}{sec}$. Consequently, the final velocity of the COM of the body is higher in case 2 compared to case 1. These results indicate that the biped can sustain the motion during the stance phase in both cases. Dimensionless kinetic energy κ, is defined as the ratio of the kinetic energy of the biped to its gravitational potential energy at midstance, $m_2 l_2 g$. Figures 4.3c and 4.4c depict the κ versus time, and the comparison of the results indicates that the kinetic energy loss at the FTD is significantly reduced in case 2, that is by 1%, resulting from the proper adjustment of the OLASAT, compared to the κ in case 1 which is as high as 29%. These results illustrate the effects of OLASAT on the energetics of the bipedal walking. The significant reduction in energy loss during the FTD in the well-adjusted stiffness case results in higher final velocity of the body compared to the poorly-adjusted stiffness case. The displacement of the COM of the body during the collision phase together with its velocity vector is shown in Figures 4.3d and 4.4d. Figure 4.4d shows that the vertical component of the velocity of the body's COM is gradually decreased during the collision phase which can reduce the energy loss at the FTD as discussed in Section 5.1. The dimensionless parameter of

τ_{ankle} is the ratio of the torque of the ankle joint exerted by OLASAT to m_2gl_2 during the single support stance phase. The graph of τ_{ankle} versus time is given in Figure 4.5 for the above two cases. In case 1, only spring 1 of OLASAT is engaged. The exerted torque by OLASAT in case 1 is much lower than case 2. As shown in Figure 4.5, the graphs include different sudden changes of slopes of the τ_{ankle} in the time period of the stance phase. In case 1, this behavior is caused by the end of the collision phase defined by point B and by the end of the rebound phase defined by F. OLASAT performs differently in case 2 while both of the springs are engaged in part of the time period of the motion. At the beginning of case 2, spring 2 is not engaged. After A in Figure 4.5, both springs are engaged and they will remain engaged up to D. The change of slope in case 2 at C occures at the end of the collision phase. Point E is also defined by the end of the rebound phase in case 2. Figure 4.5 indicates that by reducing the offset of OLASAT more energy is stored and released during the stance phase. To continue this study, the next section illustrates the effectiveness of adjusting the stiffness of the OLASAT in consecutive walking steps.

4.4.2 Bipedal walking simulations in consecutive steps

In the last section, bipedal walking with constant step length was realized by implementing the OLASAT at the ankle joint. In this section, the simulation results of the bipedal walking in consecutive steps are presented. The goal is to demonstrate and quantify the effects of properly adjusting the stiffness of the ankle joint on multiple steps of the bipedal walking. For the first walking step, the same biped configuration and the same initial conditions as in Section 4.4.1 are used. The biped is moving on level ground. To demonstrate the kinetic energy loss of the biped in this section, we defined $\Delta\kappa_n$ as the dimensionless ratio of the total kinetic energy loss of the biped after n walking steps to the gravitational potential energy of the biped, m_2gl_2, at the midstance.

Figures 4.6 and 4.7 show the stick diagram and the velocity of the COM of the body in 5 consecutive steps for case 1. As shown in Figure 4.6, the motion of the biped is sustained in all 5 consecutive walking steps. Figure 4.7 illustrates how stepping forward increases the period of each walking step. Reducing the average velocity of the biped is caused by the energy loss of the impact events. The final velocity of the COM of the body after the fifth step equals $0.75\frac{m}{sec}$ which is half of the initial velocity of at the first step ($1.5\frac{m}{sec}$). On average, for the poorly-adjusted stiffness of the OLASAT, 13% of the kinetic energy of the biped is dissipated in each step and $\Delta\kappa_5 = 0.0921$.

To demonstrate the impact of stiffness adjustment on improving the energetics of the biped, Figures 4.8 and 4.9 show the stick diagram and the velocity of the body's COM in 5 consecutive steps for case 2. Figure 4.8 demonstrates that the motion of the biped is sustained in all steps. The final velocity of the COM of the body after the fifth step equals $1.4\frac{m}{sec}$ which is close to the initial velocity of $1.5\frac{m}{sec}$. On average, well-adjusted stiffness in OLASAT dissipates 1.4% of the kinetic energy of the biped in each walking step when $\Delta\kappa_5 = 0.064$. These results show how the proper adjustment of the stiffness of the OLASAT significantly improves the energetics of the biped and makes it more efficient. This justifies the developement of an automated stiffness adjustment controller which will be addressed in Section 5.2. The next section presents the results of the implementation of the above mentioned controller.

4.5 Summary

This chapter presented the results of the effects of stiffness adjustment of the ankle joint on energetics of the bipedal walking robots. A methodology to reduce the energy loss was presented through two main efforts. First, a simplified model of the bipedal walking robot in the stance phase was developed consisting of a foot, a leg, and an OLASAT which is installed parallel to the ankle joint. The model includes a compliant trailing leg which simulates the force generated by the trailing leg during the double

support stance phase. The concept of impulsive constraints was used to establish the mathematical model of the collision phase which includes the heel-strike and the foot-touch-down. Such a model was used to compare the effects of a poorly-adjusted and a well-adjusted stiffness OLASAT on reducing the energy loss at the foot-touch-down. Second, computer simulations were carried out to compare the energy loss of the biped in the two cases of the poorly-adjusted and the well-adjusted stiffness OLASAT. Proper adjustment of the stiffness can significantly reduce the kinetic energy loss during the foot-touch-down from 29% (of the poorly-adjusted stiffness) to 1%. Simulation results of the biped during multiple walking steps illustrate that proper stiffness adjustment of OLASAT significantly improves the energetics of the bipedal walking. On average, the kinetic energy loss during multiple walking steps is reduced from 13% to 1.4% in each walking step. In general, the simulation results of this thesis suggest that various designs of the adjustable stiffness artificial tendons can be included in robot structures to achieve better energetics.

Future directions of this research may include studying the effects of adjusting the stiffness of OLASAT and that of energy injection during the double support phase through the elastic trailing leg. The role of automatic stiffness adjustment of OLASAT and the stiffness adjustment of the trailing leg spring will be addressed in the next chapter.

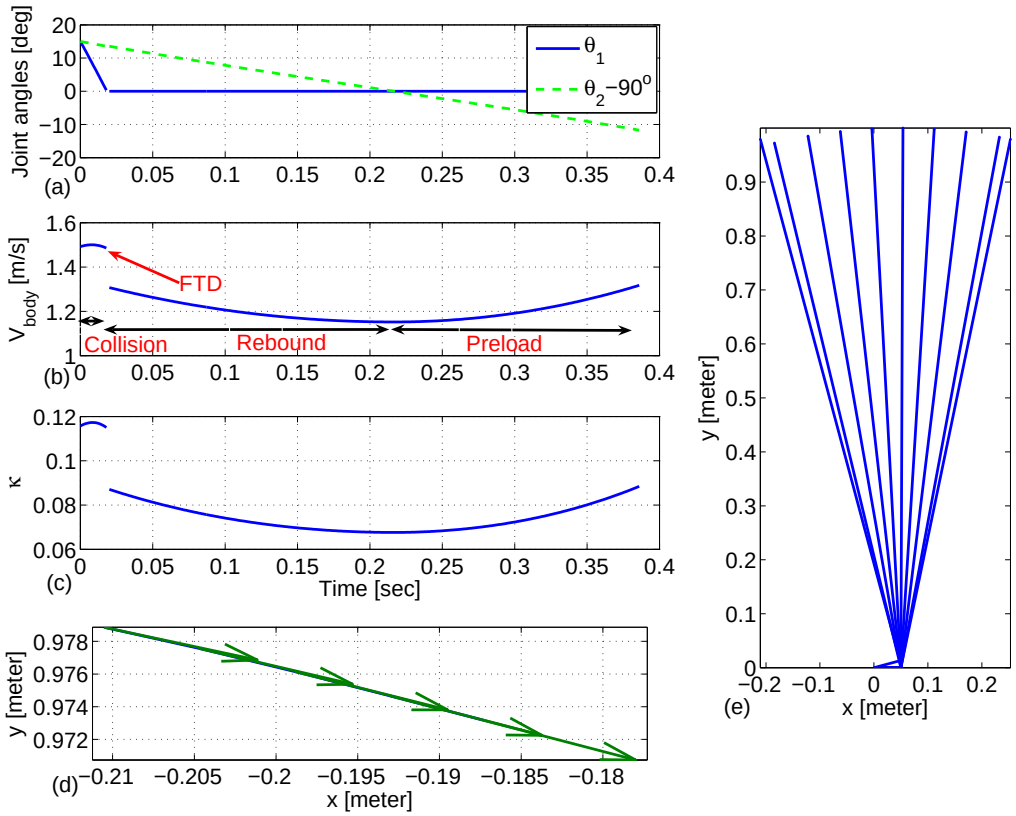

Figure 4.3: Simulation results during the single support stance period for poorly-adjusted stiffness of OLASAT. (a)- Joint angles vs. time. (b)- Velocity of the COM of the body vs. time. (c)- Dimensionless kinetic energy of the biped vs time. (d)- Position and velocity vector of the COM of the body during the collision phase. (e)- Stick diagram of the links of the biped.

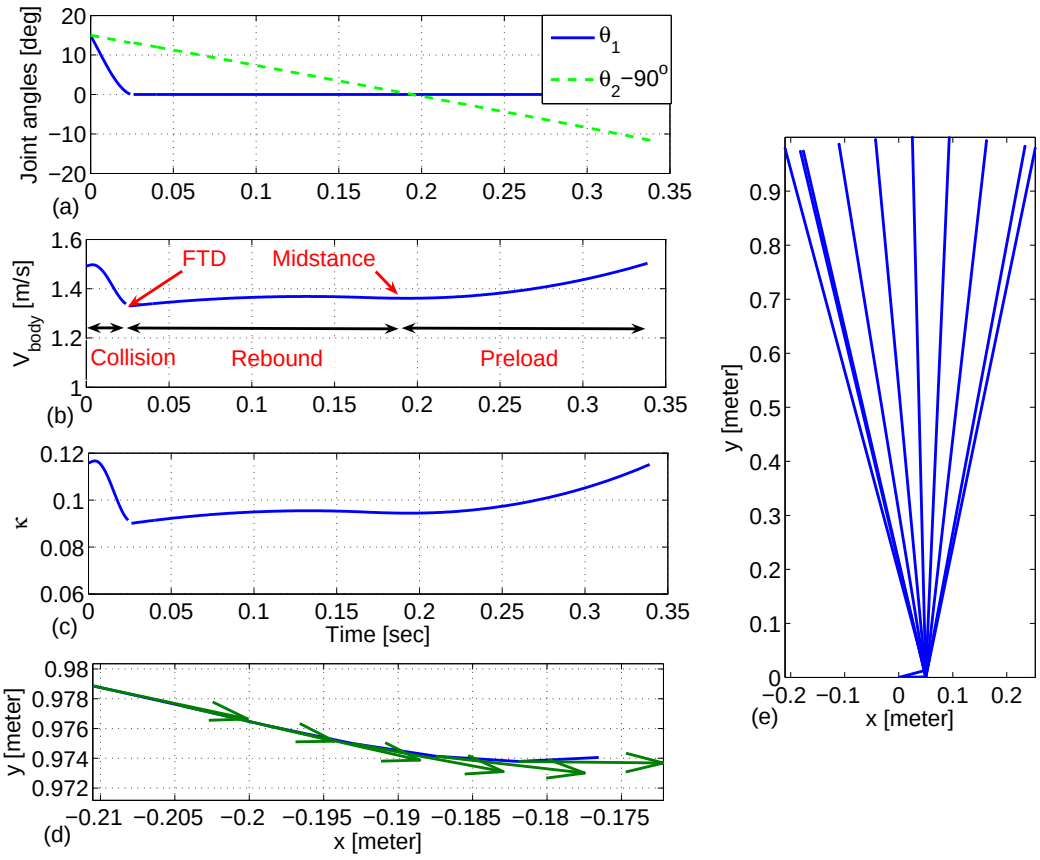

Figure 4.4: Simulation results during the single support stance period for well-adjusted stiffness of OLASAT. (a)- Joint angles vs. time. (b)- Velocity of the COM of the body vs. time. (c)- Dimensionless kinetic energy of the biped vs time. (d)- Position and velocity vector of the COM of the body during the collision phase. (e)- Stick diagram of the links of the biped.

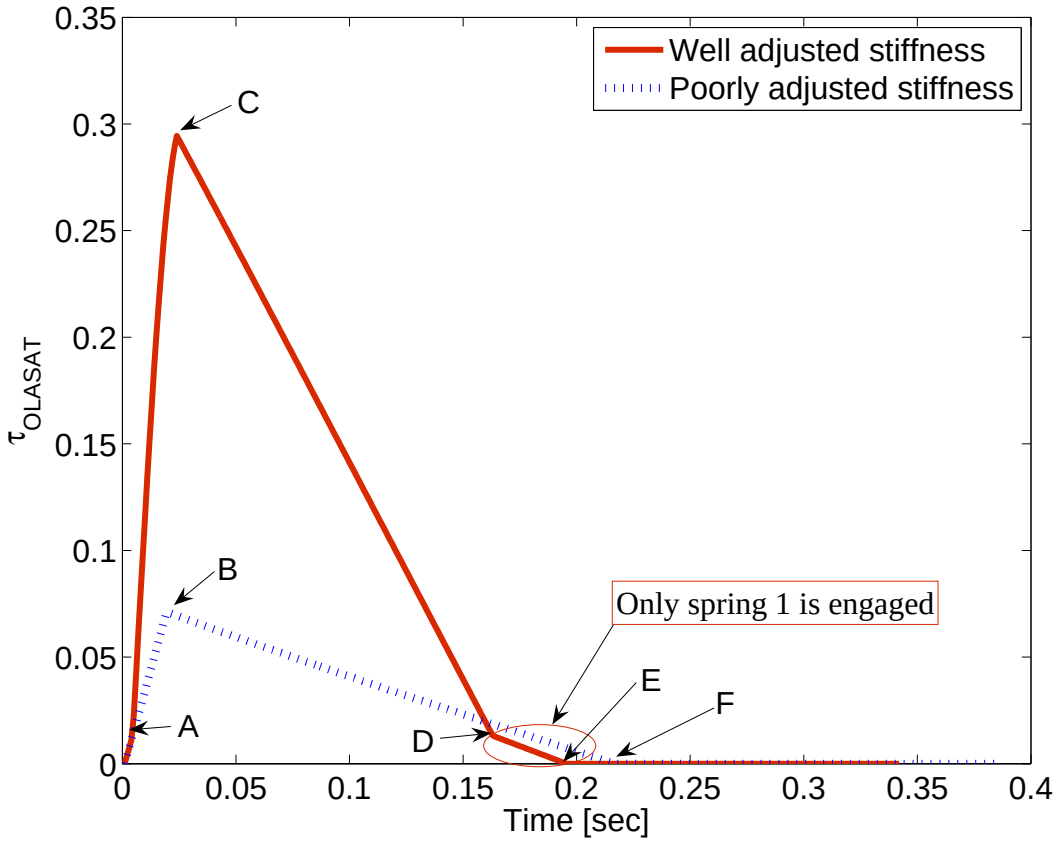

Figure 4.5: Dimensionless torque of OLASAT vs. time during single support stance phase for both case 1 and case 2.

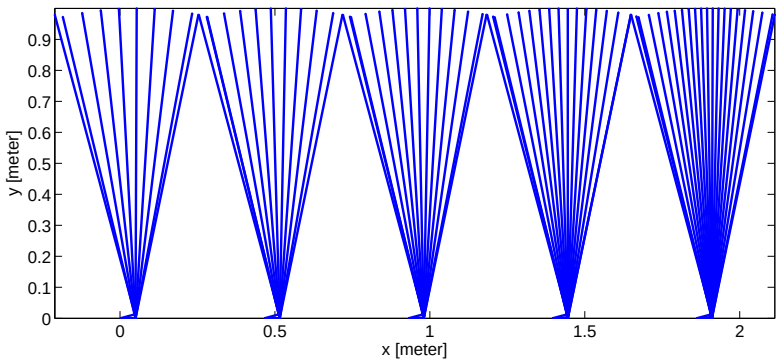

Figure 4.6: Stick diagram of the links of the biped during 5 multiple walking steps for poorly-adjusted ($\frac{a}{R} = 15deg$).

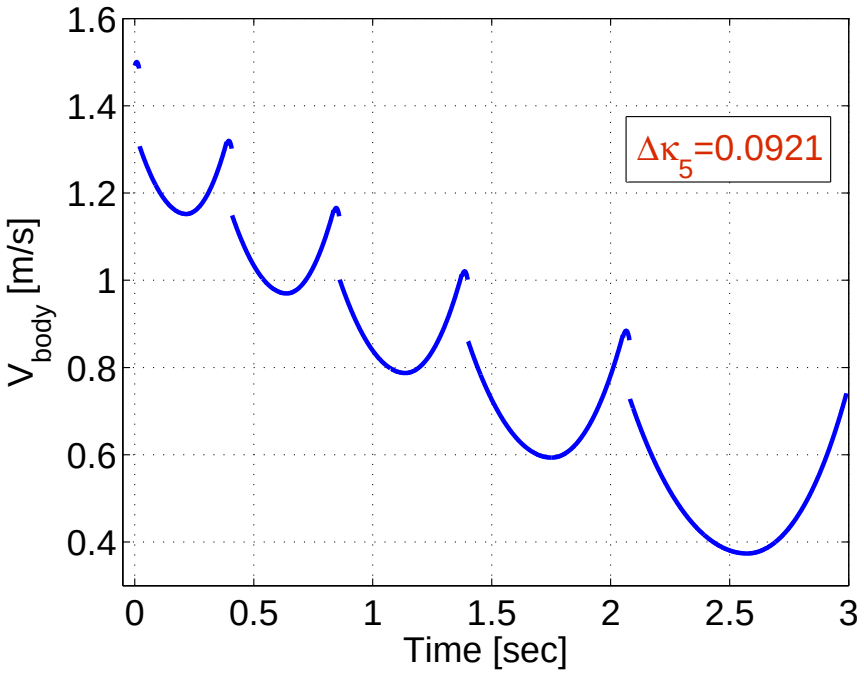

Figure 4.7: Velocity of the COM of the body vs. time during 5 multiple walking steps for poorly-adjusted ($\frac{a}{R} = 15deg$).

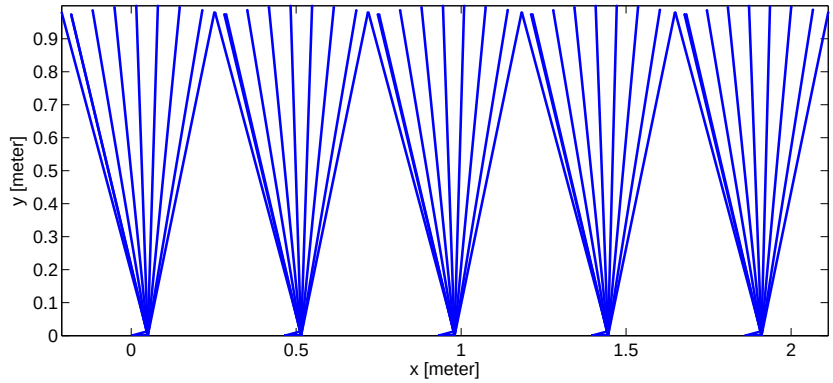

Figure 4.8: Stick diagram of the links of the biped during 5 multiple walking steps for well-adjusted ($\frac{a}{R} = 3.5deg$).

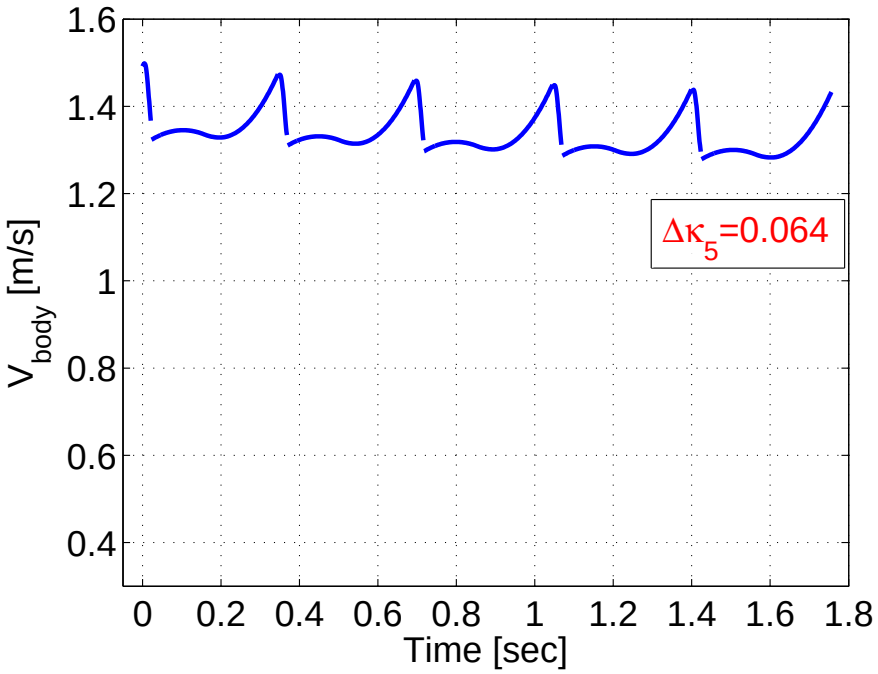

Figure 4.9: Velocity of the COM of the body vs. time during 5 multiple walking steps for well-adjusted ($\frac{a}{R} = 3.5deg$).

Chapter 5

Study of Energy Economy and Design of Controllers

The previous chapter illustrated that properly adjusting the stiffness of OLASAT can significantly reduce the energy loss. I also believe that the adjustment of the stiffness of the tendons as a control strategy can significantly improve the energetics of locomotion in bipedal walking robots. This chapter demonstrates the development of the control methodology of the elastic model of the bipedal walking through the following efforts. Firstly, the energy loss at the foot-touch-down of the bipedal walking model presented in the last chapter is calculated. Based on the provided information, a control strategy based on energy feedback is designed to adaptively adjust the mechanical configuration of OLASAT. Therefore, it adjusts the stiffness of OLASAT to reduce the energy loss during foot-touch-down. Secondly, the detailed development of the speed tracking (ST) controller is provided in this chapter. The ST controller adjusts the stiffness of the trailing leg spring to control the injected energy. It also manipulates the mechanical configuration of OLASAT while energy dissipation is required for reducing the speed. Finally, computer simulations were employed which demonstrates the capability of stiffness adjustment controller and ST controller in reducing the energy loss

and tracking a desired speed of the biped.

The organization of this chapter is as follows. Energy loss during the foot-touch-down is provided in Section 5.1 using the mathematical model of the biped. A controller to automatically adjust the stiffness of OLASAT is proposed in Section 5.2. Section 5.3 provides the detailed development of the speed tracking controller followed by a local stability analysis in Section 5.4. Then in Section 5.5, computer simulations are carried out to demonstrate the performance of the controllers during the single support stance phase.

5.1 Discussion of the energy loss

In chapter 4, the dynamic modeling of the biped during the stance phase was described. The energy loss during the foot-touch-down is one of the major causes of energy reduction in bipedal walking which is reduced by properly adjusting the stiffness of OLASAT. This section studies the key parameters involved in the change in the kinetic energy of the biped, ${}^{FTD}\Delta E = {}^{FTD}E^{-} - {}^{FTD}E^{+}$, before and after the foot-touch-down, shedding light on how the stiffness adjustment of OLASAT can reduce the energy loss. ${}^{FTD}\Delta E$ for the model explained in Figure 4.1 is given below.

$$\begin{aligned} {}^{FTD}\Delta E = 0.5m_2l_2^2(({}^{FTD}\dot{\theta}_2^-)^2 - ({}^{FTD}\dot{\theta}_2^+)^2) + 0.5(m_1d_1^2 + m_2l_1^2)({}^{FTD}\dot{\theta}_1^-)^2 \\ +m_2l_1l_2\cos({}^{FTD}\theta_2)({}^{FTD}\dot{\theta}_1^-)({}^{FTD}\dot{\theta}_2^-) \end{aligned} \tag{5.1}$$

By substituting of ${}^{FTD}\dot{\theta}_2^+$ from Eqn.(4.28) into Eqn.(5.1) and after simplification, the following relation is obtained.

$${}^{FTD}\Delta E = 0.5(m_1d_1^2 + m_2l_1^2\sin^2({}^{FTD}\theta_2^-))({}^{FTD}\dot{\theta}_1^-)^2 \tag{5.2}$$

Masses, lengths of the links and $\sin^2(\ ^{FTD}\theta_2)$ are all positive. Eqn.(5.2) illustrates the direct relation of $^{FTD}\Delta E$ with $(\ ^{FTD}\dot{\theta}_1^-)^2$. It indicates that reducing the magnitude of the angular velocity of the foot immediately before the foot-touch-down can significantly reduce the energy loss of the biped. In addition, Eqn.(4.28) illustrates the direct relation of $^{FTD}\dot{\theta}_2^+ - \ ^{FTD}\dot{\theta}_2^-$ with $^{FTD}\dot{\theta}_1^-$ which indicates that by reducing the magnitude of $^{FTD}\dot{\theta}_1^-$ the change of angular velocity of the stance leg at the foot-touch-down is reduced.

By taking the time derivative of the position of the center of mass (COM) of the body, $^{FTD}Y_{COM}^-$, its velocity is arrived at as given below:

$$^{FTD}\dot{Y}_{COM}^- = l_1\ ^{FTD}\dot{\theta}_1^- + l_2\ ^{FTD}\dot{\theta}_2^- \cos(\ ^{FTD}\theta_2) \tag{5.3}$$

$^{FTD}\dot{\theta}_2^-$ and $\cos(\ ^{FTD}\theta_2)$ are negative before midstance. The optimum situation $^{FTD}\Delta E = 0$ can be achieved by reducing $(\ ^{FTD}\dot{\theta}_1^-)^2$ to zero. In such a scenario, the velocity of the COM of the body at the foot-touch-down will be upward. This indicates that the direction of the velocity vector of the COM of the body at the heel-strike $^{HS}\dot{Y}_{COM}^-$, which is downward, should be reversed to the upward direction at the foot-touch-down during the collision phase to reduce the energy loss. This is made possible by storing part of the kinetic energy of the biped in elastic form during the collision phase. The two elastic elements in this bipedal walking model are the trailing leg spring and OLASAT. These findings serve as the foundation to determine the offset of OLASAT. As a result, the development of an automatic controller to adjust the stiffness of OLASAT is necessary to improve the performance of the bipedal walking which is described in the following section.

5.2 Design of the stiffness adjustment controller

In general, OLASAT has two major roles during the collision phase. The first role is to compensate the moment about the ankle joint exerted by the gravitational force of the body. The second is to store part of the kinetic energy of the biped. Both of these two roles can reduce $({}^{FTD}\dot{\theta}_1^-)^2$. This section provides a guideline for determining the offset of OLASAT, a, in order to store part of the energy of the biped, thus reducing $({}^{FTD}\dot{\theta}_1^-)^2$, and consequently bringing the energy loss down. The development of a controller to satisfy such an optimal condition of $({}^{FTD}\dot{\theta}_1^-)^2 = 0$ can be possible by predicting the dynamics of the bipedal walking in advance. On the other hand, perfectly predicting the dynamics of the biped is not realistic because of the complexity of physical robots. Thus, a controller is developed in this section to estimate the offset of OLASAT without requiring the full knowledge of the system dynamics. To design such a controller, the following assumptions are made in this work.

First, OLASAT is loaded and unloaded passively during the stance phase. Thus for the following walking step, the offset is adjusted during the swing phase of the current walking step while the foot is not in contact with the ground. Second, the feedback signals of the biped are taken to be the angular position, θ_2, and the angular velocity, $\dot{\theta}_2$, of the stance leg. The reason for specifying these two signals as feedback is that the biped is an inverted pendulum during the rebound and the preload phases. Thus, the velocity of the biped at the heel-strike of the following walking step can be determined from the angular velocity of the stance leg at midstance, ${}^{MD}\dot{\theta}_2$. This choice allows enough time to adjust the offset during the swing phase which is important from the practical point of view. Third, the foot is perpendicular to the stance leg immediately before the heel-strike and in such a situation, OLASAT is in the neutral position (with no force). Fourth, the step length is fixed by assuming that the swing leg is perfectly controlled. Fifth, the angular displacement of the stance leg relative to the ground is

negligible during the collision phase. This assumption results in the approximation of ${}^{FTD}\theta_2^- = {}^{HS}\theta_2^-$. It ensures that the total deformation of spring 1 in OLASAT is equal to $R\,{}^{HS}\theta_1^-$. ${}^{HS}\theta_1^-$ and ${}^{HS}\theta_2^-$ are the θ_1 and θ_2 immediately before the heel-strike which are known from the walking step length.

The stiffness adjustment controller developed here determines the offset of OLASAT, a, which corresponds to the angular offset of $\frac{a}{R}$ at the pulley of the ankle joint. Here, the maximum angular displacement of the pulley ($\Delta\vartheta$), in which spring 2 is engaged during the collision phase, is determined first to calculate the offset. Before determining the offset, we first discuss the selection of the stiffness of spring 1 of OLASAT. The stiffness of spring 1 must be selected low enough to prevent the leg from bouncing during the collision phase even for minimum bipedal walking speed while spring 2 is not engaged (minimum stiffness of OLASAT). It must also be selected high enough to compensate a portion of the gravitational moment about the ankle joint at the foot-touch-down and also to store part of the kinetic energy of the biped. Next, we explain the procedure of determining $\Delta\vartheta$.

$\Delta\vartheta(n+1)$ is calculated from the feedback loop of the stiffness adjustment controller for the walking step n+1. Walking step n is started from the heel-strike which includes the double support phase and will end immediately before the heel-strike of the step n+1. The inputs of the stiffness adjustment controller are the angular velocity of the stance leg at midstance, ${}^{MD}\dot{\theta}_2(n)$, of the current walking step n, and the stiffness of the trailing leg spring of the following walking step, $K_t(n+1)$. The output of the stiffness adjustment controller is the offset of OLASAT for the walking step n+1. $K_t(n+1)$ is determined by the speed tracking controller explained in Section 5.3.

Part of the kinetic energy of the biped at the end of the walking step n is stored in the trailing leg spring during the collision phase of the walking step n+1. Based on the results obtained in Section 5.1, the OLASAT should also store part of the kinetic energy during the collision phase of the walking step n+1. Here, the elastic potential

energy, $0.5K_{sp2}R^2(\Delta\vartheta(n+1))^2$, of the walking step n+1 stored in spring 2 is assumed to be proportional to the difference between the kinetic energy of the biped at the end of the walking step n, $0.5m_2(l_2\ {}^{EN}\dot{\theta}_2^-(n)\sin(\varphi_0(n)))^2$, associated with the vertical component of the velocity of the COM of the body, and the elastic potential energy of trailing leg spring, $\frac{1}{2}K_t(\Delta L_{col}^2 - \Delta L_{dss}^2)$, during the collision phase of the walking step n+1 where $\varphi_0(n) = \frac{\pi}{2} -\ {}^{EN}\theta_2^-(n)$. ${}^{EN}\theta_2^-(n)$ and ${}^{EN}\dot{\theta}_2^-(n)$ are the angle and the angular velocity of the stance leg at the end of the preload phase of the walking step n. ΔL_{dss} and ΔL_{col} are the deformation of the tailing leg spring at the heel-strike and the deformation of the tailing leg spring at the foot-touch-down of the walking step n+1. The following equation describes the above energy relation.

$$\frac{1}{2}K_{sp2}R^2(\Delta\vartheta(n+1))^2 = \frac{1}{2}K_{adjust}(m_2(l_2\ {}^{EN}\dot{\theta}_2^-(n)\sin(\varphi_0(n)))^2 - K_t(n+1)(\Delta L_{col}^2 - \Delta L_{dss}^2)) \tag{5.4}$$

K_{adjust} is a proportional gain and $\Delta L_{col} = L_0 -\ {}^{FTD}L_t$, where ${}^{FTD}L_t$ is the length of the trailing leg spring at the foot-touch-down of the walking step n+1 which can be calculated from the kinematics of the biped using the following assumptions. Here, the stiffness of the trailing leg should be limited preventing the right hand side of Eqn.(5.4) from having a negative value. The step length and the initial angles of the foot and the stance leg for the walking step n+1 are known values in this work. Preload is also assumed as a free rotating inverted pendulum under gravity. ${}^{EN}\dot{\theta}_2^-(n)$ can be calculated from the angular velocity of the leg at midstance, ${}^{MD}\dot{\theta}_2(n)$, using the following energy relation:

$$0.5m_2l_2^2({}^{EN}\dot{\theta}_2^-(n))^2 = 0.5m_2l_2^2({}^{MD}\dot{\theta}_2^2(n)) + m_2gl_2(1-\cos(\varphi_0(n))) \tag{5.5}$$

The first term in the right-hand side of the above relation is the kinetic energy of the biped at midstance of the walking step n which is measurable from the feedback

signals. It is assumed that the double support phase is ended before the midstance. Thus the injected energy, through the trailing leg spring during the double support phase of the walking step n, is converted to the kinetic energy of the biped which is measured at the midstance. The second term of the right-hand side of Eqn. (5.5) is the change in the gravitational potential energy of the biped between the midstance of the walking step n and the heel-strike of the walking step n+1 which can be calculated by assuming a fixed amount for the step length. By calculating ${}^{EN}\dot{\theta}_2^-(n)$ from Eqn.(5.5), which results in ${}^{EN}\dot{\theta}_2^-(n) = \sqrt{{}^{MD}\dot{\theta}_2^2(n) + \frac{2g}{l_2}(1-\cos(\varphi_0(n)))}$, and by substituting it into Eqn.(5.4), $\Delta\vartheta(n+1)$ is determined to be as follows.

$$\Delta\vartheta(n+1) = \sqrt{\frac{K_{adjust}}{R^2 K_{sp2}}}\sqrt{m_2(l_2\ {}^{EN}\dot{\theta}_2^-(n)\sin(\varphi_0(n)))^2 - K_t(n+1)(\Delta L_{col}^2 - \Delta L_{dss}^2)} \tag{5.6}$$

Finally, as mentioned above by assuming that the angular movement of the stance leg relative to the ground is negligible during the collision phase, the offset $\frac{a}{R}(n+1)$ is calculated from the relation below.

$$\frac{a}{R}(n+1) = {}^{HS}\theta_1^-(n+1) - \Delta\vartheta(n+1) \tag{5.7}$$

5.3 Design of the speed tracking controller

During stable walking on flat terrain, the limit cycle trajectories of a legged robot can be analyzed using a Poincare map, also known as a return map [114]. This tool has been used extensively in the legged robot literature [38, 115]. For an n-dimensional dynamical system $\dot{x} = f(x)$, a Poincare section S is an n-1 dimensional surface that the system crosses exactly once during each period. By integrating the dynamics forward from one intersection of S to the next, we can describe the discrete return map dynamics of the system as $x_{n+1} = rx_n$ [116]. The advantage of doing this is that the

limit cycle stability of the periodic trajectory in x can now be studied by looking at the fixed point stability of the discrete system in x_n. Although it is rare that we can obtain an analytical form for the return map dynamics, r, here the numerical return map analysis is used. The step-to-step return map [38] is taken at the midstance point. This is a natural configuration of slicing the trajectory because it simplifies the analytical analysis and because it is an event that is easy to measure using position sensor that is installed at the ankle joint of the biped. For the bipedal walking model proposed in the previous chapter, the states of the system after the collision phase are the angle, θ_2, and the angular velocity, $\dot{\theta}_2$, of the stance leg. However, the angle is fixed at midstance. Thus, regulating the velocity or the kinetic energy of the biped at midstance provides a stable limit cycle. Velocity regulation or speed tracking (ST) of the proposed bipedal walking model, including the adaptive stiffness adjustment controller, is a challenging problem which is discussed in this section. The ST controller adjusts the stiffness of the trailing leg spring to regulate the velocity of the biped at midstance during consecutive walking steps. This stiffness adjustment can be done by developing the compliant control on the actuator systems in the trailing leg. In addition, the effects of elasticity in the actuation system and other artificial tendons in the robot should be considered. However in the thesis, the implementation details of the stiffness adjustment of the trailing leg are not covered. The input of the ST controller is the biped velocity error at midstance in the current walking step and the output of the controller is the stiffness of the trailing leg spring for the next walking step. As a result, the ST controller is an event-based and time-independent controller. The walking step n is started from the heel-strike which includes the double support phase. The walking step n will be ended immediately before the heel-strike of the step n+1. In this section the background of developing such a controller is explained first. Then, the detailed form of the ST controller is described.

As mentioned before, potential elastic energy in the trailing leg during the double

support phase is the major source of energy input to the biped. Since the mechanical energy of the biped is suddenly changed in each walking step during the collision phase (heel-strike and foot-touch-down), a force from compliant trailing leg (assumed as a massless pre-compressed compressional linear spring) is applied on the COM of the body to inject the energy to the biped for regulating the kinetic energy of the biped at midstance which regulates the velocity at midstance through direct correlation. Geometric progression is used to regulate the kinetic energy of the biped at midstance, ${}^{MD}E$, to the desired one, ${}^{MD}E_d$. The n+1 term of this geometric sequence, ${}^{MD}E(n+1)$, with the initial value of ${}^{MD}E(n)$ and the common ratio of μ_k for every walking step $n > 2$ is given by:

$$ {}^{MD}E(n+1) = \mu_k \, {}^{MD}E(n) + (1-\mu_k) \, {}^{MD}E_d \tag{5.8}$$

The behavior of the above geometric sequence depends on the value of the common ratio. If the common ratio is positive and less than 1, there will be exponential decay towards ${}^{MD}E_d$. In such a scenario, the required kinetic energy change of the biped in walking step n+1, ΔE_r, is given below by substituting ${}^{MD}E(n+1)$ from Eqn.(5.8) in $\Delta E_r = {}^{MD}E(n+1) - {}^{MD}E(n)$.

$$ \Delta E_r = (\mu_k - 1)(\, {}^{MD}E(n) - \, {}^{MD}E_d) \tag{5.9}$$

The actual kinetic energy change of the biped in one step, $\Delta E_a = E^{inj}(n+1) - E^{diss}(n+1)$, equals the summation of the total injected energy, $E^{inj}(n+1)$, and the total dissipated energy, $E^{diss}(n+1)$, of the biped during the walking step n+1 from the heel-strike to the midstance. $E^{inj}(n+1)$ equals the summation of the elastic energy from the trailing leg spring, $E_t^{inj}(n+1) = \frac{1}{2}K_t(n+1)(\Delta L_{dss})^2$, and the gravitational

potential energy of the foot, $E_g^{inj}(n+1) = m_1 g d_1 \sin({}^{HS}\theta_1)$, which is given below.

$$E^{inj}(n+1) = \frac{1}{2}K_t(n+1)(\Delta L_{dss})^2 + m_1 g d_1 \sin({}^{HS}\theta_1) \tag{5.10}$$

where $K_t(n+1)$ and ΔL_{dss} are the stiffness and the initial deformation of the trailing leg spring in walking step n+1. ΔL_{dss} is calculated from the kinematics of the biped preceding the heel-strike. To regulate the kinetic energy of the biped at the midstance, the actual kinetic energy change of the biped should be equal to the required one which correspons to $\Delta E_a = \Delta E_r$ and results in the following equation.

$$E^{inj}(n+1) - E^{dis}(n+1) = (\mu_k - 1)({}^{MD}E(n) - {}^{MD}E_d) \tag{5.11}$$

By replacing the injected energy, $E^{inj}(n+1)$ formulated in Eqn.(5.10), in the energy relation of Eqn.(5.11), the following relation is obtained:

$$\frac{1}{2}K_t(n+1)(\Delta L_{dss})^2 + m_1 g d_1 \sin({}^{HS}\theta_1) = E^{diss}(n+1) + (\mu_k - 1)\,{}^{MD}(E(n) - E_d) \tag{5.12}$$

in which

$${}^{MD}E(n) - {}^{MD}E_d = \frac{1}{2}m_2 l_2^2({}^{MD}\dot{\theta}_2^2(n) - {}^{MD}\dot{\theta}_{2d}^2) \tag{5.13}$$

where $l_2\ {}^{MD}\dot{\theta}_2$ and $l_2\ {}^{MD}\dot{\theta}_{2d}$ are the actual and desired velocity of the biped at midstance. By substituting ${}^{MD}E(n) - {}^{MD}E_d$ from Eqn.(5.13) into Eqn.(5.12), we have:

$$\begin{aligned} \frac{1}{2}K_t(n+1)(\Delta L_{dss})^2 &= E^{diss}(n+1) - m_1 g d_1 \sin({}^{HS}\theta_1) \\ &+ \frac{1}{2}m_2 l_2^2(\mu_k - 1)\,{}^{MD}(\dot{\theta}^2(n) - \dot{\theta}_{2d}^2) \end{aligned} \tag{5.14}$$

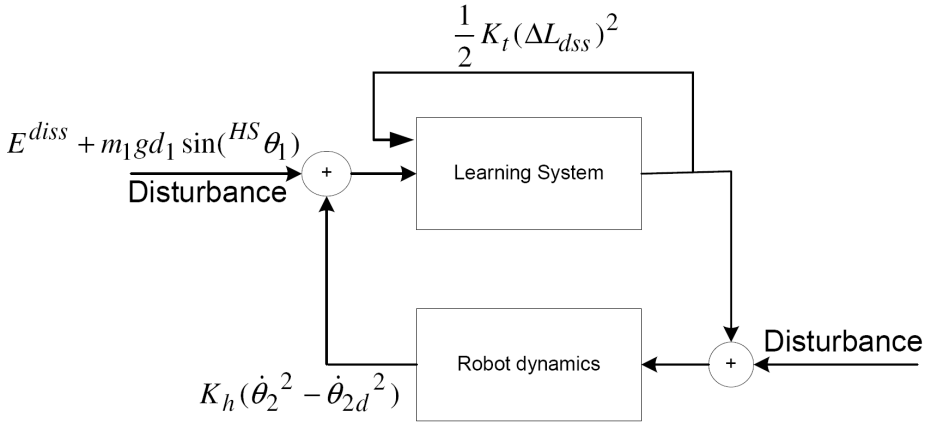

Figure 5.1: Schematic diagram of the speed tracking controller.

The required elastic potential energy, $\frac{1}{2}K_t(n+1)(\Delta L_{dss})^2$, for regulating the kinetic energy of the biped can be calculated from Eqn.(5.14) in which, the dissipated energy, $E^{diss}(n+1)$, the foot initial angle at the heel-strike, ${}^{HS}\theta_1$, and the angular velocity of the stance leg at midstance should be known. In this work, it is considered that the initial deformation of the trailing leg spring, ΔL_{dss}, to be constant and the elastic potential energy can be adjusted by changing the stiffness of the trailing leg spring, K_t. Since random perturbations exist in the leg and the foot initial angles, $E^{diss}(n+1)$ and ${}^{MD}\dot{\theta}_2$ can not be predicted accurately. However, the lack of accurate prediction is also influenced by adjusting the stiffness of OLASAT. Thus, designing a controller based on Eqn.(5.14), with the objective of regulating the kinetic energy at midstance by adjusting K_t, is a challenging problem which is explained below.

In this work, the controller (shown in Figure 5.1) is designed as a reinforcement learning system in which the above energy relation in Eqn.(5.14) is used. By weighing the resulting feedback signal, ${}^{MD}\dot{\theta}_2^2(n) - {}^{MD}\dot{\theta}_{2d}^2$, against the perturbation applied, $E^{diss}(n+1) - m_1 g d_1 \sin({}^{HS}\theta_1)$, the controller can effectively tune the system to fulfill the control objective. As shown in Figure 5.1, a learning system is assumed to have

the following relationship:

$$\frac{1}{2}K_t(n+1)(\Delta L_{dss})^2 = \frac{1}{2}K_t(n)(\Delta L_{dss})^2 + K_h\ {}^{MD}(\dot{\theta}_2^2(n) - \dot{\theta}_{2d}^2) \tag{5.15}$$

which is similar to Eqn.(5.14) by assuming two things. Firstly, the injected energy through the trailing leg, $\frac{1}{2}K_t(n+1)(\Delta L_{dss})^2$, eliminates the energy disturbance terms of $E^{diss}(n+1) - m_1 g d_1 \sin({}^{HS}\theta_1)$. Secondly, the variation in the injected energy in each walking step, $\frac{1}{2}(K_t(n+1) - K_t(n))(\Delta L_{dss})^2$, is proportional to the square of the velocity error with the gain $K_h = \frac{1}{2}m_2 l_2^2(\mu_k - 1)$. $K_t(n+1)$ is determined from the learning system which is set to be always positive. $\nu(n+1)$ is the dimensionless parameter of the stiffness of the trailing leg in step n+1 which is computed from $K_t(n+1)$ and is equal to $\frac{K_t(n+1)l_2}{m_2 g}$ as listed in Table 5.1.

Using this method, $\nu(n+1)$ is updated from its value in the previous walking step $\nu(n)$. By adjusting the trailing leg stiffness using Eqn.(5.15) and Eqn.(5.16), the injected energy to the system can be controlled to accelerate the biped.

The above ST controller can only inject the energy to the biped. However, it decreases the stiffness value of the trailing leg spring while the desired speed is lower than the actual one. In addition, the automated stiffness adjustment controller adjusts the offset of OLASAT to reduce the energy loss. Thus, the remaining way to reduce the speed of the biped is to naturally dissipate part of the energy of the biped during the collision phase and this is possible by re-tuning the offset $\frac{a}{R}(n)$ resulted from Eqn.(5.7). The following equation shows the offset re-tunning method.

$$\frac{a}{R}(n+1) = \begin{cases} \frac{a}{R}(n+1) + K_o E_v & 0 > E_v \\ \frac{a}{R}(n+1) & 0 \leq E_v \end{cases} \tag{5.16}$$

where E_v is the error in the square of the angular velocity of the stance leg at midstance and equals ${}^{MD}\dot{\theta}_2^2(n) - {}^{MD}\dot{\theta}_{2d}^2$. K_o is the gain of the offset re-tuning controller. In

this method, the energy is dissipated by poorly adjusting the stiffness of OLASAT. By considering the existence of spring 1 in OLASAT, the collision phase is still compliant and the impulsive force at the foot-touch-down remains lower than the force at the rigid impact. The next section explains the local stability analysis of the biped.

5.4 Local stability analysis

The local stability of the passive walkers is traditionally quantified by examining the eigenvalues of the linearized step-to-step return map ([38, 116]), taken around a point in the period either preceding or immediately following the collision. Return of a perturbed state variable to a limit cycle can be mapped discretely from cycle to cycle at the same phase. Mapping all possible perturbations from one cycle to the next produces a return map. A linearized version of the mapping function can yield quantitative measures of stability for a local region. The percentage of the perturbation remaining after each cycle is given by the eigenvalue. Eigenvalues closer to zero indicate a more rapid rate of recovery, whereas values closer to one indicate a slower rate of recovery. A stability value (eigenvalue) of 0.3 means that only 30% of the perturbation remains after a single cycle. In the next cycle, the remaining perturbation is reduced again by 30%, so that only 9% is left. Reducing the perturbation by a constant percentage after each cycle results in asymptotic recovery. While in this work the velocity is regulated at midstance, a position sensor can detect the upright position and the motion of the biped. The biped is an inverted pendulum preceding or following the midstance. The return map of this analysis is evaluated through the $\theta_2 = \frac{\pi}{2}$ when $\dot{\theta}_2 > 0$.

The state of the bipedal walking model is described by 2 variables (θ_2, $\dot{\theta}_2$), therefore the return map has dimension 1. To evaluate the eigenvalues of the return map of the biped in consecutive walking, ${}^{MD}\dot{\theta}_2^n$ is created which represents $\dot{\theta}_2$ at midstance on the n^{th} walking step. For the velocity regulation, the equilibrium of the return map is ${}^{MD}\dot{\theta}_{2d}$. Finally, a least squares fit of the matrix A to satisfy the following relation can

be performed.

$$({}^{MD}\dot{\theta}_2^{n+1} - {}^{MD}\dot{\theta}_{2d}) = A \, ({}^{MD}\dot{\theta}_2^{n} - {}^{MD}\dot{\theta}_{2d})$$

This was accomplished by accumulating the data from all walking steps into matrices

$$X = [{}^{MD}\dot{\theta}_2^{1} - {}^{MD}\dot{\theta}_{2d}, \; {}^{MD}\dot{\theta}_2^{2} - {}^{MD}\dot{\theta}_{2d}, ..., \; {}^{MD}\dot{\theta}_2^{n} - {}^{MD}\dot{\theta}_{2d}, ...] \tag{5.17}$$
$$Y = [{}^{MD}\dot{\theta}_2^{2} - {}^{MD}\dot{\theta}_{2d}, \; {}^{MD}\dot{\theta}_2^{3} - {}^{MD}\dot{\theta}_{2d}, ..., \; {}^{MD}\dot{\theta}_2^{n+1} - {}^{MD}\dot{\theta}_{2d}, ...]$$

and computing

$$A = YX^T(XX^T)^{-1} \tag{5.18}$$

The eigenvalues of A give the linear approximation of the return map eigenvalues. The next section shows the simulation results illustrating the performance of the controllers to regulate the velocity of the biped.

5.5 The study of energetics through simulations

The performance of the stiffness adjustment controller developed in Section 5.2 and the ST controller implemented in Section 5.3 are illustrated in this section through computer simulations.

5.5.1 Bipedal walking simulation with stiffness adjustment controller

In this section the performance capabilities of an automated stiffness adjustment controller, explained in Section 5.2, are discussed. The initial conditions of the biped are the same as case 1 in Section 4.4.1. In order to simulate the poorly-adjusted stiffness, $\frac{a}{R}$ is assumed to be 15^o in the first walking step. This is equivalent to a single

spring. Here, the stiffness of spring 1 in OLASAT is defined through trial and error. The objective was to find a stiffness which prevents the leg bouncing at the FTD for different initial velocities, and which is high enough to store the elastic energy during the collision phase. This results in increasing the stiffness of spring 1 from $\varsigma = 0.3$ (in previous sections) to $\varsigma = 0.5$. The proportional gain of the automated stiffness adjustment controller, K_{adjust}, can play an important role in optimally adjusting the offset. Optimal iteration procedure to obtain the best gain remains as future research. Through trial and error simulations, it has been observed that adaptive adjusting of K_{adjust}, as a function of the angular velocity of the stance leg at midstance, provides a better performance of the controller. Thus, in the simulation results of this section, the relation $K_{adjust} = 3l_2^{MD}\dot{\theta}_2$ is assumed. The simulation results of the biped in 5 consecutive walking steps using the automated stiffness adjustment controller are shown in Figures 5.2 and 5.3. The motion of the biped is sustained as shown in the stick diagram of the biped (Figure 5.2). The first walking step shows a sudden jump in the velocity of the COM of the body, shown in Figure 5.3. The controller is activated after the first walking step by sensing the angular velocity of the stance leg at midstance. As shown in Figure 5.3, the sudden change in the velocity of the COM of the body is significantly reduced after the first walking step. The energy loss is also significantly reduced, $\Delta\kappa = 0.074$, compared to case 1 in Section 4.4.2.

5.5.2 Simulation results and discussions of speed tracking controller

The bipedal walking studied here is regulated by the adaptive stiffness adjustment controller (Eqn.(5.7) of Section 5.1) and the ST controller (Eqn.(5.15) of Section 5.3) followed by the offset of OLASAT being adjusted by a retuning controller. The goal of this section is to demonstrate the performance of the controllers in tracking a desired

Table 5.1: Parameters used in the simulations.

Parameters	β	ψ	ζ	υ	ς	η	ϵ
Value	0.02	0.05	0.07	0.1	0.3	4	0.05

speed during consecutive walking steps on a level ground.

Parameters of the biped used in the computer simulations are listed in Table 5.1. $m_2 = 1\ kg$ and $l_2 = 1.0\ m$. The initial conditions of the biped immediately before the heel-strike of the first walking step in the simulations are specified as follows. ${}^{HS}\theta_1^- = 15^o$, ${}^{HS}\theta_2^- = 105^o$, $x_h = y_h = 0$, ${}^{HS}\dot{\theta}_1^- = {}^{HS}\dot{\theta}_2^- = 0$, and $\varphi_0 = 11.7^o$. Note that an actively controlled swing leg is assumed during the single support phase to provide a constant step length without any dynamical effects on the biped. In the simulations $K_h = 1$, $K_o = 20$ and the initial value of $\nu(1)$ is equal to 5. The proportional gain of the adaptive stiffness adjustment controller, K_{adjust}, can play an important role in optimally adjusting the offset. The optimal iteration procedure to obtain the best gain remains as future research. Through trial and error simulations, it has been observed that adaptive adjusting of K_{adjust}, as a function of the angular velocity of the stance leg preceding the heel-strike, improves the performance of the controller in reducing the energy loss.

Simulation results are presented in this section for 4 cases. Case 1 shows the performance of the ST controller during acceleration while the desired velocity is larger than the initial velocity. In contrast, case 2 simulates the response of the system (biped+controllers) during deceleration while the desired velocity is lower than the initial one. In order to simulate the response of the system to disturbances, case 3 includes disturbance in the initial angle of the foot and of the stance leg of the following walking step. In case 4, the response of the biped to different desired velocities is observed through simulation. Then the local stability is studied by calculating the linear approximation of the return map eigenvalues.

Figures 5.4 and 5.5 show the simulation results of case 1. The initial velocity of the biped at the heel-strike of the first walking step is equal to 1 $\frac{m}{sec}$ and the initial value of $\nu(1)$ is equal to 5. The desired velocity at midstance, $l_2\ {}^{MD}\dot{\theta}_{2d}$, is equal to 1.5 $\frac{m}{s}$. K_{adjust} is assumed to be equal to 4 $l_2\ {}^{EN}\dot{\theta}_2$. The velocity of the upper end of the stance leg (the body) is shown in Figure 5.4 for the time period of 50 consecutive walking steps. It has been shown that the velocity of the body rapidly approaches the desired value. To gain insight of how the group of controllers (the stiffness adjustment controler, the ST controller, and the re-tuning controller) perform, Figures 5.5a, 5.5b, and 5.5c illustrate the velocity of the body at midstance ($l_2\ {}^{MD}\dot{\theta}_2$), the dimensionless value of the stiffness of the trailing leg spring (ν) and the offset of OLASAT ($\frac{a}{R}$), respectively. The horizontal axis of Figure 5.5 indicate the walking step number. There are two dash lines in Figure 5.5. Line A defines the walking step number in which the velocity of the biped at midstance reaches the desired velocity for the first time. Line B defines the step number after which the velocity of the biped at midstance remains steady state. The biped accelerates in a period of first step to line A, as shown in Figure 5.5a. In this period the ST controller increases ν to inject more energy in each walking step, as shown in Figure 5.5b. By increasing the velocity of the biped, as shown in Figure 5.5c, the offset is reduced to store more energy in OLASAT during the collision phase. From line A to B, the actual velocity is decreased and approaches the desired one caused by a decrease in ν, as shown in Figure 5.5b. This happens because less energy is required to keep the velocity constant compared to the energy requirements during the acceleration period. The discontinuity of the velocity of the body, shown in Figure 5.4, is caused by the impact of the foot-touch-down. The upper limit and the lower limit of the velocity of the body are shown with two lines in Figure 5.4. These two lines approach one another in each walking steps. This is caused by reducing the energy loss during the collision phase. This energy loss reduction is also brought about by reducing the offset in OLASAT (shown in Figure 5.5c). Reducing

the offset in OLASAT is also caused by reducing ν. As shown in Eqn.(5.6), the effects of $K_t(n+1)(\Delta L_{col}^2 - \Delta L_{dss}^2)$ term is reduced by decreasing the stiffness of the trailing leg spring. These effects are caused by coupling the stiffness adjustment controller and the ST controller through the stiffness of the trailing leg spring. In general, the results of case 1 illustrate the good performance of the group of controllers in regulating the velocity and in reducing the energy loss.

Figures 5.6 and 5.7 show the simulation results of case 2. The initial velocity of the biped at the first step is equal to 1.8 $\frac{m}{sec}$. The desired velocity at midstance, $l_2\ ^{MD}\dot{\theta}_{2d}$, is equal to 1 $\frac{m}{s}$. K_{adjust} is set to 4 $l_2\ ^{EN}\dot{\theta}_2$. The velocity of the body in 50 consequtive walking steps is shown in Figure 5.6. It has been shown that the velocity of the body approaches the desired value through a rapid deceleration. Figures 5.7a, 5.7b, and 5.7c illustrate the velocity of the body at midstance, the dimensionless value of the stiffness of the trailing leg, and the offset of OLASAT for 50 consecutive walking steps. Line A, in Figure 5.7, defines a step number in which the actual velocity of the body reaches the desired velocity and remains steady state. The biped decelerates rapidly from the first walking step to line A, as shown in Figure 5.7a. In this period, ν is rapidly decreased (as shown in Figure 5.7b) to reduce the injected energy during the double support phase. To decrease the velocity of the biped, as shown in Figure 5.7c, the offset is retuned to be higher. As can be seen in Figures 5.7b and 5.7c, the value of ν and the offset approach constant values after line A. In general, the results of case 2 illustrate the reasonable performance of the group of controllers during deceleration and speed regulation.

Figures 5.8 and 5.9 show the simulation results of case 3. In this case, to test the robustness of the controllers, an angular disturbance of $\pm 3^o$ is added in the foot and the leg initial angles which results in $^{HS}\theta_1 = 15^o \pm 3^o$ and $^{HS}\theta_2 = 105^o \pm 3^o$. Here, the initial velocity of the biped at the first walking step is equal to 1 $\frac{m}{sec}$. The desired velocity at midstance, $l_2\ ^{MD}\dot{\theta}_{2d}$, is equal to 1.8 $\frac{m}{s}$. K_{adjust} is assumed to be equal to

$3\ l_2\ {}^{EN}\dot{\theta}_2$ to prevent bouncing caused by disturbance effects. The velocity of the body is shown in Figure 5.8 in the time period of 50 consecutive walking steps. It has been shown that the velocity of the body rapidly approaches the desired value even in the presence of the disturbances. The discontinuity in the velocity of the body is caused by the impact events and the disturbances. Figures 5.9a, 5.9b, and 5.9c illustrate the velocity of the body at midstance, dimensionless value of the stiffness of the trailing leg, and the offset of OLASAT for 50 consecutive walking steps. Two qualitative lines of A and B are placed in Figure 5.9. Line A defines a walking step number in which the actual velocity is very close to the desired velocity. Line B defines the median of the actual velocity during the 50 walking steps which is very close to the desired one. The biped accelerates from the first walking step to line A, as shown in Figure 5.9a. In this period in order to inject more energy, ν is increased in each walking step as shown in Figure 5.9b. By increasing the velocity of the biped (as shown in Figure 5.9c), the offset is reduced to store more energy in OLASAT during the collision phase. After line A, the decrease in ν causes the decrease of the actual velocity, as shown in Figure 5.9b. This happens because less energy is required to keep the velocity constant compared to the energy requirements during the acceleration period. In this period (as shown in Figure 5.9c), the offset is tuned close to 6^o to reduce the energy loss during the collision phase. As can be seen in Figures 5.9b and 5.9c, the values of ν and offset approach constant values as well. In general, the results of case 3 illustrate that the controller's composition are robust with respect to the disturbances in the initial angle of the foot and the stance leg.

In case 4, Figure 5.10 illustrates the simulation results of the biped for different desired velocity values. The initial velocity of the biped at the heel-strike of the first walking step is equal to 1 $\frac{m}{sec}$. Different desired velocities at midstance, $l_2\ {}^{MD}\dot{\theta}_{2d}$, are 0.6 $\frac{m}{s}$, 0.8 $\frac{m}{s}$, 1 $\frac{m}{s}$, 1.2 $\frac{m}{s}$, 1.4 $\frac{m}{s}$, 1.6 $\frac{m}{s}$, and 1.8 $\frac{m}{s}$. K_{adjust} is assumed to be equal to $4\ l_2\ {}^{EN}\dot{\theta}_2$. In the simulations, $K_h = 1$, and the initial value of ν is equal to 1 for all

of the desired velocities. K_o in cases 1 to 3 was equal to 20 which is set to 50 here to reduce the steady state error of velocity. The horizontal axis of Figure 5.10 indicates the walking step number. Figures 5.10a, 5.10b, and 5.10c illustrate the velocity of the body at midstance, the dimensionless value of the stiffness of the trailing leg spring, and the offset of OLASAT respectively. The results show that the speed of the biped is successfully regulated in the desired velocity, as shown in Figure 5.10a. A comparison of the results of Figures 5.10a and 5.10b illustrates that the steady state value of the trailing leg spring stiffness is increased at higher speeds of the biped. This indicates that more energy is required to regulate the higher speeds. Comparing the results of Figures 5.10a and 5.10c shows that by increasing the speed of the biped, the offset of OLASAT is reduced. By reducing the offset more energy is stored in OLASAT during the stance phase. After 50 consecutive walking steps the linear approximation of the return map has the following eigenvalues: 0.6615, 0.8844, 0.8996, 0.8946, 0.8948, 0.8901, 0.8851 corresponding to the desired velocities of 0.6 $\frac{m}{s}$, 0.8 $\frac{m}{s}$, 1 $\frac{m}{s}$, 1.2 $\frac{m}{s}$, 1.4 $\frac{m}{s}$, 1.6 $\frac{m}{s}$, and 1.8 $\frac{m}{s}$. The largest eigenvalue of 0.8996 indicates that the system is locally stable. In general, these results illustrate the good performance of the group of controllers in regulating the velocity as well as in reducing the energy loss.

5.6 Summary

This chapter addressed the energy economy and control aspects of bipedal walking model composed of adjustable stiffness elasticity. A simple controller based on energy feedback was designed to automatically adjust the mechanical configuration of OLASAT. Therefore, it adjusts the stiffness of OLASAT to reduce the energy loss during the foot-touch-down. An event-based time-independent controller was developed, based on geometric progression with exponential decay in kinetic energy error, to adjust the stiffness of the trailing-leg spring. This controls the energy injected to the biped in tracking a desired speed at midstance. A re-tuning controller was also

integrated with the speed tracking controller to tune the stiffness of OLASAT. The local stability of the system composed of a group of controllers is studied by eigenvalues of the linear approximation of the return map. Simulation results show that the combination of controllers is successful in tracking a desired speed even in the presence of the disturbances in the leg's initial angles. The results of the local stability analysis also show that the largest eigenvalue is smaller than one, which testifies to the local stability of the system.

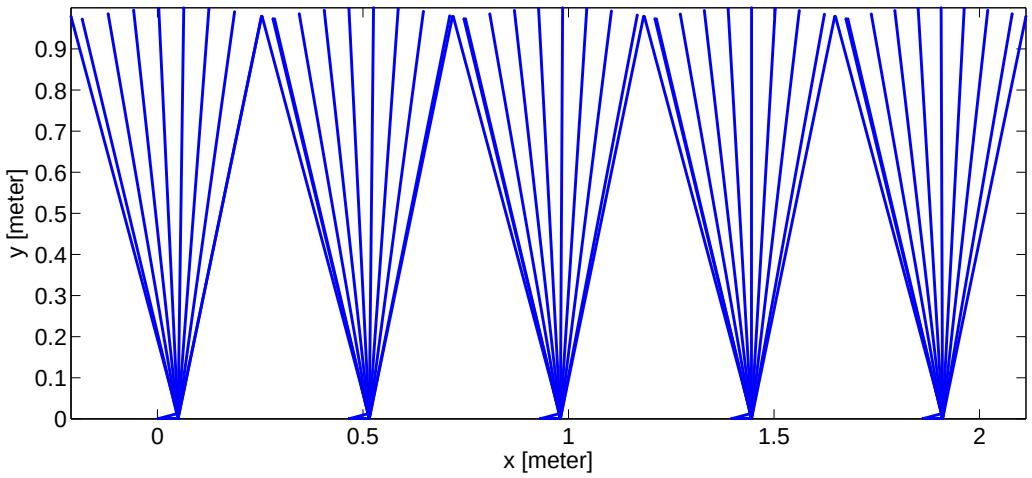

Figure 5.2: Stick diagram of the links of the biped during 5 multiple walking steps with active stiffness adjustment controller.

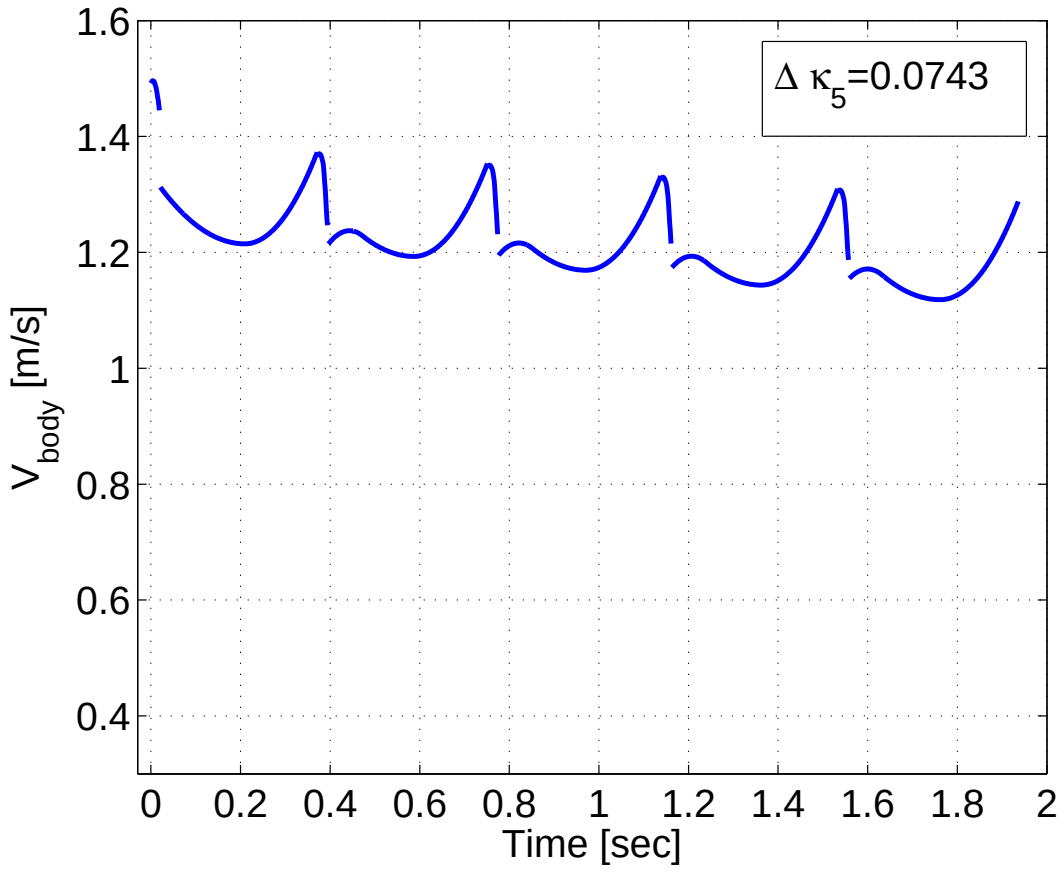

Figure 5.3: Velocity of the COM of the body vs time during 5 multiple walking steps with active stiffness adjustment controller.

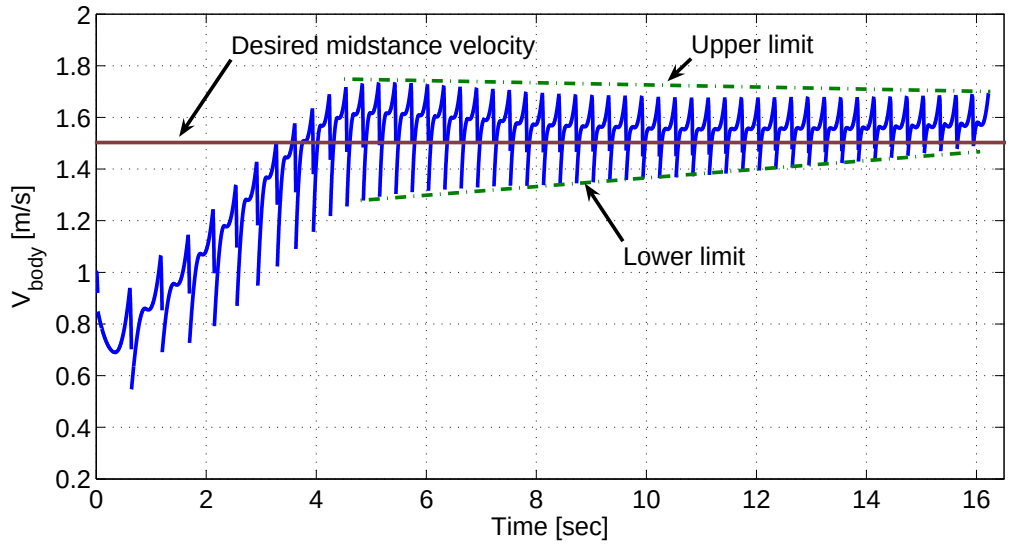

Figure 5.4: Velocity of the body. Desired velocity is 1.5 $\frac{m}{sec}$.

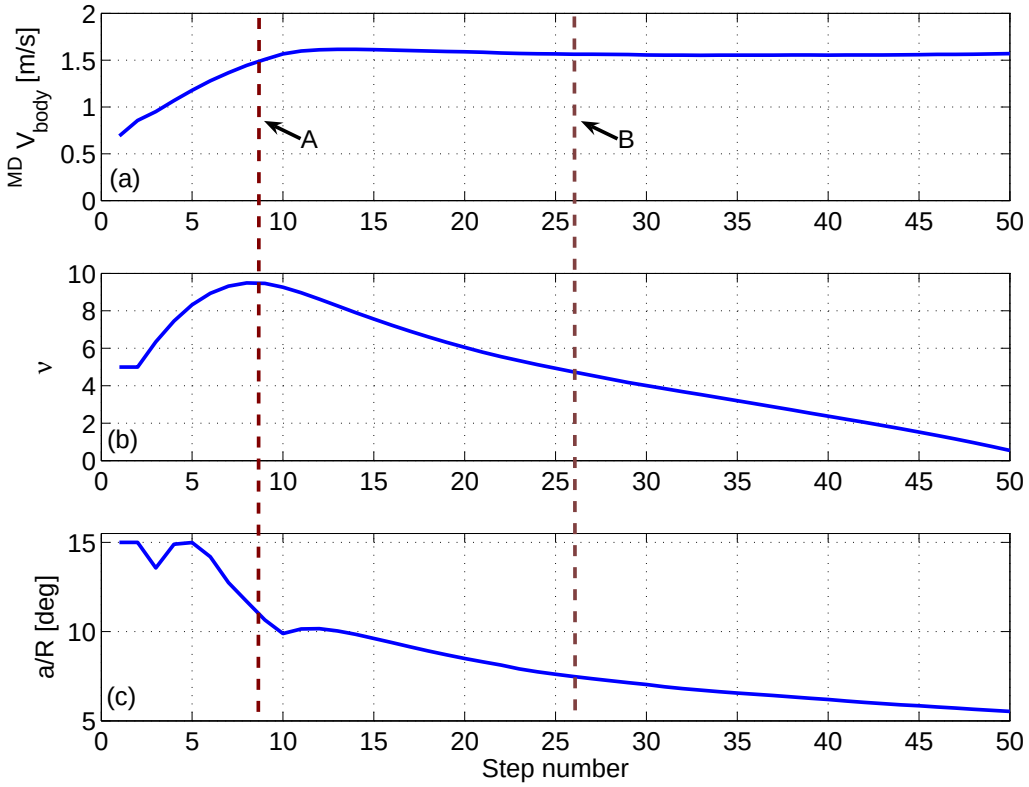

Figure 5.5: Results of the simulation during 50 walking steps. Desired velocity is 1.5 $\frac{m}{sec}$. (a)- Velocity of the body at Midsance. (b)- Stiffness of the trailing leg. (c)- Offset of the springs in OLASAT.

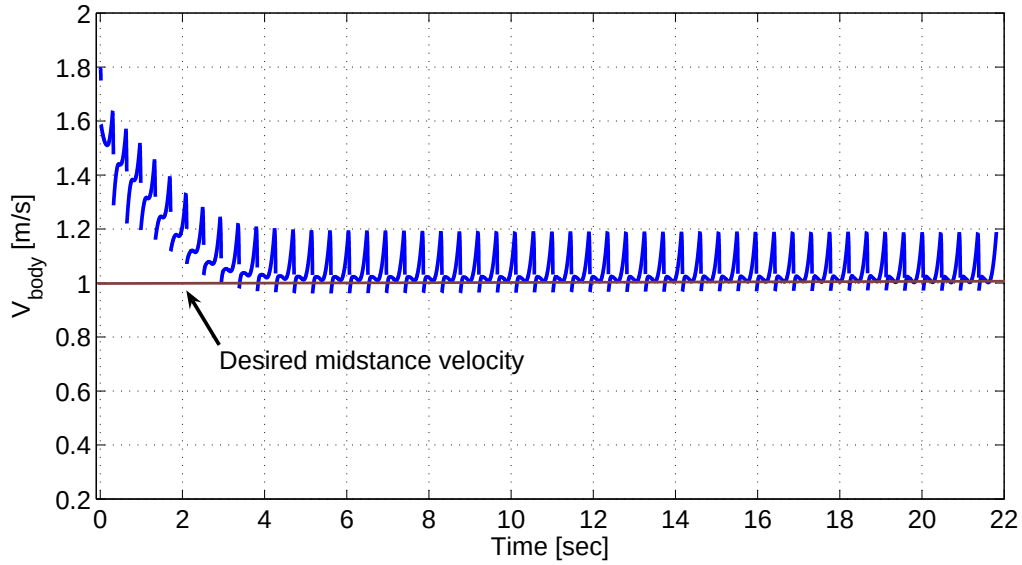

Figure 5.6: Velocity of the body. Desired velocity is 1 $\frac{m}{sec}$

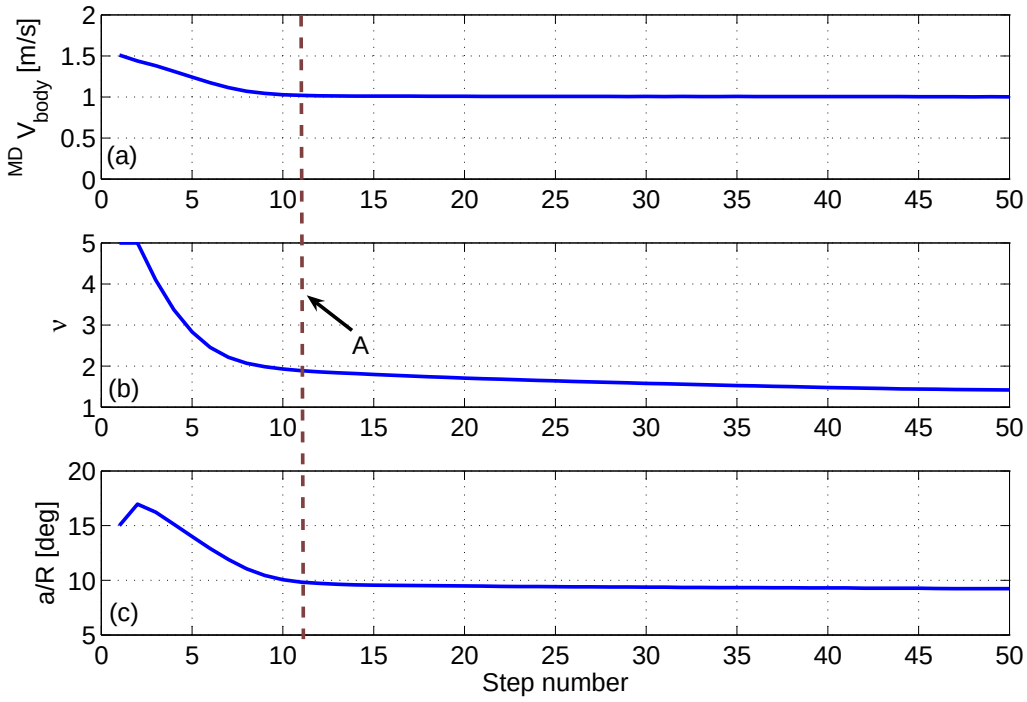

Figure 5.7: Results of the simulation during 50 walking steps. Desired velocity is 1.0 $\frac{m}{sec}$. (a)- Velocity of the body at Midsance. (b)- Stiffness of the trailing leg. (c)- Offset of the springs in OLASAT.

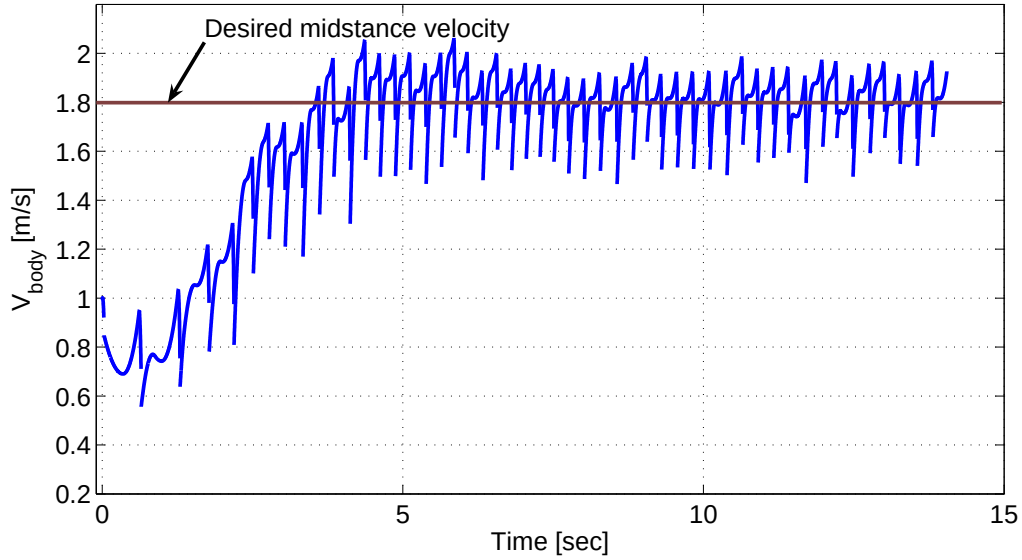

Figure 5.8: Velocity of the body including the disturbances. Desired velocity is 1.8 $\frac{m}{sec}$.

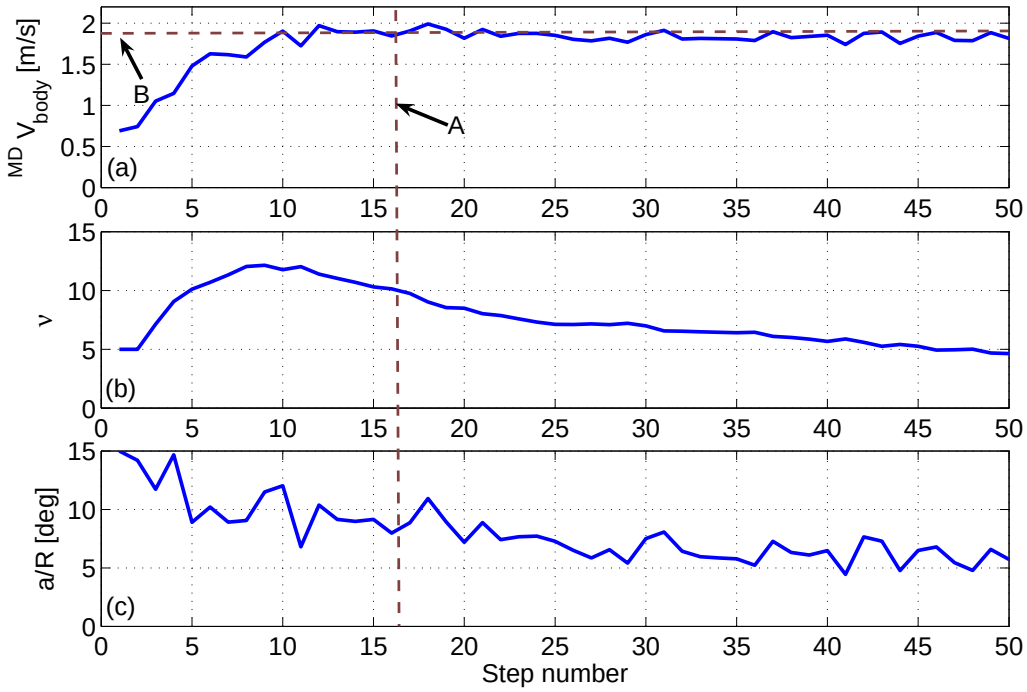

Figure 5.9: Results of the simulation during 50 walking steps including the disturbances. Desired velocity is 1.8 $\frac{m}{sec}$. (a)- Velocity of the body at Midsance. (b)- Stiffness of the trailing leg. (c)- Offset of the springs in OLASAT.

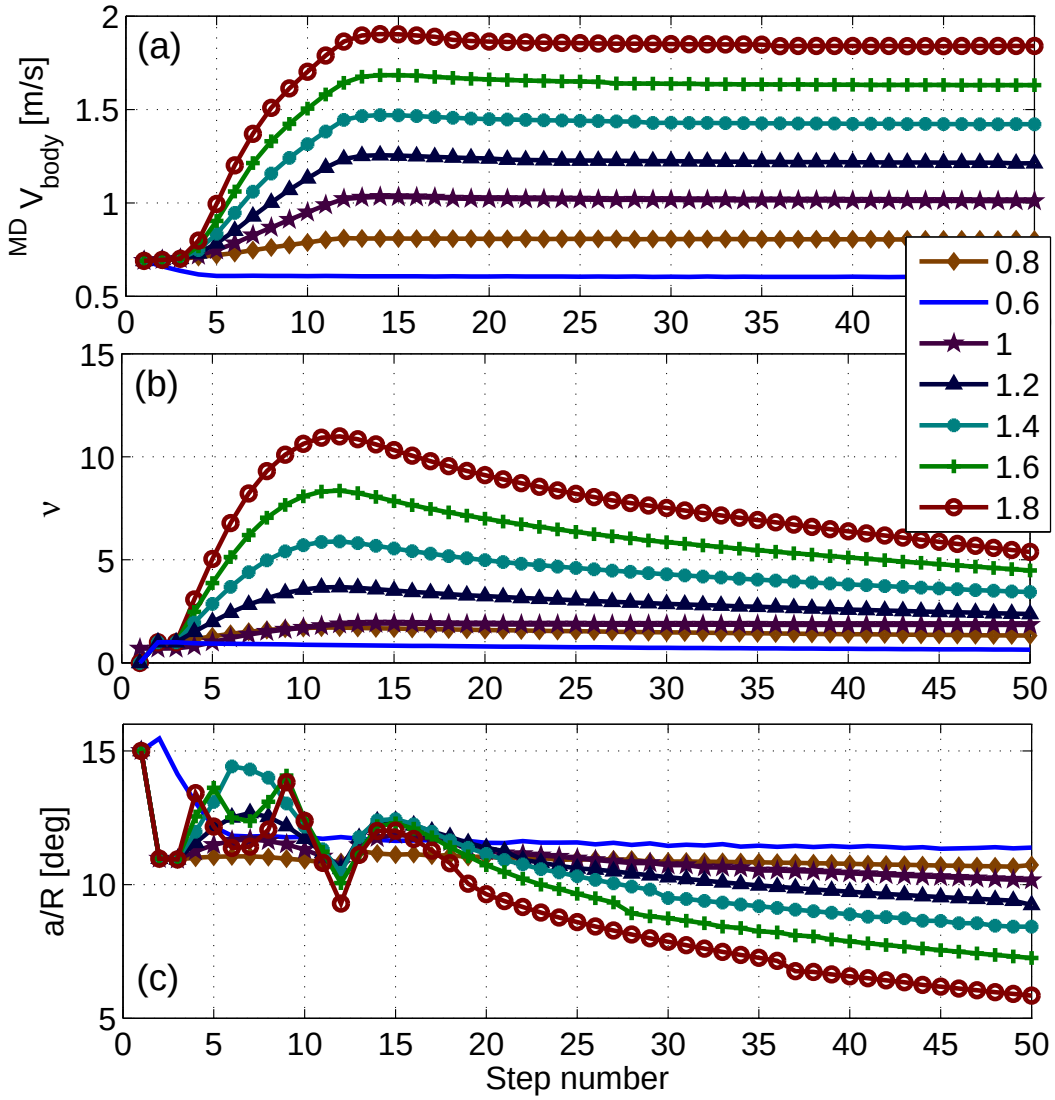

Figure 5.10: Results of the simulation during 50 walking steps for desired velocities from 0.6 to 1.8 $\frac{m}{sec}$ with steps of 0.2 $\frac{m}{sec}$. (a)- Velocity of the body at midsance. (b)- Stiffness of the trailing leg. (c)- Offset of the springs in OLASAT.

Chapter 6

Conclusions and Outline of Future Work

6.1 Conclusions

The conclusions of the thesis are summarized here.

1. Conceptual design of an automated adjustable stiffness coupling (AASC) with the ability to adjust its stiffness over a wide range was introduced. Then, Adjustable Compliant Series Elastic Actuator (ACSEA) was developed by adding AASC between a geared electromagnetic actuator and the load. A new force control method for ACSEA was developed by using the velocity control mode of the electric motor instead of using the current control mode.

   Through simulations it has been demonstrated that the velocity control mode improves the performance of the actuator to accurately regulate the torque. The ability of ACSEA with the velocity control mode to regulate an oscillatory desired torque is limited due to the force and velocity saturations of the actuator, and due to the low stiffness of the AASC. The large force bandwidth is limited because of saturations and it can be adjusted by changing the stiffness of AASC.

2. Three mechanisms of adjustable stiffness artificial tendons (ASAT) were developed to investigate how adjustable stiffness compliant behavior can indeed improve the energy economy in bipedal walking. It is demonstrated that the energy loss in bipedal walking is tied to the stiffness of ASATs during the collision phase. It is shown that properly adjusting the stiffness of ASATs improves the energy economy.

3. A more in-depth study of the effects of ASATs on walking energy economy has been carried out by introducing a new simplified model of bipedal walking with OLASAT at the ankle joint. Such a model also consists of a linear spring which simulates the force generated by the trailing leg during the double support phase. Properly adjusting the stiffness of OLASAT reduces the angular velocity of the foot preceding the foot-touch-down. It assists in storing more energy of the biped in OLASAT during the collision phase which will be returned during the rebound phase. In general, simulation results in consecutive walking steps illustrate that properly adjusting the stiffness of OLASAT at the ankle joint significantly improves the energetics of the bipedal walking robots.

   The above study demonstrates the positive effects of OLASAT in energy economy and suggests that the foot with such a mechanism to adjust its stiffness is important in the design of energy-economic bipedal walking robots. The adjustable stiffness bipedal walking model can be employed as the basic mechanical model in locomotion, since it is simple and it can adjust the energy economy.

4. The linear spring in the trailing leg of the bipedal walking model during the double support phase is the major source of energy input to the biped. Because of the adjustable stiffness capability of the trailing leg spring, the injected energy to the biped can be controlled and the higher desired speed can effectively be regulated. Reducing the speed is possible by re-tuning the stiffness of OLASAT.

A reinforcement learning controller based on the geometric progression of the kinetic energy error of the biped at the midstance has been developed to adjust the stiffness of the trailing leg spring which successfully tracks a desired speed. The results support the fact that using a simplified model of bipedal walking instead of complex models helps to better understand the general behavior of the energetics of the bipedal walking. In addition, simple models provide the opportunity to test a number of mechanical design concepts of ASATs before physical implementations.

5. Through simulations it has been demonstrated that the combination of the bipedal walking model with adjustable elastic elements and the speed tracking controller can at the same time improve the energetics of the biped and regulate its speed even in the presence of disturbances. The local stability analysis of the system was also carried out by calculating the eigenvalues of the linear approximation of the return map, which shows the robustness of the system.

The next section proposes the potential topics of follow-up research of the thesis.

6.2 Outline of future work

The outline of future work is described below.

1. In this work the dynamics of the swing leg was not considered in the bipedal walking model. Modifying the model of bipedal walking to include the swing leg is recommended. This is possible through two different approaches. The first approach is assuming the swing leg as a mass–less spring, similar to the model introduced by Geyer [6], in which the simultaneous controlling of the swing leg angle with passive motion of the stance leg will be the main research question. The second approach is assuming the inertia of the swing leg and controlling the torque at the hip joint. In the second case, the effects of energy

flow (input/output) of the swing leg can be studied. In both approaches, the knee joint can be locked or free. When it is free (passive) the effects of RASAT at the knee joint, with the ability to adjust the stiffness in a wide range, can be studied.

2. In the thesis, OLASAT was only in effect during the collision and rebound phases. However, studying the effects of storing the energy in elastic form during the preload phase may help to improve the energetics. Then, such a stored energy can be used during the double support phase. This can also reduce the velocity of the COM of the biped before the heel-strike of the next walking step leading to the use of less stiffer springs in OLASAT during the collision phase which in general reduces the weight of OLASAT.

3. In the thesis, OLASAT is assumed passive during the stance phase which helped to reduce the complexities in this study. However, a series combination of OLASAT and an electric motor provides an adjustable stiffness SEA. This combination can be installed parallel to the ankle joint and the dynamics of the actuator can be studied in a more sophisticated model specially during the double support phase. This is possible by replacing the linear spring model of the trailing leg with an articulated leg and the actuator at the ankle joint. Then the energy input to the system can be directly calculated by measuring the output power of the electric motor. In addition, this series combination includes switching between the stiffness of the springs which makes the torque control more complicated.

4. Most physical springs have some hysteresis. The compression springs used in the artificial tendons and ACSEA in this thesis have no hysteresis and were assumed to be linear. Considering the effects of hysteresis in design is an important issue and using new materials in springs may result in a change in the behavior of ASATs and ACSEA.

5. In the thesis, the trailing leg during the double support phase was assumed as a linear spring. The assumption simplified the analysis. However, assuming the trailing leg as a nonlinear spring or as an articulated leg with actuation can lead to a more detailed study of the system. This may result in developing new concepts of elastic actuators and tendons for robotics applications.

6. In this thesis, the speed tracking controller in combination with the stiffness adjustment and re-tuning controllers were used to determine the required configuration of OLASAT, energy, and force. Using the adjustable stiffness elastic actuators inside the model of the biped and using a torque control loop can be the next stage of the research.

7. This thesis focused on the design of simple controllers in regulating the velocity of the biped. There exist other complex control systems that can enhance the performance of the system. The investigation of passivity-based control in speed regulation of the biped with adjustable stiffness elasticity is an interesting subject. The efficiency of the proposed control method in the thesis can be compared with that of other control methods such as passivity-based and energy optimal control methods.

8. In this thesis, simulations were performed for specific parameters and initial conditions to show the advantages and limitations of ASATs in bipedal walking robots. However, parametric study with rigorous simulations may help to complete the study.

9. The physical development of each ASAT in series with an actuator is recommended to test the real performance.

Bibliography

[1] M. M. Williamson, "Series elastic actuators," Ph.D. dissertation, Massachusetts Institute of Technology, 1995.

[2] M. W. Gomes and A. Ruina, "A walking model with no energy cost," *In revision, Physical Review E*, 2005.

[3] A. Seyfarth, "Elastically operating legs – strategies and construction principles," Ph.D. dissertation, University of Jena, 2000.

[4] H. Geyer, R. Blickan, and A. Seyfarth, "Natural dynamics of spring–like running– emergence of self stability," *5th International Conference on Climbing and Walking Robots*, pp. 87–91, 2002.

[5] H. Geyer, A. Seyfarth, and R. Blickhan, "Spring–mass running: simple approximate solution and application to gait stability," *Journal of Theoretical Biology*, vol. 232(3), pp. 315–328, 2005.

[6] H. Geyer, "Simple models of legged locomotion based on compliant limb behavior," Ph.D. dissertation, University of Jena, 2005.

[7] H. Hanafusa and H. Asada, "A robotic hand with elastic fingers and its application to assembly process," *IFAC Symposium on Information and Control Problems in manufacturing Technology*, pp. 127–138, 1977.

[8] M. Mason, *Compliant motion, in robot motion: planning and control*. MIT Press, 1982.

[9] R. H. Cannon and E. Schmitz, "Initial experiments on the end-point control of a flexible one-link robot," *International Journal of Robotics Research*, vol. 3, pp. 62–75, 1984.

[10] M. W. Spong, "Modeling and control of elastic joint robots," *Journal of Dynamic Systems, Measurement, and Control*, vol. 109, pp. 310–319, 1987.

[11] S. Sugano and I. Kato, "Force control of the robot finger joint equipped with mechanical compliance adjuster," *International Conference on Intelligent Robots and Systems*, vol. 3, pp. 2005–2013, 1992.

[12] D. Vischer and O. Khatib, "Design and development of high-performance torque-controlled joints," *IEEE Transactions on Robotics and Automation*, vol. 11(4), pp. 537–544, 1995.

[13] H. Asada and K. Youcef-Toumi, *Direct drive robots: theory and practice.* MIT Press, 1987.

[14] V. S. Kulishov and N. V. Lakota, *Remotely controlled robots and manipulators.* MIR Publisher, 1988.

[15] R. D. Howard, "Joint and actuator design for enhanced stability in robotic force control," Ph.D. dissertation, Massachusetts Institute of Technology, 1990.

[16] G. A. Pratt and M. Williamson, "Series elastic actuators," *IEEE International Conference on Intelligent Robots and Systems*, pp. 399–406, 1995.

[17] D. W. Robinson, J. E. Pratt, D. J. Paluska, and G. A. Pratt, "Series elastic actuator development for a biomimetic walking robot," *Advanced Intelligent Mechatronics*, pp. 19–22, 1999.

[18] H. Gomi, M. Nishikawa, M. Hirose, and T. Takahashi, "Legged mobile robot equipped with impact absorber," *U.S. Patent Number: 5445235*, 1995.

[19] K. Hirai, M. Hirose, Y. Haikawa, and T. Takenaka, "The development of honda humanoid robot," *IEEE International Conference on Robotics and Automation*, vol. 2, pp. 1321–1326, 1998.

[20] M. Zinn, B. Roth, O. Khatib, and J. K. Salisbury, "New actuation approach for human friendly robot design," *The International Journal of Robotics Research*, vol. 23(4-5), pp. 379–398, 2004.

[21] J. Hurst, J. Chestnutt, and A. Rizzi, "An actuator with physically variable stiffness for highly dynamic legged locomotion," *International Conference on Robotics and Automation*, pp. 4662–4667, 2004.

[22] J. Hurst and A. Rizzi, "Physically variable compliance in running," *International Conference on Climbing and Walking Robots*, pp. 123–132, 2004.

[23] A. Bicchi and G. Tonietti, "Fast and soft-arm tactics [robot arm design]," *IEEE Robotics and Automation Magazine*, vol. 11(2), pp. 22–33, 2004.

[24] M. T. Mason and J. K. Salisbury, *Robot hands and mechanics of manipulation.* MIT Press, 1985.

[25] G. Hirzinger, A. Albu-Schflafer, M. Hfahnle, I. Schaefer, and N. Sporer, "A new generation of torque controlled light-weight robots," *Proceedings of the International Conference on Robotics and Automation*, vol. 4, pp. 3356–3363, 2001.

[26] S. H. Collins, M. Wisse, and A. Ruina, "A three-dimensional passive-dynamic walking robot with two legs and knees," *International Journal of Robotics Research*, vol. 20(7), pp. 607–615, 2001.

[27] M. Coleman and A. Ruina, "An uncontrolled toy that can walk but cannot stand still," *Physical Review Letters*, vol. 80(16), pp. 3658–3661, 1998.

[28] M. S. Garcia, "Stability, scaling, and chaos in passive dynamic gait models," Ph.D. dissertation, Theoretical and Applied Mechanics, Cornell University, 1999.

[29] S. H. Collins, A. Ruina, M. Wisse, and R. Tedrake, "Efficient bipedal robots based on passive-dynamic walker," *Science Magazine*, vol. 307, pp. 1082–1085, 2005.

[30] M. Wisse and J. V. Frankenhuyzen, "Design and construction of mike; a 2d autonomous biped based on passive dynamic walking," *Adaptive Motion of Animals and Machines*, pp. 143–154, 2006.

[31] M. Wisse, "Essentials of dynamic walking: analysis and design of two-legged robots," Ph.D. dissertation, T.U. Delft, 2004.

[32] J. K. Holm, D. Lee, and M. W. Spong, "Time scaling for speed regulation in bipedal locomotion," *IEEE International Conference on Robotics and Automation*, pp. 3603–3608, 2007.

[33] M. Spong and F. Bullo, "Controlled symmetries and passive walking," *IEEE Transactions on Automatic Control*, vol. 50(7), pp. 1025–1031, 2005.

[34] M. Spong, "Some new results in passivity based control of robots," *Semi-Plenary Lecture at NOLCOS04*, 2004.

[35] M. Spong and F. Bullo, "Controlled symmetries and passive walking," *IFAC Triennial World Congress*, pp. 1025–1031, 2002.

[36] M. Spong, R. Lozano, and R. Mahony, "An almost linear biped," *IEEE Conference on Decision and Control*, pp. 4803–4808, 2000.

[37] M. Spong, "Passivity based control of the compass gait biped," *IFAC World Congress*, 1999.

[38] T. McGeer, "Passive dynamic walking," *The International Journal of Robotics Research*, vol. 9, pp. 62–82, 1990.

[39] A. D. Kuo, J. M. Donelan, and A. Ruina, "Energetic consequences of walking like an inverted pendulum: step-to-step transitions," *Exercise and Sport Sciences Reviews*, vol. 33(2), pp. 88–97, 2005.

[40] R. Blickhan, "The springmass model for running and hopping," *Journal of Biomechanics*, vol. 22, pp. 1217–1227, 1989.

[41] T. McMahon and G. Cheng, "The mechanics of running: how does stiffness couple with speed," *Journal of Biomechanics*, vol. 23 (Suppl. 1), pp. 65–78, 1990.

[42] C. Farley and D. Morgenroth, "Leg stiffness primarily depends on ankle stiffness during human hopping," *Journal of Biomechanics*, vol. 32 (3), pp. 267–273, 1999.

[43] A. Seyfarth, A. Friedrichs, V. Wank, and R. Blickhan, "Dynamics of the long jump," *Journal of Biomechanics*, vol. 32, pp. 1259–1267, 1999.

[44] S. Chelly and C. Denis, "Leg power and hopping stiffness: relationship with sprint running performance," *Medicine and Science in Sports and Exercise*, vol. 33(2), pp. 326–333, 2001.

[45] A. Seyfarth, H. Geyer, M. Gunther, and R. Blickhan, "A movement criterion for running," *Journal of Biomechanics*, vol. 35, pp. 649–655, 2002a.

[46] V. Sholukha, M. Gunther, and R. Blickhan, "Running synthesis with a passive support leg," *Hoegfors Ziebell, C. (Ed.), XII the International Biomechanics Seminar on Dynamical Simulation. Chalmers University of Technology, Gothenburg, Sweden*, pp. 63–72, 1999.

[47] D. P. Ferris, M. Louie, and C. T. Farley, "Running in the real world: adjusting leg stiffness for different surfaces," *The Royal Society B: Biological Sciences*, pp. 989–994, 1998.

[48] R. F. Ker, R. Alexander, and M. B. Bennett, "Why are mammalian tendons so thick?" *Journal of Zoology*, vol. 216, pp. 309–324, 1988.

[49] M. M. Williamson, "Robot arm control exploiting natural dynamics," Ph.D. dissertation, Massachusetts Institute of Technology, 1999.

[50] P. Gregorio, M. Ahmadi, and M. Buehler, "Design, control, and energetics of an electrically actuated leggedrobot," *IEEE Transactions on Systems, Man and Cybernetics, Part B*, vol. 27(4), pp. 626–634, 1997.

[51] D. Papadopoulos and M. Buehler, "Stable running in a quadruped robot with compliant legs," *IEEE International Conference on Robotics and Automation*, pp. 444–449, 2000.

[52] M. Srinivasan, "Why walk and run: energetic costs and energetic optimality in simple mechanics-based models of a bipedal animal," Ph.D. dissertation, Cornell University, 2006.

[53] T. M. Kubow and R. J. Full, "The role of the mechanical system in control: a hypothesis of self-stabilization in hexapedal runners," *Philosophical Transactions of the Royal Society B*, vol. 354, pp. 849–861, 1999.

[54] H. J. Ralston, *Energetics of human walking*. Plenum Press, 1976.

[55] G. J. Bastien, P. A. Willems, B. Schepens, and N. C. Heglund, "Effect of load and speed on the energetic cost of human walking," *European Journal of Applied Physiology*, vol. 94, pp. 76–83, 2005.

[56] P. Hogberg, "How do stride length and stride frequency influence the energy-output during running?" *Arbeitsphysiologie*, vol. 14, pp. 437–441, 1952.

[57] P. R. Cavanagh and K. R. Williams, "The effect of stride length variation on oxygen uptake during distance running," *Medical Science and Sports Exercise*, vol. 14, pp. 30–35, 1982.

[58] A. D. Kuo, "A simple model predicts the step length-speed relationship in human walkings," *Journal of Biomechanical Engineering*, vol. 123, pp. 264–269, 2001.

[59] J. E. Bertram and A. Ruina, "Multiple walking speed-frequency relations are predicted by constrained optimization," *Journal of Theoretical Biology*, vol. 209(4), pp. 445–453, 2001.

[60] G. A. Cavagna, N. G. Heglund, and C. R. Taylor, "Mechanical work in terrestrial locomotion: two basic mechanisms for minimizing energy expenditure," *American Journal of Physiology*, vol. 233, pp. 243–261, 1977.

[61] R. M. Alexander and M. B. Bennett, "How elastic is a running shoe?" *New Scientist*, vol. 123, pp. 45–6, 1989.

[62] G. A. Cavagna, F. P. Saibene, and R. Margaria, "Mechanical work in running," *Journal of Applied Physiology*, vol. 19, pp. 249–256, 1964.

[63] C. T. Farley and O. Gonzalez, "Leg stiffness and stride frequency in human running," *Journal of Biomechanics*, vol. 29, pp. 181–186, 1996.

[64] J. P. He, R. Kram, and T. A. McMahon, "Mechanics of running under simulated low gravity," *Journal of Applied Physiology*, vol. 71, pp. 863–870, 1991.

[65] C. T. Farley, J. Glasheen, and T. A. McMahon, "Running springs: speed and animal size," *Journal of Experimental Biology*, vol. 185, pp. 71–86, 1993.

[66] T. J. Roberts, R. L. Marsh, P. G. Weyand, and C. R. Taylor, "Muscular force in running turkeys: the economy of minimizing work," *Science*, vol. 275, pp. 1113–1115, 1997.

[67] R. M. Alexander, *Elastic mechanisms in animal movement*. Cambridge University Press, 1988.

[68] F. Iida and R. Tedrake, "Motor control optimization of compliant one-legged locomotion in rough terrain," *IEEE/RSJ International Conference on Intelligent Robots and Systems*, pp. 2230–2235, 2007.

[69] http://www2.uni-jena.de/lauflabor.html. [Online]. Available: http://www2.uni-jena.de/lauflabor.html

[70] G. A. Pratt, "Low impedance walking robots 1," *Integrative and Comparative Biology*, vol. 42(1), pp. 174–181, 2002.

[71] J. Veneman, R. Ekkelenkamp, R. Kruidhof, and F. C. T. van der Helm, "A series elastic– and bowden–cable–based actuation system for use as torque actuator in exoskeleton-type robots," *The international Journal of Robotics Research*, vol. 25(3), pp. 261–281, 2006.

[72] B. Vanderborght, B. Verrelst, R. Van Ham, M. Van Damme, D. Lefeber, B. M. Y. Duran, and P. Beyl, "Exploiting natural dynamics to reduce energy consumption by controlling the compliance of soft actuators," *The international Journal of Robotics Research*, vol. 25(4), pp. 343–358, 2006.

[73] R. Van Der Linde, "Active leg compliance for passive walking," *International Conference on Robotics and Automation*, vol. 3, pp. 2339–2344, 1998.

[74] F. Daerden and D. Lefeber, "The concept and design of pleated pneumatic artificial muscles," *International Journal of Fluid Power*, vol. 2(3), pp. 41–50, 2001.

[75] http://lucy.vub.ac.be. [Online]. Available: http://lucy.vub.ac.be

[76] G. Tonietti, R. Schiavi, and A. Bicchi, "Design and control of a variable stiffness actuator," *IEEE ICRA International Conference on Robotics and Automation*, pp. 528–533, 2005.

[77] S. A. Migliore, E. A. Brown, and S. P. DeWeerth, "Biologically inspired joint stiffness control," *IEEE ICRA International Conference on Robotics and Automation*, pp. 4508–4513, 2005.

[78] K. Hollander, T. Sugar, and D. Herring, "Adjustable robotic tendon using a 'jack spring'," *9th International Conference on Rehabilitation Robotics*, pp. 113–118, 2005.

[79] S. K. Au and H. Herr, "Initial experimental study on dynamic interaction between an amputee and a powered ankle-foot prosthesis," *Workshop on Dynamic Walking: Mechanics and Control of Human and Robot Locomotion*, 2006.

[80] S. K. Au, P. Dilworth, and H. Herr, "An ankle-foot emulation system for the study of human walking biomechanics," *IEEE International Conference on Robotics and Automation*, pp. 2939–2945, 2006.

[81] S. Au, P. Bonato, and H. Herr, "An emg-position controlled system for an active ankle-foot prosthesis: An initial experimental study," *IEEE 9th International Conference on Rehabilitation Robotics (ICORR): Frontiers of the Human-Machine Interface*, pp. 375–379, 2005.

[82] H. Herr, "Multidisciplinary approaches to limb loss: a chain of events leading to a single step," *Journal of Rehabilitation Research and Development; White House/VA Conference, Emerging Technologies; Washington D.C.*, pp. 76–80, 2005.

[83] R. Aaron, H. Herr, D. Ciombor, L. Hochberg, J. Donoghue, C. Briant, J. Morgan, and M. Ehrlich, "Horizons in prosthesis development for the restoration of limb function," *Journal of the American Academy of Orthopaedic Surgeons*, vol. 14(10), pp. 198–204, 2006.

[84] D. Paluska and H. Herr, "The effect of series elasticity on actuator power and work output: Implications for robotic and prosthetic joint design," *Robotics and Autonomous Systems*, vol. 54, pp. 667–673, 2006.

[85] J. Johansson, D. Sherrill, P. Riley, B. Paolo, and H. Herr, "A clinical comparison of variable-damping and mechanically-passive prosthetic knee devices," *American Journal of Physical Medicine and Rehabilitation*, vol. 84(8), pp. 563–575, 2005.

[86] D. H. Gates, J. Lelas, U. Della Croce, H. Herr, and B. P., "Characterization of ankle function during stair ambulation," *26th International Conference of the IEEE Engineering in Medicine and Biology Society*, vol. 6, pp. 4248–4251, 2004.

[87] F. E. Zajac, "Muscle coordination of movement: a perspective," *Journal of Biomechanics*, vol. 26, pp. 109–124, 1993.

[88] F. E. Zajac, "Muscle and tendon: properties, models, scaling, and application to biomechanics and motor control," *Critical Reviews in Biomedical Engineering*, vol. 17(4), pp. 359–411, 1989.

[89] S. L. Delp and J. P. Loan, "A computational framework for simulating and analyzing human and animal movement," *IEEE Computational Science and Engineering*, vol. 2, pp. 46–55, 2000.

[90] R. Neptune, F. Zajac, and S. Kautz, "Muscle force redistributes segmental power for body progression during walking," *Gait and Posture*, vol. 19, pp. 194–205, 2004.

[91] R. Alexander, "Energy-saving mechanisms in walking and running," *Journal of Experimental Biology*, vol. 160, pp. 55–69, 1991.

[92] R. Alexander, "A model of bipedal locomotion on compliant legs," *Philosophical Transactions: Biological Sciences*, vol. B338, pp. 189–198, 1992.

[93] R. Alexander, "Invited editorial on interaction of leg stiffness and surface stiffness during human hopping," *Journal of Applied Physiology*, vol. 82, pp. 13–14, 1997.

[94] R. Alexander, "Design by numbers," *Nature*, vol. 412(591), 2001.

[95] R. Alexander, "Tendon elasticity and muscle function," *Comparative Biochemistry and Physiology*, vol. 133, pp. 1001–1011, 2002.

[96] R. Alexander, *Principles of animal locomotion*. Princeton University Press, 2003.

[97] R. Alexander, "Optimization and gaits in the locomotion of vertebrates," *Physiological Review*, vol. 69, pp. 1199–1227, 1989.

[98] R. Alexander, *Energy for animal life*. Oxford University Press, 1999.

[99] R. Donelan, J.M. Kram and A. Kuo, "Mechanical work for step-to step transitions is a major determinant of the metabolic cost of human walking," *Journal of Experimental Biology*, vol. 205, pp. 3717–3727, 2002.

[100] A. D. Kuo, "Energetics of actively powered locomotion using the simplest walking model," *Journal of Biomechanical Engineering*, vol. 124, pp. 113–120, 2002.

[101] A. D. Kuo and C. E. Bauby, "Active control of lateral balance in human walking," *Journal of Biomechanical Engineering*, vol. 33, pp. 1433–1440, 2000.

[102] M. J. Donelan, R. Kram, and A. D. Kuo, "Simultaneous positive and negative external mechanical work in human walking," *Journal of Biomechanical Engineering*, vol. 35, pp. 117–124, 2002.

[103] J. E. Bertram, A. Ruina, C. E. Cannon, Y. H. Chang, and M. Coleman, "Point-mass model of gibbon locomotion," *Journal of Experimental Biology*, vol. 202, pp. 2609–2617, 1999.

[104] S. Collins, A. Ruina, R. Tedrake, and M. Wisse, "Efficient bipedal robots based on passive dynamic walkers," *Science Magazine*, vol. 307, pp. 1082–1085, 2005.

[105] M. Garcia, A. Chatterjee, and A. Ruina, "Efficiency, speed, and scaling of two-dimensional passive-dynamic walking," *Dynamics and Stability of Systems*, vol. 2, pp. 75–99, 2000.

[106] M. Gomes and A. Ruina, "A five-link 2d brachiating ape model with life-like zero-energy-cost motions," *Journal of Theoretical Biology*, vol. 237(3), pp. 265–278, 2005.

[107] A. Ruina, J. Bertram, and M. Srinivasan, "A collisional model of the energetic cost of support work qualitatively explains leg-sequencing in walking and galloping, pseudo-elastic leg behavior in running and the walk-to-run transition," *Journal of Theoretical Biology*, vol. 14, pp. 170–192, 2005.

[108] S. H. Collins, A. Ruina, R. Tedrake, and M. Wisse, "Efficient bipedal robots based on passive-dynamic walkers," *Science*, vol. 307, pp. 1082–1085, 2005.

[109] R. L. Norton, *Design of machinery*, K. T. Kane, Ed. Thomas Casson, 1999.

[110] D. T. Greenwood, *Advanced Dynamics*. Cambridge University Press, 2003.

[111] X. Mu, "Dynamic and motion regulation of a five link biped robot walking in the sagittal plane," Ph.D. dissertation, University of Manitoba, 2004.

[112] X. Mu and Q. Wu, "Development of a complete dynamic model of a planar five-link biped and sliding mode control of its locomotion during the double support phase," *International Journal of Control*, vol. 77 (Suppl. 8), pp. 789–799, 2004.

[113] S. Tzafestas, M. Raibert, and C. Tzafestas, "Robust sliding mode control applied to a 5-link biped robot," *Journal of Intelligent and Robotic Systems*, vol. 15, pp. 67–133, 1996.

[114] S. H. Strogatz, *Nonlinear dynamics and chaos: with applications to physics, biology, chemistry, and engineering*. Pereus Books, 1994.

[115] D. E. Koditscheck and M. Buhler, "Analysis of a simplified hopping robot," *The International Journal of Robotics Research*, vol. 10(6), pp. 587–605, 1991.

[116] R. L. Tedrake, "Applied optimal control for dynamically stable legged locomotion," Ph.D. dissertation, Massachusetts Institute of Technology, 2004.

Appendix A

Derivation of Dynamic Model of the Robot

According to the kinematic model shown in Figure 4.13, the coordinates of mass center of each link are:

$$x_{c1} = d_1 cos\theta_1 + x_h \tag{A.1}$$
$$y_{c1} = d_1 sin\theta_1 + y_h \tag{A.2}$$
$$x_{c2} = l_1 cos\theta_1 + d_2 cos\theta_2 + x_h \tag{A.3}$$
$$y_{c2} = l_1 sin\theta_1 + d_1 sin\theta_2 + y_h \tag{A.4}$$
$$x_{c3} = l_1 cos\theta_1 + l_2 cos\theta_2 + d_3 cos\theta_3 + x_h \tag{A.5}$$
$$y_{c3} = l_1 sin\theta_1 + l_2 sin\theta_2 + d_3 sin\theta_3 + y_h \tag{A.6}$$

The velocity of mass center of each link are:

$$\dot{x}_{c1} = -d_1 sin\theta_1 \dot{\theta}_1 + \dot{x}_h \tag{A.7}$$
$$\dot{y}_{c1} = d_1 cos\theta_1 \dot{\theta}_1 + \dot{y}_h \tag{A.8}$$
$$\dot{x}_{c2} = -l_1 sin\theta_1 \dot{\theta}_1 - d_2 sin\theta_2 \dot{\theta}_2 + \dot{x}_h \tag{A.9}$$
$$\dot{y}_{c2} = l_1 cos\theta_1 \dot{\theta}_1 + d_2 cos\theta_2 \dot{\theta}_2 + \dot{y}_h \tag{A.10}$$
$$\dot{x}_{c3} = -l_1 sin\theta_1 \dot{\theta}_1 - l_2 sin\theta_2 \dot{\theta}_2 - d_3 sin\theta_3 \dot{\theta}_3 + \dot{x}_h \tag{A.11}$$
$$\dot{y}_{c3} = l_1 cos\theta_1 \dot{\theta}_1 + l_2 cos\theta_2 \dot{\theta}_2 + d_3 cos\theta_3 \dot{\theta}_3 + \dot{y}_h \tag{A.12}$$

The kinetic (K_i) and potential (P_i) energy of each link are:

$$K_1 = \frac{1}{2} m_1 d_1^2 \dot{\theta}_1^2 \tag{A.13}$$

$$P_1 = m_1 g d_1 sin\theta_1 \tag{A.14}$$

$$K_2 = \frac{1}{2} m_2 d_2^2 \dot{\theta}_2^2 + \frac{1}{2} m_2 l_1^2 \dot{\theta}_1^2 + m_2 l_1 d_2 cos(\theta_1 - \theta_2)\dot{\theta}_1 \dot{\theta}_2 \tag{A.15}$$

$$P_2 = m_2 g(l_1 sin\theta_1 + d_2 cos\theta_2) \tag{A.16}$$

$$K_3 = \frac{1}{2} m_3 d_3^2 \dot{\theta}_3^2 + \frac{1}{2} m_3 [l_1^2 \dot{\theta}_1^2 + l_2^2 \dot{\theta}_2^2 + 2 l_1 l_2 cos(\theta_1 - \theta_2)\dot{\theta}_1 \dot{\theta}_2 \tag{A.17}$$

$$+2 l_1 d_3 cos(\theta_1 - \theta_3)\dot{\theta}_1 \dot{\theta}_3 + 2 l_2 d_2 cos(\theta_2 - \theta_3)\dot{\theta}_2 \dot{\theta}_3]$$

$$P_3 = m_3 g(l_1 sin\theta_1 + l_2 sin\theta_2 + d_3 cos\theta_3) \tag{A.18}$$

From (A1) to (A18), one obtains:

$$\frac{\partial P}{\partial \theta_1} = [m_1 d_1 + m_2 l_1 + m_3 l_1] g cos\theta_1 \tag{A.19}$$

$$\frac{\partial P}{\partial \theta_2} = [m_2 d_2 + m_3 l_2] g cos\theta_2 \tag{A.20}$$

$$\frac{\partial P}{\partial \theta_3} = [m_3 d_3] g cos\theta_3 \tag{A.21}$$

that can be formulated in general form of:

$$\frac{\partial P}{\partial \theta_i} = \left[m_i d_i + \left(\sum_{k=i+1}^{3} m_k \right) l_i \right] g cos\theta_i \tag{A.22}$$

From (A1) to (A18), one obtains:

$$\frac{\partial K}{\partial \theta_1} = -[m_2 l_1 d_2 + m_3 l_1 l_2] sin(\theta_1 - \theta_2)\dot{\theta}_1 \dot{\theta}_2 - m_3 l_1 d_3 sin(\theta_1 - \theta_3)\dot{\theta}_1 \dot{\theta}_3 \tag{A.23}$$

$$\frac{\partial K}{\partial \theta_2} = -[m_2 l_1 d_2 + m_3 l_1 l_2] sin(\theta_1 - \theta_2)\dot{\theta}_1 \dot{\theta}_2 - m_3 l_2 d_3 sin(\theta_2 - \theta_3)\dot{\theta}_2 \dot{\theta}_3 \tag{A.24}$$

$$\frac{\partial K}{\partial \theta_3} = -[m_3 l_1 d_3] sin(\theta_1 - \theta_3)\dot{\theta}_1 \dot{\theta}_3 + m_3 l_2 d_3 sin(\theta_2 - \theta_3)\dot{\theta}_2 \dot{\theta}_3 \tag{A.25}$$

that can be formulated in general form of:

$$\frac{\partial K}{\partial \theta_i} = -\sum_{j=1}^{i-1} \left\{ \left[m_i d_i + \left(\sum_{k=i+1}^{3} m_k \right) l_i \right] l_j sin(\theta_i - \theta_j)\dot{\theta}_i \dot{\theta}_j \right\} \tag{A.26}$$

$$-\sum_{j=i+1}^{3} \left\{ \left[m_j d_j + \left(\sum_{k=j+1}^{3} m_k \right) l_j \right] l_i sin(\theta_i - \theta_j)\dot{\theta}_i \dot{\theta}_j \right\}$$

From (A1) to (A18), one obtains:

$$\frac{\partial K}{\partial \dot{\theta}_1} = [m_1 d_1^2 + (m_2 + m_3) l_1^2]\dot{\theta}_1 + [m_2 l_1 d_2 + m_3 l_1 l_2] cos(\theta_1 - \theta_2)\dot{\theta}_2 + m_3 l_1 d_3 cos(\theta_1 - \theta_3)\dot{\theta}_3 \tag{A.27}$$

$$\frac{\partial K}{\partial \dot{\theta}_2} = [m_2 l_1 d_2 + m_3 l_1 l_2] cos(\theta_1 - \theta_2)\dot{\theta}_1 + [m_2 d_2^2 + m_3 l_2^2]\dot{\theta}_2 + m_3 l_2 d_3 cos(\theta_2 - \theta_3)\dot{\theta}_3 \tag{A.28}$$

$$\frac{\partial K}{\partial \dot{\theta}_3} = m_3 l_1 d_3 cos(\theta_1 - \theta_3)\dot{\theta}_1\dot{\theta}_3 + m_3 l_2 d_3 cos(\theta_2 - \theta_3)\dot{\theta}_2 + m_3 d_3^2 \dot{\theta}_3 \tag{A.29}$$

that can be formulated in general form of:

$$\frac{\partial K}{\partial \dot{\theta}_i} = \left[m_i d_i^2 + \left(\sum_{k=i+1}^{3} m_k \right) l_i^2 \right] \dot{\theta}_i + \sum_{j=1}^{i-1} \left\{ \left[m_i d_i + \left(\sum_{k=i+1}^{3} m_k \right) l_i \right] l_j cos(\theta_i - \theta_j)\dot{\theta}_j \right\} + \sum_{j=i+1}^{3} \left\{ \left[m_j d_j + \left(\sum_{k=j+1}^{3} m_k \right) l_j \right] l_i cos(\theta_i - \theta_j)\dot{\theta}_j \right\} \tag{A.30}$$

From (A1) to (A18), one obtains:

$$\frac{d}{dt}\left(\frac{\partial K}{\partial \dot{\theta}_1}\right) = [m_1 d_1^2 + (m_2 + m_3) l_1^2]\ddot{\theta}_1 + [m_2 l_1 d_2 + m_3 l_1 l_2] cos(\theta_1 - \theta_2)\ddot{\theta}_2 + m_3 l_1 d_3 cos(\theta_1 - \theta_3)\dot{\theta}_3 - [m_2 l_1 d_2 + m_3 l_1 l_2] sin(\theta_1 - \theta_2)\dot{\theta}_1\dot{\theta}_2 + [m_2 l_1 d_2 + m_3 l_1 l_2] sin(\theta_1 - \theta_2)\dot{\theta}_2^2 - m_3 l_1 d_3 sin(\theta_1 - \theta_3)\dot{\theta}_1\dot{\theta}_3 + m_3 l_1 d_3 sin(\theta_1 - \theta_3)\dot{\theta}_3^2 \tag{A.31}$$

$$\frac{d}{dt}\left(\frac{\partial K}{\partial \dot{\theta}_2}\right) = [m_2 d_2^2 + m_3 l_2^2]\ddot{\theta}_2 + [m_2 l_1 d_2 + m_3 l_1 l_2] cos(\theta_1 - \theta_2)\ddot{\theta}_1 + m_3 l_2 d_3 cos(\theta_2 - \theta_3)\ddot{\theta}_3 + [m_2 l_1 d_2 + m_3 l_1 l_2] sin(\theta_1 - \theta_2)\dot{\theta}_1\dot{\theta}_2 - [m_2 l_1 d_2 + m_3 l_1 l_2] sin(\theta_1 - \theta_2)\dot{\theta}_2^2 - m_3 l_2 d_3 sin(\theta_2 - \theta_3)\dot{\theta}_2\dot{\theta}_3 + m_3 l_2 d_3 sin(\theta_2 - \theta_3)\ddot{\theta}_3 \tag{A.32}$$

$$\frac{d}{dt}\left(\frac{\partial K}{\partial \dot{\theta}_3}\right) = m_3 d_3^2 \ddot{\theta}_3 + m_3 l_1 d_3 cos(\theta_1 - \theta_3)\ddot{\theta}_1 + m_3 l_2 d_3 cos(\theta_2 - \theta_3)\ddot{\theta}_2 + m_3 l_1 d_3 sin(\theta_1 - \theta_3)\dot{\theta}_1\dot{\theta}_3 - m_3 l_2 d_3 sin(\theta_1 - \theta_3)\dot{\theta}_1^2 + m_3 l_2 d_3 sin(\theta_2 - \theta_3)\dot{\theta}_2\dot{\theta}_3 - m_3 l_2 d_3 sin(\theta_2 - \theta_3)\dot{\theta}_2^2 \tag{A.33}$$

that can be formulated in general form of:

$$\begin{aligned}\frac{d}{dt}\left(\frac{\partial K}{\partial \dot{\theta}_i}\right) &= [m_i d_i^2 + \left(\sum_{k=j+1}^{3} m_k\right) l_i^2]\ddot{\theta}_i \\ &+ \sum_{j=1}^{i-1}\left\{\left[m_i d_i + \left(\sum_{k=i+1}^{3} m_k\right) l_i\right] l_j cos(\theta_i - \theta_j)\ddot{\theta}_j\right\} \\ &+ \sum_{j=i+1}^{3}\left\{\left[m_j d_j + \left(\sum_{k=j+1}^{3} m_k\right) l_j\right] l_i cos(\theta_i - \theta_j)\ddot{\theta}_j\right\} \\ &+ \sum_{j=1}^{i-1}\left\{\left[m_i d_i + \left(\sum_{k=i+1}^{3} m_k\right) l_i\right] l_j sin(\theta_i - \theta_j)\dot{\theta}_j(\dot{\theta}_j - \dot{\theta}_i)\right\} \\ &+ \sum_{j=i+1}^{3}\left\{\left[m_j d_j + \left(\sum_{k=j+1}^{3} m_k\right) l_j\right] l_i sin(\theta_i - \theta_j)\dot{\theta}_j(\dot{\theta}_j - \dot{\theta}_i)\right\}\end{aligned} \tag{A.34}$$

In general the inertia matrix during continuous motion is a 3×3 matrix that is obtained:

$$\frac{\partial K}{\partial \dot{\theta}_i \dot{\theta}_j} = \begin{cases} m_i d_i^2 + \left(\sum_{k=i+1}^{3} m_k\right) l_i^2 & i = j \\ \left(m_j d_j l_j + \left(\sum_{k=j+1}^{3} m_k\right) l_i l_j\right)\cos(\theta_i - \theta_j) & j > i \\ \left(m_i d_i l_i + \left(\sum_{k=i+1}^{3} m_k\right) l_j l_i\right)\cos(\theta_j - \theta_i) & j < i \end{cases} \tag{A.35}$$

The inertia matrix before heel strike is obtained as:

$$D = \begin{bmatrix} D1 & D2 \\ \\ D3 & D4 \end{bmatrix} \tag{A.36}$$

where $D1$ is a 2×2 matrix:

$$D1_{ij} = \begin{bmatrix} \sum_{k=1}^{3} m_k & 0 \\ \\ 0 & \sum_{k=1}^{3} m_k \end{bmatrix} \tag{A.37}$$

and $D2$ is a 2×3 matrix:

$$D2_{ij} = \begin{cases} m_j d_j + \left(\sum_{k=j+1}^{3} m_k\right) l_j sin(\theta_j) & i = 1 \\ \\ m_j d_j + \left(\sum_{k=j+1}^{3} m_k\right) l_j cos(\theta_j) & i = 2 \end{cases} \tag{A.38}$$

and D3 is transpose of D2 matrix:

$$D3_{ij} = D2_{ji} \tag{A.39}$$

and D4 is a 3×3 matrix:

$$D4_{ij} = \begin{cases} m_i d_i^2 + \left(\sum_{k=i+1}^{3} m_k\right) l_i^2 & i = j \\ \left(m_j d_j l_j + \left(\sum_{k=j+1}^{3} m_k\right) l_i l_j\right) \cos(\theta_i - \theta_j) & j > i \\ \left(m_i d_i l_i + \left(\sum_{k=i+1}^{3} m_k\right) l_j l_i\right) \cos(\theta_j - \theta_i) & j < i \end{cases} \tag{A.40}$$